

INFORMATION TO USERS

This manuscript has been reproduced from the microfilm master. UMI films the text directly from the original or copy submitted. Thus, some thesis and dissertation copies are in typewriter face, while others may be from any type of computer printer.

The quality of this reproduction is dependent upon the quality of the copy submitted. Broken or indistinct print, colored or poor quality illustrations and photographs, print bleedthrough, substandard margins, and improper alignment can adversely affect reproduction.

In the unlikely event that the author did not send UMI a complete manuscript and there are missing pages, these will be noted. Also, if unauthorized copyright material had to be removed, a note will indicate the deletion.

Oversize materials (e.g., maps, drawings, charts) are reproduced by sectioning the original, beginning at the upper left-hand corner and continuing from left to right in equal sections with small overlaps.

**ProQuest Information and Learning
300 North Zeeb Road, Ann Arbor, MI 48106-1346 USA
800-521-0600**

UMI[®]

**VARIATIONS IN ICE FLOW AND GLACIERS
OVER TIME AND SPACE**

**A
THESIS**

**Presented to the Faculty
of the University of Alaska Fairbanks**

**in Partial Fulfillment of the Requirements
for the Degree of**

DOCTOR OF PHILOSOPHY

**By
Daniel Harry Elsberg, B.S.**

Fairbanks, Alaska

May 2003

UMI Number: 3079039

UMI[®]

UMI Microform 3079039

Copyright 2003 by ProQuest Information and Learning Company.

All rights reserved. This microform edition is protected against
unauthorized copying under Title 17, United States Code.

ProQuest Information and Learning Company

300 North Zeeb Road

P.O. Box 1346

Ann Arbor, MI 48106-1346

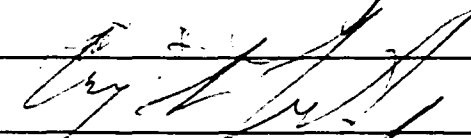
VARIATIONS IN ICE FLOW AND GLACIERS
OVER TIME AND SPACE

By

Daniel Harry Elsberg

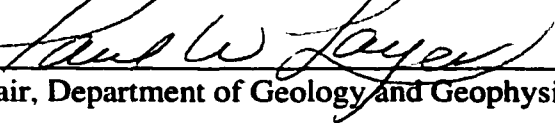
RECOMMENDED:



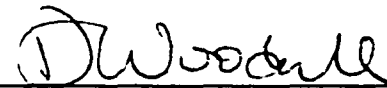




Advisory Committee Chair


Chair, Department of Geology and Geophysics


APPROVED:



Dean, College of Science, Engineering and Mathematics



Dean of the Graduate School



Date

Abstract.

Ice flows and glaciers change over many time and spatial scales. Glacier surfaces evolve over decades, and this change affects the glacier-climate interaction. When a mass balance is computed using an outdated map, that computation does not reveal actual mass change. We present a method by which a mass balance computed with an outdated map can be transformed into actual mass change. While the actual volume change of a glacier is relevant to hydrological studies, the change that would have occurred on a static surface is more relevant to certain glacier dynamics problems and most climate problems. We term this the reference-surface balance and propose that such a balance is better correlated to climatic variations than the conventional one.

Ice responds to stresses over time scales from seconds to millennia. We observed this using two independent strain-gauge systems to measure the strain rates as functions of depth and time at Siple Dome, Antarctica. One system employed optical fibers to measure annual strain rates over 175 m depth intervals. The other used one-meter resistance wires to measure strain approximately hourly at discrete depths. The long-term average strain rates from the two systems agreed to within 16%. The time-dependent strain rates measured beneath the divide by the resistance-wire gauges included intermittent strain events lasting up to 24 hours. We used the results from each system to compute an age-depth relationship assuming a time-independent ice flow geometry.

Equilibrium line altitudes are related to climate, and they vary from year to year and among neighboring glaciers. We measured a regional pattern of equilibrium lines using remote sensing. Our goals were to evaluate the accuracy of such measurements, and to assess the spatial and temporal variability of the resulting data. Individual glacier equilibrium line altitudes varied by 100 m relative to a smoothed surface, and inter-annual variations in equilibrium line altitudes at one glacier were 74 m. A map of the regional pattern of equilibrium line altitudes shows variations of 1000 meters from the south to the north side of the range, but no major trend from east to west.

Table of Contents

Signature Page	i
Title Page	ii
Abstract	iii
Table of Contents	iv
List of Figures	vii
List of Tables	viii
List of Appendices	ix
Acknowledgments	x
General Introduction	1
Chapter 1. Quantifying the Effects of Climate and Surface Change on Glacier Mass Balance	3
INTRODUCTION	4
THE RELATIONSHIP BETWEEN CONVENTIONAL AND REFERENCE-SURFACE BALANCES	5
Mass balance notation	5
Definition of the conventional and reference-surface glacier-wide balance rates	6
A relation between conventional and reference-surface glacier-wide balance rates ...8	8
Transformation between conventional and reference-surface glacier-wide annual balances	10
Geodetic corrections	11
Summary of the transformation method	12
APPLICATION TO SOUTH CASCADE GLACIER	13
Data	13
The exact transformation	14
Approximations for the exact transformation	16
Cumulative effects of geometry changes on mass balance	18
DISCUSSION	18
What measurements are needed?	18
Choice of the reference surface	19

Relevance of the reference-surface balance to glacier dynamics and climate studies	20
CONCLUSIONS	20
ACKNOWLEDGEMENTS	21
REFERENCES	33
APPENDIX 1.0: DETAILS OF MASS BALANCE CALCULATIONS	35
COMPUTING A GEODETIC CUMULATIVE BALANCE SERIES	35
EXTRAPOLATION OF BALANCE-ELEVATION CURVES	35
Chapter 2. Depth- and time-dependent strain rates and their variations at Siple Dome, Antarctica	37
INTRODUCTION	38
INSTRUMENTATION	39
Fiber-optic system design.....	39
Resistance-wire system design.....	40
Laboratory testing.....	41
Deployment and freeze-in.....	43
Gauge-design comparison.....	44
RESULTS	45
Data overview.....	45
System performance.....	46
Long-term average strain rates.....	48
Time-dependent strain rates and strain events.....	51
DISCUSSION AND SUMMARY	52
System performance.....	52
Long-term average strain rates.....	53
Time-dependent strain rates and strain events.....	55
CALCULATING AN AGE-DEPTH RELATIONSHIP AT DIVIDE	60
CONCLUSIONS	62
ACKNOWLEDGEMENTS	63
REFERENCES	76
Chapter 3. Mapping the regional distribution of equilibrium lines: a case study in the western Chugach Mountains, Alaska	80

INTRODUCTION.....	81
MEASURING EQUILIBRIUM LINE ALTITUDES.....	83
Mass-balance methods.....	83
Reconnaissance methods.....	84
PREVIOUS STUDIES	86
THE SOURCE IMAGERY	89
METHODS	91
Measuring ELAs from photographs and video images	91
Measuring the regional distribution of snow line elevations from Landsat scenes... 93	93
ERRORS IN THE ELA MEASUREMENTS.....	94
ELA VARIATIONS WITH TIME	95
SPATIAL VARIABILITY OF ELA'S	97
SUMMARY AND CONCLUSIONS.....	98
REFERENCES.....	111
APPENDIX 3.1: DESCRIPTION OF THE VIDEO AND ALTIMETRY SYSTEM 115	115
INSTRUMENTATION	115
The existing laser altimetry system.....	115
The camera	115
DATA COLLECTION AND PROCESSING	116
Field work	117
Image Processing.....	117
APPENDIX 3.2: IMAGE RECTIFICATION AND GEOLOCATION.....	119
General Conclusions.....	121

List of Figures

Figure 1.1: Schematic of a glacier.....	22
Figure 1.2: Flow chart	23
Figure 1.3: South Cascade area.....	24
Figure 1.4: Geodetic cumulative balance	25
Figure 1.5: Effective gradients and balances	26
Figure 1.6: Annual balances	27
Figure 1.7: Cumulative balances.....	28
Figure 1.8: Area and volume terms.....	29
Figure 2.1: Location map.....	65
Figure 2.2: Gauge Design	66
Figure 2.3: Sample gauges	67
Figure 2.4: Long-term average strain rates.....	68
Figure 2.5: Annual strain rates	69
Figure 2.6: Detrended strains.....	70
Figure 2.7: Sample strain events	71
Figure 2.8: Strain-event amplitudes	72
Figure 2.9: Gauge-to-ice coupling	73
Figure 2.10: Age-depth relationship	74
Figure 3.1: Location map.....	100
Figure 3.2: Example aerial photograph	101
Figure 3.3: Example video mosaic.....	102
Figure 3.4: Landsat scene	103
Figure 3.5: Snow line rise.....	104
Figure 3.6: Seasonal and map corrections	105
Figure 3.7: ELAs and their variability.....	106
Figure 3.8: ELA time series.....	107
Figure 3.9: ELA spatial distribution.....	108

List of Tables

Table 1.1: Table of variables	30
Table 1.2: Balance methods.....	31
Table 1.3: Area and balances	32
Table 2.1: Long term average strain rates	75
Table 3.1: Source imagery	109
Table 3.2: ELA results.....	110

List of Appendices

APPENDIX 1.0: DETAILS OF MASS BALANCE CALCULATIONS.....	35
APPENDIX 3.1: DESCRIPTION OF THE VIDEO AND ALTIMETRY SYSTEM....	115
APPENDIX 3.2: IMAGE RECTIFICATION AND GEOLOCATION	119

Acknowledgments

As I sit at my desk writing this, I am watching yellow iron ripping a moat around the entire Geophysical Institute. I take that as a sign that it's time for me to move on. While I can think of a million things I am looking forward to doing without this infinite time sink called school, I am thankful to a lot of folks who helped me get to this point.

Academically, I have been lucky enough to work with some amazing advisors and mentors. As an undergraduate, I built racecars instead of going to classes. I liked the machine shop far better than the senior physics lab. But when the engine wouldn't start or the hubs wouldn't turn and I was tearing my hair out, ARG (short for Albert R. George) would just say that "F still equals MA." It's amazing how that can get me through a lot of engineering, physics and cabin construction dilemmas.

So when I got to UAF I met Will Harrison, my advisor. Will thinks that engineers are lower than geographers. Will taught me much more important things, like putting tick marks on the right hand and top axes of graphs, jury rigging cars to drive when the fuel lines are froze up, and always to ask what's the uncertainty. Keith Echelmeyer may as well have been my co-advisor. Keith is 95% math whiz, 95% jock, 95% bush pilot, and 95% all-around good guy. Keith also came up with the idea of letting me engineer a bit when I was really down on school.

The other folks here at the GI have been a blast to work and play with. Ray Ward is always looking out for other folks. My fellow students (yeah Martin, you'll always be a student in my mind) really make it hard to believe that there are people who don't like their co-workers. Karo, I wish you got to see me pull this off. By, Sandy, and Patti cranked through endless laser altimetry data which I used, and provided loon calls on the hour. And thanks to the 6th floor folks who made things work even as Wadlow cackled off into the sunset.

Moving 3000 miles away from where I grew up, just to be down the road from my brother and now my sister-in-law has been great. Thank you Andy and Shannon for being around when I needed a hand – sorry about Rusty barking all night and peeing on your rug. The rest of my family is still on the east coast, but still gave me plenty to keep

me moving along. Mom, Dad, Jon, Mom-mom, and Lucia – sorry I don't call enough. The oranges and grape-fruits and pears you've sent have perked up quite a few winter weeks.

Laura has certainly made sure I haven't starved or gone cold, and from 3000 miles away too. Stacie, you opened up a new world to me, even if I never end up "living in the bush, Miller style." Lars has yet to say no when I've asked for a hand, or a futon, or a hunk of steel, or a lamp, or a... And Andrea, I'm looking forward to seeing what you can cook when you have more than a toaster oven and a single electric burner. Too bad I have to move out to make that happen. I really owe Tanja a lot of thanks, and numerous weekends hiking or skiing, for putting up with me over the last year. I'm looking forward to lots of adventures together: now and later, here and there, you and me.

Speaking of putting up with me, there's a crowd who never (well, almost never) complained about late dinners, not enough trail miles, and way too much poop in the yard. Rusty, Denali, Lupine, Gulo, Java, Merlin, Ester, Murphy, Adia, Sammy, and Mona-Lisa – arf-arf. Grover – I'll pack one for you. Snuf and Lily – get ready for some long trail rides, we're going places.

General Introduction

Glaciers and ice vary over many scales in time and space. Ice flow and deformation are determined in part by atomic and molecular bonds on the order of 10^{-10} m, yet this ice flow can be expressed over lengths of hundreds of kilometers as in Antarctic ice streams. Seismic waves propagate through ice at thousands of meters per second, while valley glaciers sometimes move only a few meters per year. In this thesis I present measurements of ice deformation and glacier variations in time and space. The three chapters are placed in the order of their completion, and each one was written to stand alone as a journal article, including individual reference lists, acknowledgements and appendices.

Chapter 1 deals with the feedback of glacier geometry changes over years and decades. This paper takes a utilitarian slant of correcting for errors in mass balance calculations due to the use of outdated maps. The ideas are more general than that, however, and allow one to distinguish between the influence of climate and the influence of surface geometry changes on mass balance. This paper was published in the *Journal of Glaciology*. William Harrison and Keith Echelmeyer had discussed these ideas over a long time period before I became involved. Robert Krimmel provided the field data from South Cascade glacier. While Will Harrison had written an early draft based on these ideas, the vast majority of the text in this chapter is mine, due to two complete rewrites of the paper.

Chapter 2 presents measurements of vertical strain rate made at Siple Dome, Antarctica. The ideas of time and length scales are peppered throughout this paper. Two types of gauges were utilized, one measuring strain rates over 1 m intervals and every hour. The other measured displacements over hundreds of meters and only over year long time intervals. During the experiment, we observed strain rate fluctuations over hours, months and years. This paper is in preparation for submission to the *Journal of Glaciology*. William Harrison designed the earlier prototypes of the strain gauges and has deployed them in Alaska and Antarctica. The fiber-optic gauges are Mark Zumberg's design and he was in charge of that portion of the experiment. The finite

element modeling discussed was done by Erin Pettit, Ed Waddington and Nadine Naruse. I worked on the construction and laboratory testing of the resistance-wire gauges, helped to deploy them, performed all of the processing and analysis of the data, and wrote the entire paper, incorporating copious comments from the co-authors and my committee.

Chapter 3 is a first step in determining regions of glaciers exhibiting similar responses to climatic forcing. This will improve our understanding of how measurements of volume change and mass balance on individual glaciers relate to neighboring glaciers. By mapping equilibrium line altitudes in the western Chugach Mountains, Alaska, general patterns appear over hundreds of kilometers. Individual glacier equilibrium line altitudes vary relative to the general patterns on length scales of just a few kilometers. There are also large variations in equilibrium lines from year to year which obscure the patterns related to climatic trends we would otherwise expect to see over decades. This paper is in preparation for submission to the Journal of Glaciology. William Harrison laid out the motivating problem which we discuss in this paper. Keith Echelmeyer provided the laser altimetry data and flew the airplane.. The laser-altimetry system is the result of many people's work over more than a decade, and Will Harrison and Keith Echelmeyer have overseen the system throughout that time. T.J. Fudge analyzed and digitized the historical aerial photographs and developed much of the GIS database. I added the video camera to the laser-altimetry system, ran the system during all of the video surveillance flights, processed all of the video data, analyzed the results and wrote the entire paper, with many ideas coming from my committee.

Chapter 1. Quantifying the Effects of Climate and Surface Change on Glacier Mass Balance*

D.H. Elsberg,¹ W.D. Harrison,¹ K.A. Echelmeyer,¹ R.M. Krimmel²

¹*Geophysical Institute, University of Alaska–Fairbanks, Fairbanks, Alaska 99775-7320, U.S.A.*

²*U.S. Geological Survey, Tacoma, Washington 98416, U.S.A.*

ABSTRACT. When a mass balance is computed using an outdated map, that computation does not reveal the actual mass change. But older maps often must be used for practical reasons. We present a method by which, with a few additional measurements each year, a mass balance computed with an outdated map can be transformed into an actual mass change. This is done by taking into account the influence of changes in areal extent and changes in the surface elevation of the glacier since the map was made. This method is applied to South Cascade Glacier as an example. The computed cumulative mass balance from 1970 to 1997 would have been 16% too negative if the 1970 map had not been updated. While the actual volume change of a glacier is relevant to hydrological studies, the change that would have occurred on a constant (or static) surface is more relevant to certain glacier dynamics problems and most climate problems. We term this the reference-surface balance and propose that such a balance, which deliberately omits the influence of changes in area and surface elevation, is better correlated to climatic variations than the conventional one, which incorporates those influences.

* This chapter was published under this title and authorship in *Journal of Glaciology*, Vol. 47, No. 159, 2001.

INTRODUCTION

The resources available to mass balance programs throughout the world are nearly as distinct and varied as the glaciers themselves, but some minimum level of data collection is necessary for mass balance calculations. For example, to compute a glacier-wide annual balance by some version of the “traditional” glaciologic method (Østrem and Brugman, 1991), specific balances, measured at several points, are integrated over a map of the glacier. Unless that map is concurrent with the specific balance measurements the results will not reflect the actual glacier change. Unfortunately, few mass balance programs have the resources to map the glacier each year. Thus the integration is likely to be performed over an outdated map, which in the extreme case may date from the beginning of the program. The resulting errors in glacier-wide annual balances may seem small, but they are systematic, and can give rise to substantial errors in a cumulative balance series constructed by summation. As we will show in an example, on South Cascade Glacier this error in the cumulative balance series is 16% of the magnitude of the cumulative mass balance over a period of 27 years and will likely continue to grow with time. One of the main purposes of this paper is to show how these errors can be removed, at least approximately, without the benefit of reliable annual maps. When computed correctly, the “conventional” mass balance is the actual ice or water equivalent change of a glacier over some specified time interval, not necessarily one year. It is useful to let the time interval approach zero, and to speak of a balance rate as a continuous function of time. Then the conventional balance rate depends upon both climate and the configuration of the surface, each of which is a continuous function of time. We introduce a different balance rate by defining the “reference surface” as the configuration of the surface as it was at some conveniently chosen time, perhaps at the beginning of a balance program or at the date of the best map. The climate still varies with time, but the reference surface is held constant. The balance rate as it would have been on this reference surface is the “reference-surface” balance rate. This is best illustrated by the extreme example given above, in which only one map is available. If each year one assumes that specific balance is a function of elevation only, and integrates

it over this original map, one is computing the reference-surface glacier-wide annual balance series for the surface defined by that map.

Because the reference-surface annual balance is calculated without an updated map, the most difficult step in determining conventional annual balance in the absence of annual maps is to find the transformation between the two balances. This is the topic of the next section. In later sections we summarize the transformation, apply it in exact form to South Cascade Glacier in order to suggest approximations necessary in typical applications, and review the data needed for the transformation. In the context of this paper, the word “transformation” refers to the change from a reference-surface balance to a conventional balance.

An important point here is that both conventional and reference-surface balances have appropriate applications, and both should be computed and reported. In hydrological studies, including water storage and sea-level change, the conventional mass balance is relevant because it is a measure of the actual change in volume of a glacier. Because a conventional mass balance incorporates both climatic forcing and surface change, the results are not simply correlated to variations in the climate. The reference-surface mass balance removes the surface change effects by holding the glacier surface constant through time, and thus is the climatically relevant mass balance. Conveying this idea is the other main purpose of this paper.

THE RELATIONSHIP BETWEEN CONVENTIONAL AND REFERENCE-SURFACE BALANCES

Mass balance notation

Our notation generally follows standard conventions: \dot{b} is used for the balance rate, and b for the balance during a specified finite time interval. We call these “specific” quantities because they are defined at a point. Note that they are measured in the vertical direction (see Rabus and others, 1996, for example). In a hydrological context it is appropriate to express b as a water equivalent thickness (and \dot{b} as a water equivalent

thickness per time), but in the context of glacier dynamics or geodetically measured balance an ice equivalent thickness is usually more appropriate. The latter will be our convention. For the glacier-wide balance and balance rates we use B and \dot{B} , in ice equivalent volume and volume per time. Balance quantities on the reference surface are designated with primes. Table 1.1 lists the variables used in this paper along with definitions and typical units.

Definition of the conventional and reference-surface glacier-wide balance rates

The actual surface is what one would find by visiting a glacier, and this surface is continuously changing. The reference surface is defined at one point in time and never changes. The relationship between conventional specific balance rate, \dot{b} , and reference-surface specific balance rate, \dot{b}' , is simple if the reference and actual surfaces are close enough that the balance rate varies linearly in the vertical direction between them. Then

$$\dot{b} = \dot{b}' + \dot{G}(Z - Z') \quad (1)$$

where the upper case symbols Z and Z' denote the elevations of the actual and reference surfaces at a given point in the map plane, and \dot{G} is the vertical derivative of the balance rate there. (The lower case symbol z will represent the independent variable of elevation.) In the general case, all of these quantities may vary with horizontal position in the map plane. We call the derivative \dot{G} the "balance rate gradient" although it is only the vertical component of the mathematical gradient. Because of the linearity assumption, $\dot{G} = \dot{G}'$.

Next we present expressions for the glacier-wide conventional and reference-surface balance rates, \dot{B} and \dot{B}' . In the case where a topographic map (or equivalently a digital elevation model), or an area distribution function (the amount of area per elevation interval of the actual surface) is available then the glacier-wide balance rates can be computed directly. These computations are often performed in practice by numerical summation methods, but we present them here in analytic form. If it is an adequate approximation to express the specific balance rate as a function of elevation z only, the conventional rate is

$$\dot{B} = \int_{\xi} \alpha \dot{b} dz \quad (2)$$

where α is the area distribution function. The integration is over ξ , the elevation range of the glacier. α and ξ may vary with time. This is a familiar expression except that it deals with the instantaneous balance rate, rather than the balance accumulated during a specified time interval. The corresponding reference surface quantity is

$$\dot{B}' = \int_{\xi'} \alpha' \dot{b}' dz \quad (3)$$

in which α' is the area distribution function obtained from the reference surface map. This integration is over ξ' , the elevation range of the reference glacier. α' and ξ' , unlike α and ξ , do not vary with time because the reference surface does not change. Assuming that the balance rate expressed as a function of elevation is not influenced significantly by changes in the glacier surface, \dot{b} can be used in place of \dot{b}' in Equation (3). This assumption may tend to break down near the transient snow line and near the edges of the glacier.

If the specific balance rate as a function of map position cannot be adequately approximated as a function of elevation then Equations (2) and (3) are replaced by

$$\dot{B} = \int_A \dot{b}(x, y) dA \quad (4)$$

and

$$\dot{B}' = \int_{A'} \dot{b}'(x, y) dA \quad (5)$$

where A' is the map area of the reference surface and x and y are the map coordinates. The integrations are carried out over the map projection of the actual surface in Equation (4) and the reference surface in Equation (5). Thus the integrands, $\dot{b}(x, y)$ and $\dot{b}'(x, y)$, are evaluated on the actual and reference surfaces, respectively. A' , unlike A , does not vary with time. Although the reference-surface specific balance rate can not be directly measured except when the actual surface is the reference surface, $\dot{b}'(x, y)$ can be computed by Equation (1). Equation (4) is the general expression for evaluating the conventional glacier-wide balance except, as in Equation (2), it deals with the balance

rate.

A relation between conventional and reference-surface glacier-wide balance rates

Equation (1) relates the specific balances on the conventional and reference surfaces. We next consider the glacier-wide balances and show how they can be expressed in terms of the difference in area and volume between the actual and reference glaciers.

We begin with the case of a glacier which has advanced relative to its reference state; the results will then be generalized to cover retreat as well. Equation (4) can be rewritten as

$$\begin{aligned}\dot{B} &= \int_A \dot{b} dA \\ \dot{B} &= \int_{A'} \dot{b} dA + \int_{\Delta A} \dot{b} dA\end{aligned}\quad (6)$$

in which ΔA is the difference between the actual and reference surface map areas, $A-A'$ (Figure 1.1 shows the reference and actual surfaces and some related items). The first term on the right hand side of Equation (6) can be evaluated by substituting Equation (1) into the integrand, and applying Equation (5). The second term on the right can be calculated using a variation of Equation (1), whereby $\dot{b} = \dot{b}_r + \dot{G}(Z - Z_r)$. The r subscript signifies evaluation at the elevation of the glacier bed or the elevation of the ground exposed by retreat (Fig. 1.1); we call this surface the bedrock surface, although it may actually be till or some other material. \dot{b}_r is found at the corresponding elevation on the specific balance rate curve, even though a specific balance cannot be measured on an ice-free surface. In the area between the reference and actual termini, ΔA , the elevation of the reference surface, Z' , is undefined, so we prescribe it to be identical to the bedrock surface elevation, Z_r , at the same horizontal position (Fig. 1.1). Then, after minor rearrangement and combination of terms Equation (6) becomes

$$\dot{B} = \dot{B}' + \int_A \dot{G}(Z - Z') dA + \int_{\Delta A} \dot{b}_r dA \quad (7)$$

A similar equation, with the first integral carried out over A' (not A), is obtained

from Equation (5) if the glacier has retreated.

In the case of retreat a few points should be noted. The surface of integration in the last term of Equation (7), ΔA , is negative by definition. Also, within ΔA we define $Z = Z_r$, instead of $Z' = Z_r$, in order to derive Equation (7). Finally, the balance curve must be extrapolated not only below the lowest measured point (as in the case of advance), but also beyond the actual glacier terminus to the reference terminus.

Equation (7) can be written in the simple form,

$$\dot{B} = \dot{B}' + \dot{G}_e \Delta V + \dot{b}_e \Delta A \quad (8)$$

where

$$\dot{G}_e = \frac{\int_{A'} \dot{G}(Z - Z') dA}{\int_{A'} (Z - Z') dA} = \frac{\int_{A'} \dot{G}(Z - Z') dA}{\Delta V} \quad (9)$$

and

$$\dot{b}_e = \frac{\int_{\Delta A} \dot{b}_r dA}{\int_{\Delta A} dA} = \frac{\int_{\Delta A} \dot{b}_r dA}{\Delta A} \quad (10)$$

Equation (8) is identical to Equation (7) but lends itself to approximations in \dot{G}_e and \dot{b}_e . \dot{G}_e is the average of \dot{G} over the entire glacier weighted to emphasize areas of large thickness change. \dot{b}_e is the average of \dot{b}_r over ΔA . ΔV is the difference between the actual and reference volumes ($V - V'$), as shown in Figure 1.1; ΔA is the corresponding difference in map area as defined previously. In case of retreat each integration in Equation (9) is over A' instead of A , making Equation (8) valid in both advance and retreat.

Equation (8) states that the difference between the reference-surface and conventional glacier-wide balance rates can be expressed by two terms, one accounting for the change in surface elevation ($\dot{G}_e \Delta V$, the "volume" or the "surface elevation" term) and one for the change in area, especially near the terminus ($\dot{b}_e \Delta A$, the "area" term).

These are usually of opposite sign since $\dot{b}_e < 0$.

Transformation between conventional and reference-surface glacier-wide annual balances

So far we have dealt only with balance rates. This was to avoid any ambiguity due to time varying surface characteristics. A balance rate, because it is defined at a specific point in time, is associated with a specific glacier surface geometry at that same moment. The balance rate at any moment in time is not likely to be a simple function of position or elevation because passing storms or instantaneous wind patterns do not follow smooth patterns. For this reason balance rates are generally averaged over either a season or a year; on these time scales definite patterns in accumulation and ablation are apparent. Nye (1965) chose to approximate the time varying balance rate by an average annual value. This is possible when changes in glacier geometry occur on time scales much greater than one year, as Nye (1965) found for his study of South Cascade Glacier. Using this approximation, the time integrated form of Equation (8) can be expressed in terms of annual balances rather than balance rates by merely dropping the time derivatives. Then the conventional annual balance for the balance year is

$$B = B' + G_e \Delta V + b_e \Delta A \quad (11)$$

Each quantity in Equation (11) (e.g., B , G_e , or ΔV) is evaluated for the balance year in question. G_e and b_e are found by corresponding time integrated forms of Equations (9) and (10). Values for ΔV and ΔA can be taken (for simplicity) to be those values found at the end of the balance year; note that they are both defined as the changes relative to the reference surface, and not relative to the beginning of the balance year.

The cumulative balance from year one to year n is then

$$B_n^{(cumul)} = \sum_{j=1}^n B_j \quad (12)$$

where B_j is the conventional annual balance for the j th year, as obtained from Equation (11). Reference-surface glacier-wide cumulative balances can be calculated by an analogous equation.

ΔV_n is the total change in volume from $t = 0$ to the end of year n . $B_n^{(cumul)}$ is the ice equivalent volume change over the same time interval. We approximate ΔV_n by $B_n^{(cumul)}$ in order to solve explicitly for the conventional glacier-wide annual balance, B_n :

$$B_n = \frac{1}{1 - (G_e)_n} \left[B'_n + (G_e)_n \sum_{j=1}^{n-1} B_j + (b_e)_n \Delta A_n \right] \quad (13)$$

This is the required transformation between a reference-surface annual balance and a conventional annual balance.

Geodetic corrections

By our convention, a geodetic balance is the ice equivalent volume change determined by comparing two maps. This could equivalently be called the geodetic cumulative balance over the interval from first map to the second. Alternatively, airborne laser surface profiling techniques can also be used to measure glacier volume change (Echelmeyer and others, 1996). If more than two maps are available then the geodetic balances, measured between each consecutive pair of maps, can be summed to form a series of geodetic cumulative balances, each one representing the total change in ice equivalent volume since the first map in the series. Such a geodetic cumulative balance series is less subject to the accumulation of systematic errors, and is thus usually more accurate than a glaciologically measured cumulative balance. The accuracy of a geodetic balance is inherently limited by the quality of the maps used.

We can use a geodetic cumulative balance series (or even one long-term geodetic balance) to determine a correction for the conventional glacier-wide cumulative balance series by requiring that they agree (in a least squares sense, if necessary) over the same time intervals. We apply this correction as a one or two parameter adjustment to the reference-surface glacier-wide annual balances. The two parameter version is

$$B'_n(\text{correct}) = c_0 + c_1 B'_n(\text{measured}) \quad (14)$$

Initial values of the coefficients are estimated and then revised by an iterative process. Each iteration involves adjusting c_0 and c_1 , transforming the “corrected” reference-surface annual balances via Equation (13), summing the transformed conventional annual values using Equation (12), and computing the root mean square deviation between the conventional and geodetic cumulative balance series. The iteration concludes when the deviation is minimized. A simple linear goal seeking algorithm, available in some spreadsheets, is a useful tool for this procedure.

In the following example on South Cascade Glacier we make the corrections to the glacier-wide balances only. This is because we believe that the main systematic errors arise in the extrapolation and integration of the specific balances over the area of the glacier, and not in the specific balances themselves. Errors in extrapolation of specific balances near the terminus are particularly significant in both advance and retreat. They affect both conventional and reference-surface balance computations.

Summary of the transformation method

Before transforming reference-surface balances into conventional balances, the following information must be gathered:

- the map which defines the reference surface
- all other available maps of the glacier
- the specific balance curve for each year in the time series
- the measured glacier area and coordinates of the glacier boundary for each year
- a map of the bedrock surface that falls within ΔA .

The transformation then follows the procedure given in the form of a flowchart in Figure 1.2. The results are time series of reference-surface and conventional balances corrected to fit to the geodetic cumulative balances (if available). In the next section we will apply this methodology to an example.

APPLICATION TO SOUTH CASCADE GLACIER

We need to choose a subject glacier in order to demonstrate the transformation between reference-surface and conventional balances. This glacier should have as much data available as possible, including a long time series of measurements, numerous repeat mappings, and easy access to the archived data. South Cascade Glacier fits these criteria. The abundance of information allows us to perform exact computations while learning to approximate those quantities that many mass balance programs are not able to evaluate exactly. Such an abundance of data also makes it possible to compute conventional mass balances for most years without going through the transformation method we have described, and this has been done previously (Table 1.2 and Krimmel, 1999b). Applying the transformation to South Cascade Glacier guided our development of the theory into a *modus operandi* and here serves to demonstrate the various steps involved.

Data

South Cascade is a small glacier in the North Cascade Mountains of Washington, USA (Meier and others, 1971). Its present area is about 2 km². The temporal changes in its area (Fig. 1.3 and Table 1.3) have been measured from ablation zone outlines. Geodetic volume change has been determined over various time intervals by airborne photogrammetry (Krimmel, 1999a). Appendix 1 describes how we computed a series of geodetic cumulative balances from these volume change measurements. It also describes how specific balance curves were fit to and extrapolated above and below the available field data. Figure 1.4 shows the geodetic cumulative balances. We plot glacier-wide balances primarily in units of volume. The secondary axis is scaled by a constant factor of $1/A'$ to yield a characteristic thickness change; this is more easily envisioned than volume change. This differs from the often used convention of plotting cumulative average specific balances, which introduces unnecessary errors in volume change computations if a glacier's area is changing significantly during the time series.

Table 1.2 is a partial summary of the data available and the methods that were used by Krimmel and others for determination of conventional glacier-wide annual

balances from 1959 to 1997 (Krimmel, 1999b). Such a diversity of data reduction methods introduces inconsistencies in the previously published conventional balance series. We reduce each year's data as consistently as possible, thereby eliminating some systematic errors. We use data only from 1970 to 1997 because consistent photogrammetric techniques were used during that period. The use of geodetic corrections, in the form of Equation (14), also make our resulting series of conventional balances differ from those previously published.

The exact transformation

There are abundant data available for South Cascade, including many repeat mappings. In this section we use all of the available data to produce a nearly exact series of conventional balances. Afterwards we look at what can be done when fewer maps are available. The first step in the flowchart (Fig. 1.2) is to compute the reference-surface glacier-wide annual balance, B' , for each year. Taking the 29 September 1970 map (in the form of a digital elevation model) as our reference surface, these balances can be computed directly by Krimmel's (1996) grid index method, using the same 1970 area distribution function for each year's calculation. The grid index method is a numerical form of Equation (3) because the specific balance is approximated as a function of elevation only. For a given year the reference-surface average specific balance is B'/A' ; from 1970 to 1997 the mean of the annual values for this quantity is -0.95 m of ice.

Next, we compute G_e for each year using a form of Equation (9) without time derivatives. This requires an annually updated map and the reference surface map because both Z and Z' are present. For those years when we have an updated map (1985-1997), we perform numerical integration of the two terms in Equation (9). The product $G(Z-Z')$ is evaluated at each grid cell dA in the reference area A' . The solid circles in Figure 1.5a show the series of G_e 's calculated in this manner. No trend with time is apparent, so from 1970 through 1984 we approximate G_e by the average of these latter results (0.024 m m^{-1} with an interannual standard deviation of 0.004 m m^{-1}).

Evaluation of the b_c 's using Equation (10), again dropping the time derivatives, requires a map of bedrock elevations within ΔA . This map can be created by several different methods. In case of retreat, a recent map should include these elevation data. Alternatively, a sampling of surveyed bedrock surface elevations which spans the ΔA region can be interpolated to approximate a topographic map there. These points may be surveyed during one field excursion or, as we chose to do in this example, assembled from the existing annual surveys of the terminus boundary. If the glacier has advanced then this data may already exist because the original map probably includes the subsequently covered bedrock surface in addition to the glacier itself.

The balance at the elevation of the bedrock surface, b_c , is found on the appropriate year's balance curve for each cell dA in the ΔA region. The bedrock elevations from the interpolated topographic map do not vary with time and the ablation zone outlines allow us to determine ΔA for each year. The solid circles in Figure 1.5b are the calculated values of b_c ; they show a positive trend with time due to the incorporation of higher elevations (and thus less negative balances) into ΔA as the terminus retreats. The average annual value of b_c is -6.16 m with an interannual standard deviation of 1.18 m.

With all the necessary values of B' , G_c , b_c , and ΔA known for every year, we now use Equation (13) to evaluate the conventional glacier-wide annual balances. Equation (12) is used to calculate the cumulative balances, and these can be compared with geodetic cumulative balances over the same time interval. In the case of South Cascade Glacier the ratio of the geodetic to the glaciologic cumulative balances over the entire interval from 1970 to 1997 is consistently about 1.5, as noted by Krimmel when analyzing his reported glaciologic and geodetic balances (1999a). Krimmel (1989) considered whether the difference over an earlier interval could be due in part to the breakdown of Sorge's Law. Our correction (see Appendix 1) takes this into account, and yet there still is a divergence between the two balances. The divergence we find falls within the range of values found by other mass balance programs for their subject glaciers. For example, we compared glaciologic and geodetic measurements for eight glaciers described in the proceedings of the August, 1998 Tarfala meeting on "Methods

of Mass Balance Measurements and Modelling.” Of those eight comparisons, one showed nearly perfect agreement (Kuhn and others, 1999), while the ratio of geodetic to glaciologic measurements in the rest ranged from -1.7 to $+1.7$ (Trabant and March, 1999, for example).

The next step is to determine the coefficients in Equation (14) by minimizing the root mean square error between the conventional glaciologic cumulative balances and the available geodetic cumulative balances. These were found to be $c_0 = -0.35 \times 10^6 \text{ m}^3$ and $c_1 = 1.16$. After correcting the reference-surface glacier-wide balances they were substituted back into Equation (13) to produce corrected conventional balances. The final conventional and reference-surface annual balances are shown in Figure 1.6, the cumulative balances (including geodetic) are shown in Figure 1.7 and all of the data plotted are listed in Table 1.3, along with the annual glacier areas. The differences between the reference-surface and conventional annual balances are fairly small over this time interval, but the differences in the cumulative balances are significant. Both differences will continue to grow with time if the current climatic conditions persist.

Approximations for the exact transformation

Now that we have some experience with calculations when there is bountiful data, we are ready to see what approximations would be necessary on a glacier with fewer or no repeat mappings. Some mass balance programs will have maps for some years other than just the reference year. For these years, G_e and b_e can be evaluated and trends may appear from which to estimate values for the unmapped years. The quality of the estimates made will depend greatly on how much data exist; without any updated maps these approximations will be difficult or impossible to make. This section contains potential estimates of G_e and b_e which we found to work with our data; some will be applicable to other glaciers, while others will not. Tests of what works best will be necessary for each mass balance program.

We find the best approximation of G_e to be 0.9 times the value of the specific balance gradient at 1733 meters on South Cascade ($r^2 = 0.58$). This corresponds with an

elevation a little less than half of that from the terminus to the equilibrium line. Figure 1.5a shows a comparison of the exact and approximate values for G_e .

As mentioned above, calculation of b_e does not require annual glacier maps. It does require annual terminus outlines and the reference terminus outline to define the ΔA region, a bedrock map in the vicinity of the terminus, and specific balances low on the glacier (in case of advance) or extrapolated below the actual terminus (in case of retreat). Two important annual field measurements in this case are the specific balance near the terminus and a survey of the terminus boundary. If even a rudimentary bedrock map is impossible to produce by the methods previously mentioned, then approximations to b_e must be used. Our exact b_e term appears to have a slight time dependence as seen in Figure 1.5b, for the reason mentioned previously. Thus we choose an approximation that is relative to the specific balance at the actual terminus elevation, b_t , for each year. In this case we find $b_e = 0.75 \times b_t$ is the best substitution ($r^2 = 0.50$, but from 1976 to 1997 $r^2 = 0.80$). Figure 1.5b shows the approximate values for b_e .

Starting with the same geodetically corrected reference-surface balances as in the exact case and using the approximate values for G_e and b_e just described, we compute the approximate conventional balances using Equation (13). The correlation between the exact and approximate annual balances is excellent, with $r^2 = 0.998$, and there is a difference in the average values of only 0.4%. The exact and approximate cumulative balances also agree almost exactly. Thus, the approximate method potentially yields results quite close to the exact method while using fewer observations as input. If the South Cascade Glacier mass balance program no longer had the resources to map the glacier annually, then both of these approximations would aid in the continuation of an accurate time series of conventional mass balances.

The best approximations for G_e and b_e will most likely be different on other glaciers due to the surface and bed geometries, the shape of the specific balance curve, and the amount of advance or retreat. If there is at least one repeat mapping then we suggest calculating G_e for that (those) year(s) and looking for a similar connection with elevation. Otherwise, we recommend using the specific balance gradient at an elevation

halfway between the terminus and the equilibrium line. As mentioned above, other mass balance programs are less likely to require an approximate form of b_e . In case some approximation is required, then $0.75 \cdot b_e$ is probably the best choice.

Cumulative effects of geometry changes on mass balance

The 1997 reference-surface cumulative balance since 1970 is 16% more negative than the conventional one. This difference is due in part to recession of the terminus, which reduces the size of the ablation area and brings the glacier closer to equilibrium, and in part to lowering of the surface, which shifts the glacier into a more negative balance regime and counters some of the effects of the area change. Figure 1.7 is a plot of the annual values of both the area and volume terms from the exact and approximate transformations. From 1970 to 1997 the cumulative effect of the volume term was 60% as large as that of the area term, and it was of opposite sign.

DISCUSSION

What measurements are needed?

In order to apply these ideas, mass balance researchers need to measure the following, either remotely or in the field:

- annual terminus position and elevation as far up the sides and of such spatial resolution as is practical or necessary for two applications—to quantify area changes and to contribute to a bedrock map
- bedrock elevations at points previously unsurveyed but within ΔA
- specific annual mass balance as low on the glacier as possible because of the rapidly varying balance curve there.

These measurements, in conjunction with the data reduction methods presented here, can reduce systematic errors in the derived balances.

Some programs will be able to remap the glacier only infrequently, and the

surface may change significantly between successive maps. In order to compute the most accurate conventional balances possible, the newest map (assuming map accuracy is comparable) should be used. In the intervening years before the next map is made, our methodology will again have to be called upon. The original reference surface map should still be used when reporting reference-surface balances so that its time series is both continuous and consistent.

Choice of the reference surface

One of our underlying points is that variations in the surface over which specific balance measurements are integrated directly affect the glacier-wide balance. By the same logic, the choice of the reference surface will affect the reference-surface glacier-wide balance. With the help of Equation (11) it can be shown that the difference between the glacier-wide annual balances on two different reference surfaces will be approximately constant over the years, with only small fluctuations due to interannual variations in G_c and b_c . Cumulative balances are even more sensitive to the choice of reference surface. The trend in the difference between the glacier-wide cumulative balances on two different reference surfaces will grow approximately linearly with time. Logically it makes the most sense to choose the reference surface to be the glacier surface at the beginning of the time series, but whatever the choice the reference surface must be clearly defined.

A large difference between the chosen reference surface and the actual surface reduces the accuracy of Equation (1) because the linearity assumption upon which the equation was based is unlikely to remain valid. Another assumption we made was that changes in the glacier surface do not significantly affect balance rate as a function of elevation. This allowed us to substitute \dot{b} for \dot{b}' in Equation (3), but large deviations between the reference and actual surfaces weaken this assumption as well. Temporal and spatial variations in environmental variables, including surface albedo, solar input, wind patterns, and proximity to rock surfaces, help to undermine both of these assumptions.

Relevance of the reference-surface balance to glacier dynamics and climate studies

The concepts described here can be used as the basis for a new and simple approach to the theory of glacier response to climate. This results when Equation (8), a statement of the conservation of mass, is combined with a functional relationship between area and volume which specifies the dynamics of flow (Harrison and others, 2001).

These ideas also have a bearing on climate studies. By removing the effects of changing surface configuration on mass balance, reference-surface balances are more closely related to trends in climate than are conventional balances. The following example demonstrates that conventional mass balance is not always well correlated with climate variations. If a glacier initially in equilibrium experiences a permanent step increase in summer temperature, by the mechanisms of glacier flow it will usually adjust its length and thickness until equilibrium with the new climate is reached. The initial and final conventional balance rates are the same (zero), but the initial and final surfaces, and the climate, are different. This illustrates the non-unique relationship between conventional balance and climate, and one of the difficulties in connecting the two. The reference-surface balance on the same glacier, under the same conditions, will experience a permanent step decrease coincident with the climate change. Because the reference surface does not adjust itself, the reference-surface balance will continue to reflect the permanent change in climatic conditions.

CONCLUSIONS

We have presented a method by which glaciologists can compute a change in glacier mass from specific balance measurements, without the benefit of an up-to-date map. Changes in both glacier area (the area term in Equation (11)) and in surface elevation (the volume term in Equation (11)) since the time when an older map was made must be taken into account. Both of these terms are vital aspects of glacier response to climatic forcing (Harrison and others, 2001). In addition, reference-surface balances which measure the balance on an unchanging surface, and not conventional balances, are

required for studies of glacier dynamics and climate change. For this reason, reference-surface balances should be routinely reported along with conventional balances.

A separate and possibly more significant issue is the often observed difference between geodetic and glaciologic measurements of a glacier's mass balance. To this end, we believe that the first priority of mass balance programs should be to understand and control the large systematic errors that seem to plague most glacier-wide balance estimates made by glaciologic methods.

ACKNOWLEDGEMENTS

This work was supported by the United States National Science Foundation program under grant number OPP97-07515. We would like to thank Dennis Trabant, Rod March, Joe Sapiano and Jeff Schmok for their assistance and input. Tómas Jóhannesson was helpful beyond the call of duty, not only performing as an extraordinary scientific editor, but also serving as one of the peer reviewers. His insights into this topic were an invaluable help in redirecting the focus of this paper. The three other reviewers, Michael Kuhn, Roger LeB. Hooke, and one reviewer who was anonymous, provided extensive helpful comments as well.

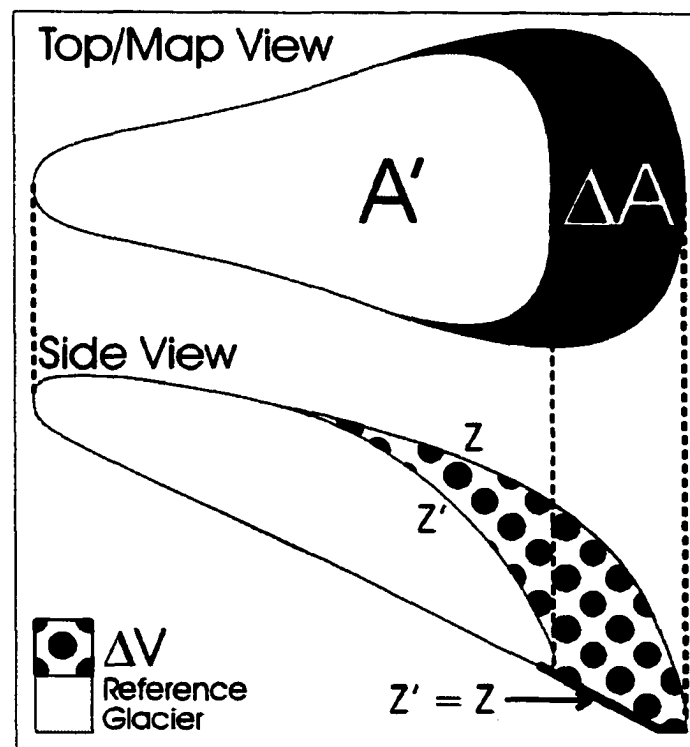


Figure 1.1: Schematic of a glacier. Schematic of a glacier which has advanced since the reference surface was defined. A' is the map area of the reference surface; ΔA is the change in map area due to advance; ΔV is the increase in volume; Z , Z' , and Z_r are the elevations of the conventional, reference, and bedrock surfaces respectively.

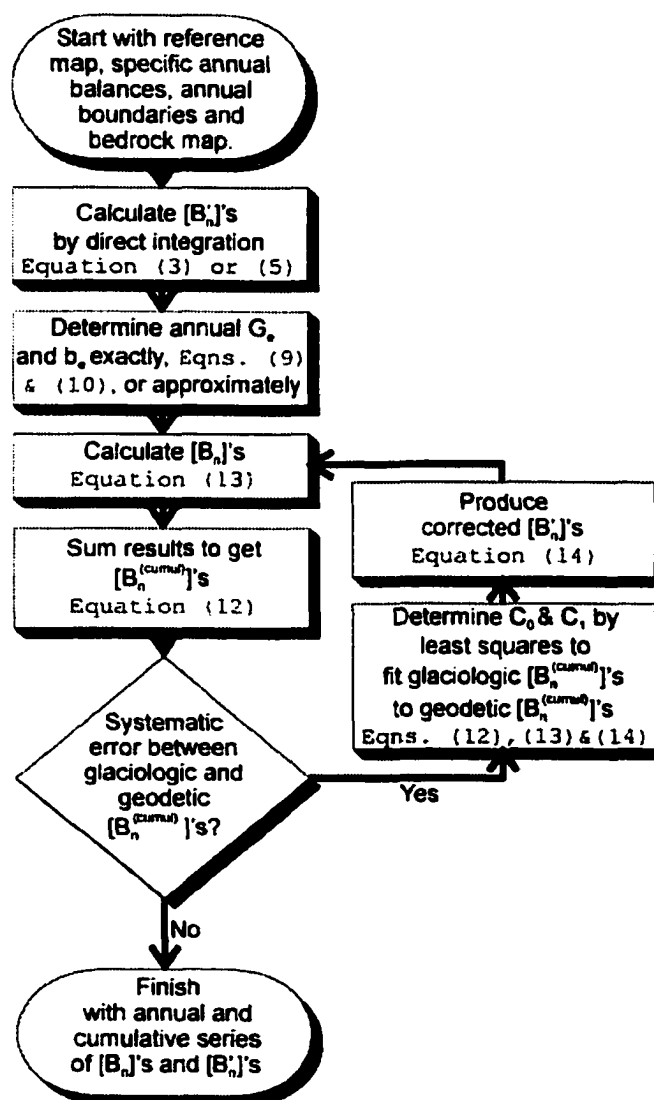


Figure 1.2: Flow chart. Flow chart of the steps and equations used to compute reference-surface glacier-wide balances and transform them into conventional balances.

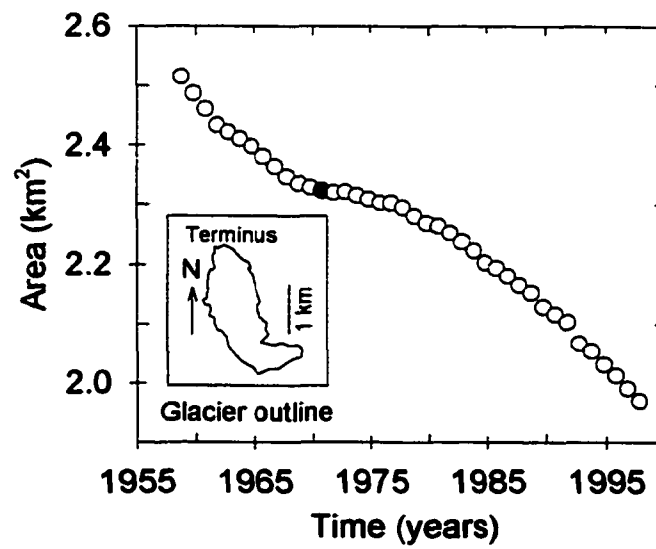


Figure 1.3: South Cascade area. South Cascade Glacier map area since September, 1958, and an outline of the reference surface. The solid black circle represents the area at the time when the reference surface was defined (29 September 1970).

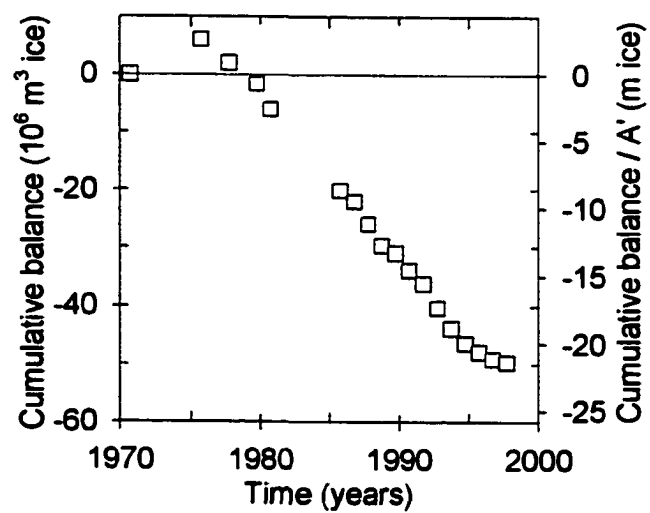


Figure 1.4: Geodetic cumulative balance. Geodetic cumulative balances for South Cascade Glacier since 1970.

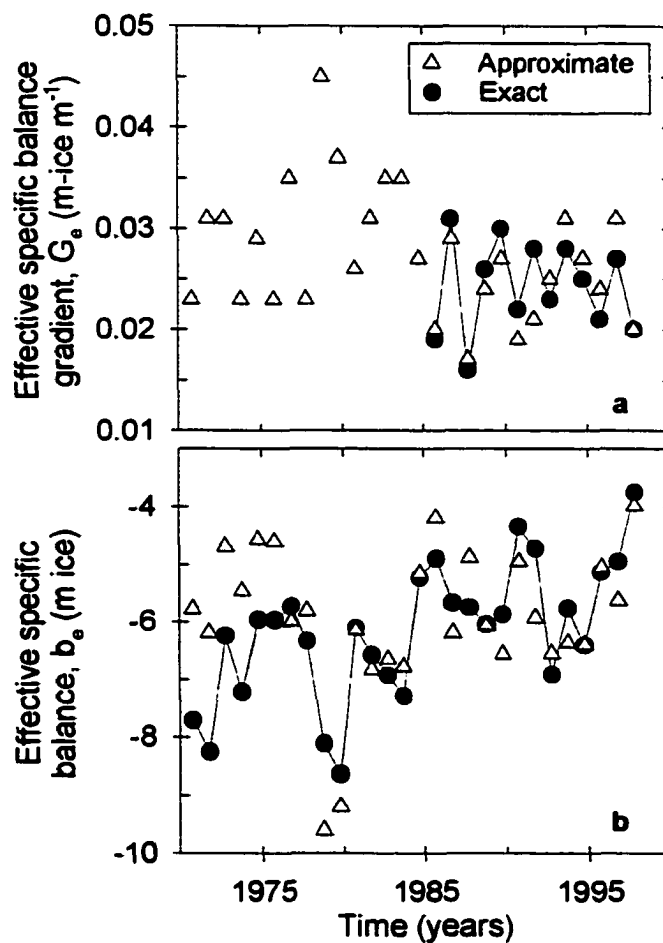


Figure 1.5: Effective gradients and balances. (a) Exact and approximate values of G_e for South Cascade Glacier. Each year the approximate value is taken to be 90% of the value of G at 1733 m. (b) Exact and approximate values of b_e for South Cascade Glacier. Each year the approximate value is taken to be $0.75 \times b_t$, where b_t is the specific balance at the elevation of the actual glacier terminus.

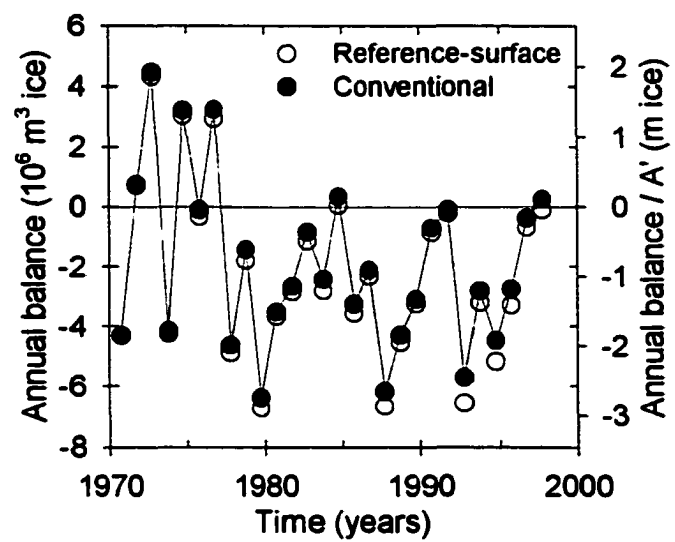


Figure 1.6: Annual balances. Conventional and reference-surface annual balances for South Cascade Glacier.

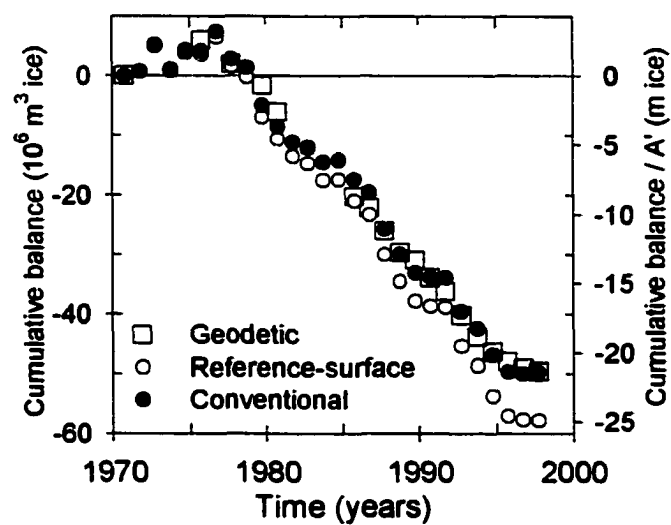


Figure 1.7: Cumulative balances. Conventional, reference-surface and geodetic cumulative balances for South Cascade Glacier since 1970.

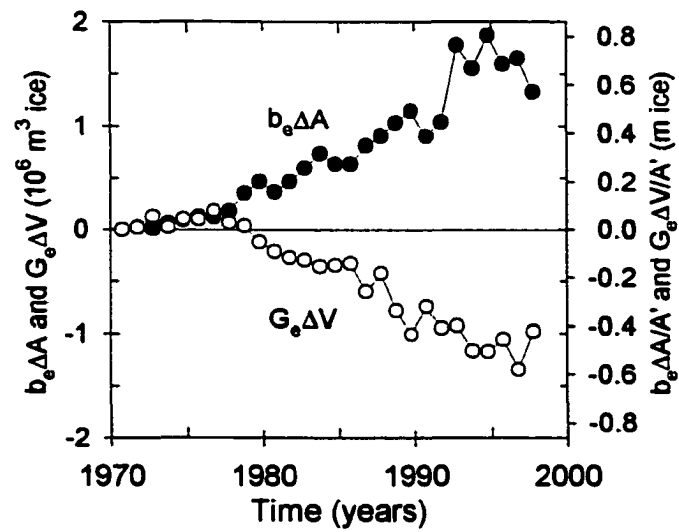


Figure 1.8: Area and volume terms. South Cascade Glacier annual values for the volume and area terms in Equation (13).

Table 1.1: Table of variables. Key variables used throughout the paper, along with definitions and typical units (all balances are given in ice equivalent units)

<i>Variable</i>	<i>Definition</i>	<i>Units</i>
x'	Primed quantities are on the reference surface	
\dot{x}	Dotted quantities are rates	a^{-1}
$x^{(cumul)}$	(<i>cumul</i>) superscript implies accumulation over many years	
\dot{b}	Conventional specific balance rate	$m a^{-1}$
b	Conventional specific balance (over some time interval)	m
\dot{b}'	Reference-surface specific balance rate	$m a^{-1}$
b'	Reference-surface specific balance	m
B	Glacier-wide balance	m^3
A	Map area	m^2
\dot{G}	Specific balance rate gradient, $\partial \dot{b} / \partial z$	$m m^{-1} a^{-1}$
G	Specific balance gradient, $\partial b / \partial z$	$m m^{-1}$
Z	Elevation at a point on the surface	m
x, y, z	Independent variables of position	m
ξ	Altitude range of glacier in limits of integration	m
α	Area distribution function, $\alpha(z)$	$m^2 m^{-1}$
ΔA	Difference in actual map area from the reference surface area	m^2
ΔV	Difference in actual volume from the reference glacier volume	m^3
\dot{G}_e	Weighted average of \dot{G} , with weighting given by amount of elevation change from the reference glacier	$m m^{-1} a^{-1}$
$b_r; b_e$	Specific balance on the bedrock surface; average of b_r over entire ΔA region	m
$b_t; b_r$	Specific balance at the reference terminus elevation; actual terminus elevation	m

Table 1.2: Balance methods. Density of balance stake measurements, methods used for integration of previously published conventional glacier-wide balances, and availability of airphotos for South Cascade Glacier, as reported by Krimmel (1999b).

<i>Time interval</i>	<i>Balance stake density km⁻²</i>	<i>Integration method used in previous analyses</i>	<i>Airphotos available</i>
1958-1973	>10	gridding of hand-contoured map	1958, 1961, 1970
1974-1982	2-3	gridding of hand-contoured map	1975, 1977, 1979, 1980
1983-1985	0.5 (1 index stake)	correlation with earlier balances (see Krimmel, 1989)	1985
1986-1997	0.5-3	grid index (see Krimmel, 1996)	1986-97

Table 1.3: Area and balances. South Cascade Glacier area, annual and cumulative reference-surface and conventional glacier-wide balances, and geodetic cumulative balances. The conventional cumulative balances have been fit, by the method of least squares, to the geodetic cumulative balances.

Balance year	Area 10^6 m^2	Annual		Cumulative		
		Reference-surface $10^6 \text{ m}^3 \text{ ice}$	Conventional $10^6 \text{ m}^3 \text{ ice}$	Reference-surface $10^6 \text{ m}^3 \text{ ice}$	Conventional $10^6 \text{ m}^3 \text{ ice}$	Geodetic $10^6 \text{ m}^3 \text{ ice}$
1970	2.32	-4.30	-4.30	0.00	0.00	0.00
1971	2.32	0.71	0.75	0.71	0.75	
1972	2.32	4.32	4.46	5.03	5.21	
1973	2.32	-4.24	-4.16	0.78	1.05	
1974	2.31	3.03	3.22	3.81	4.27	
1975	2.30	-0.32	-0.10	3.49	4.17	6.05
1976	2.30	2.94	3.25	6.43	7.42	
1977	2.30	-4.88	-4.63	1.55	2.79	1.99
1978	2.28	-1.80	-1.42	-0.25	1.37	
1979	2.27	-6.73	-6.38	-6.99	-5.02	-1.63
1980	2.26	-3.68	-3.52	-10.67	-8.54	-6.06
1981	2.25	-2.85	-2.66	-13.52	-11.20	
1982	2.24	-1.14	-0.83	-14.66	-12.03	
1983	2.22	-2.81	-2.42	-17.47	-14.46	
1984	2.20	0.05	0.34	-17.43	-14.12	
1985	2.19	-3.56	-3.25	-20.99	-17.37	-20.13
1986	2.18	-2.32	-2.11	-23.32	-19.48	-22.02
1987	2.17	-6.66	-6.18	-29.98	-25.65	-25.91
1988	2.15	-4.54	-4.28	-34.52	-29.93	-29.62
1989	2.13	-3.26	-3.11	-37.77	-33.05	-30.90
1990	2.12	-0.86	-0.70	-38.63	-33.74	-33.84
1991	2.10	-0.20	-0.11	-38.83	-33.85	-36.13
1992	2.07	-6.56	-5.71	-45.39	-39.56	-40.28
1993	2.05	-3.21	-2.82	-48.60	-42.38	-43.82
1994	2.03	-5.18	-4.48	-53.78	-46.85	-46.37
1995	2.01	-3.29	-2.75	-57.07	-49.60	-47.88
1996	1.99	-0.68	-0.38	-57.75	-49.98	-49.12
1997	1.97	-0.10	0.25	-57.85	-49.73	-49.62

REFERENCES

Echelmeyer, K.A., *and 8 others*. 1996. Airborne surface profiling of glaciers: a case-study in Alaska. *J. Glaciol.*, **42**(142), 538-547.

Harrison, W.D., D.H. Elsberg, K.A. Echelmeyer, and R.M. Krimmel. 2001. On the characterization of glacier response by a single time scale. *J. Glaciol.*, **47**(159), 659-664.

Krimmel, R.M. 1989. Mass balance and volume of South Cascade Glacier, Washington, 1958-1985. In Oerlemans, J., *ed. Glacier fluctuations and climatic change*. Dordrecht, Kluwer Academic Publishers, 193-206.

Krimmel, R.M. 1996. Glacier mass balance using the grid-index method. In Colbeck, S.C., *ed. Glaciers, ice sheets and volcanoes: a tribute to Mark F. Meier. CRREL Spec. Rep. 96-27*, 62-8.

Krimmel, R.M. 1999a. Analysis of difference between direct and geodetic balance measurements at South Cascade Glacier, WA. *Geogr. Ann.*, **81A**(4), 653-658.

Krimmel, R.M. 1999b. Water, ice, meteorological, and speed measurements at South Cascade Glacier, Washington, 1998 balance year. *U.S. Geological Survey Water-Resources Investigations Report 99-4049*.

Kuhn, M., *and 5 others*. 1999. Measurement and models of the mass balance of Hintereisferner. *Geogr. Ann.*, **81A**(4), 659-670.

Meier, M.F., W.V. Tangborn, L.R. Mayo, and A. Post. 1971. Combined ice and water balances of Gulkana and Wolverine Glaciers, Alaska and South Cascade Glacier, Washington, 1965 and 1966 hydrologic years. *Geological Survey Professional Paper 715-A*. Washington, DC, U.S. Government Printing Office.

Nye, J.F. 1965. A numerical method of inferring the budget history of a glacier from its advance and retreat. *J. Glaciol.*, 5(41), 589-607.

Østrem, G., M. Brugman. 1991. *Glacier Mass-Balance Measurements, a manual for field and office work*. Saskatoon, National Hydrology Research Institute Science Report No. 4, 129-31.

Rabus, B., W.D. Harrison and K.A. Echelmeyer. 1996. Comments on "The use of planimetric surface area in glacier mass-balance calculations: a potential source of errors" by Jacobsen and Theakstone. *J. Glaciol.*, 43(142), 588.

Sorge, E. 1935. Glaziologische Untersuchungen in Eismitte. In F.A. Brockhaus *Wissenschaftliche Ergebnisse der Deutschen Groenland-Expedition Alfred Wegener 1929 und 1930/31*. Leipzig. 3, 270 pp.

Trabant, D.C. and R.S. March. 1999. Mass-balance measurements in Alaska and suggestions for simplified observation programs. *Geogr. Ann.*, 81A(4), 777-789.

APPENDIX 1.0: DETAILS OF MASS BALANCE CALCULATIONS

The appendix includes details of the methods used for balance calculations on South Cascade Glacier.

COMPUTING A GEODETIC CUMULATIVE BALANCE SERIES

Differencing of glacier maps yields geodetic volume changes which we want to use to correct the ice equivalent glaciologic balances. We must adjust the geodetic volume changes because Sorge's Law, which states that the density structure of a glacier stays constant with time under certain conditions (Sorge, 1935), is not strictly valid on most glaciers, especially during periods of thinning (Krimmel, 1989). During periods of negative balance both firn and ice are lost at middle elevations, while in the upper accumulation zone and the lower ablation zone, changes in volume are assumed to be of ice only. Because firn has a lower density than that of ice, the average density of lost material at mid-elevations is between those of firn and ice. Krimmel (1989) estimated the fractional areas for these three elevation zones on South Cascade Glacier as such: low (ice) = 1/4, mid (firn & ice) = 1/2, and high (ice) = 1/4. He then reported a firn density profile which shows an average of approximately 700 kg/m³. With this, and an ice density of 900 kg/m³, we compute the glacier-wide weighted average density of the lost volume to be 850 kg/m³. This modest 5.5% correction in density decreases the magnitude of the geodetic volume changes (of mixed firn and ice) on South Cascade Glacier, yielding ice equivalent balances. These balances are summed over time to give a geodetic cumulative balance series. Because of this density correction, substituting the geodetically corrected $B^{(cumul)}$ for ΔV in Equation (13) undervalues the volume term by 5.5%, but for simplicity we do not correct for this.

EXTRAPOLATION OF BALANCE-ELEVATION CURVES

To evaluate the time integrated form of Equation (3), it is necessary to fit balance-elevation curves to the field data and to extrapolate these curves to the positions of the

terminus and head of the reference glacier. The curves thus extend below and above the range of field measurements made each year. To do this we usually fit a quadratic curve to the measured specific balances. In some years the paucity of data does not permit a fit to be determined, so either a constant offset is added to an average balance curve to fit the existing data (twice), or the quadratic fit is limited to some maximum balance to yield a reasonable curve (four times). We find the computed reference-surface balances to be relatively unaffected by reasonable variations in the extrapolation of the measured balance-elevation curves down to the reference terminus elevation. For example, ± 2 m variations in the balance curves at the reference terminus (corresponding to observed variability in annual values for the extrapolated b_r .) typically changed the reference-surface average annual balance by ± 0.4 m—less than one-tenth of the maximum variability in reference-surface average annual balances.

Chapter 2. Depth- and time-dependent strain rates and their variations at Siple Dome, Antarctica*

D. H. Elsberg,¹ W. D. Harrison,¹ E. Husmann,² J. L. Morack,¹ E. C. Pettit,³ E. D.
Waddington,³ M. A. Zumberge²

¹*Geophysical Institute, University of Alaska Fairbanks, Fairbanks, Alaska 99775-7320, U.S.A.*

²*Scripps Institution of Oceanography, University of California San Diego, La Jolla, California 92093-
0225, U.S.A.*

³*Dept. of Earth and Space Sciences, University of Washington, Seattle, Washington 98195-1310, U.S.A.*

ABSTRACT. Two independent strain-gauge systems were used to measure the strain rates as functions of depth and time at Siple Dome, Antarctica from January 1998 until January 2002. The gauges were deployed at the ice divide and at a location 7 km to the NE on the flank. One system employed optical fibers to measure single- and multi-year average strain rates over five depth intervals spanning the ice thickness. The other used one-meter resistance wires in a Wheatstone bridge configuration to measure strain approximately hourly at 12 discrete depths at each of the two deployment sites. The long-term average strain rates from the two systems agreed to within 16%, with the resistance-wire gauges reading higher compressive rates. The time-dependent strain rates measured beneath the divide by the resistance-wire gauges included intermittent strain events lasting up to 24 hours. We used the results from each system to compute an age-depth relationship. Assuming a time-independent ice flow geometry, the ice at the bed is older than the Wisconsin ice age.

* This chapter is in preparation for submission to *Journal of Glaciology*.

INTRODUCTION

Ever since the mapping of several fast flowing ice streams which carry large quantities of ice from the interior of the West Antarctic Ice Sheet to the Ross Sea there has been much interest in the ice-transport mechanisms of the region (e.g., Zumberge and others, 1969; Hughes, 1973; and Rose, 1979). There is evidence that, on time scales of decades or centuries, the locations and velocities of some of the ice streams have varied (e.g., Alley and Whillans, 1991). One site which has not been over-run by ice streams in at least the last 10 ka is the current location (Fig. 2.1) of Siple Dome (Nereson and others, 1998), which spans 120 km across from Kamb Ice Stream (variant name: Ice Stream C) to Bindschadler Ice Stream (variant name: Ice Stream D) and reaches 620 m a.m.s.l. at the summit (Raymond and others, 1995a). This long-term stability suggests that the ice stratigraphy is simpler than in portions of the ice sheet which have been over-run more recently by ice originating inland. We used two independent instrument systems to measure the depth-dependent vertical strain rates in the ice at Siple Dome from January 1998 through January 2002. The measurements were motivated by our interest in a constitutive flow relationship for ice which is valid across a broad range of deviatoric stresses found in nature (Pettit and Waddington, submitted, April 2002) and in interpreting and dating the deep ice core recently drilled at an adjacent site. The measured strain rates showed variations on time scales of hours, months, and years.

To carry out these measurements, we used two complementary types of strain gauges: a fiber-optic system which has a high level of long term stability, and a resistance-wire system which makes measurements over time and length scales several orders of magnitude shorter than the fiber-optic system. We deployed the gauges in the ice beneath two sites on Siple Dome in December 1997 and January 1998. Day 1 of the experiment was defined as 1 January 1998. We returned to Siple Dome approximately annually for four years to collect data and maintain the gauges. (The field visits were centered around days 376, 704, 1057 and 1463.) The two measurement locations were Divide, directly beneath the current flow divide ($81^{\circ} 39.3' \text{ S}$, $148^{\circ} 49.3' \text{ W}$), and Flank, beneath a site 7 km to the Northeast ($81^{\circ} 35.7' \text{ S}$, $148^{\circ} 41.6' \text{ W}$). Divide is located

approximately 500 m north of the deep ice core site (Binschadler, 1995). The ice thickness is 1004 m at Divide and 980 m at Flank (Gow and Engelhardt, 2000). (All depths in this paper are given as vertical distances below the surface.) Measurements of shallow firn cores (Gregg Lamorey, personal communication, 2002) show that the density is still increasing at 80 m. Strain rates measured throughout the firn using visual markers suggest that firn compaction continues below 80 m depth (Robert Hawley, personal communication, 2003).

The fiber-optic gauge design and results collected as of the November 2000 field visit have been published previously (Zumberge and others, 2002), so we begin with only a brief review of the fiber-optic system design. We then describe the resistance-wire system, including the gauge design, laboratory testing and calibration results, and field installation. Next we compare the two types of gauges. The results, and discussion and summary sections focus mainly on the resistance-wire measurements, but also present the complete set of fiber-optic measurements.

INSTRUMENTATION

Fiber-optic system design

The fiber-optic measurement system is made up of optical-fiber cables embedded in the ice and a custom modified portable surveying electronic distance meter (EDM). The optical-fiber cables, each one made up of two optical fibers loosely jacketed by a stainless steel tube with an outside diameter of 1.2 mm, reach from a surface marker emplaced at the time of installation down to a bottom anchor frozen into the ice. Each fiber was initially stretched 0.1 to 0.2 % by a weight attached to the bottom anchor. At the bottom of each cable, the two optical fibers are fusion-spliced together and at the surface each end is terminated with a polished optical-fiber connector. The EDM was modified to focus a light pulse into one of the optical-fiber connectors and receive the return signal from the other connector. The length measured by the EDM is an optical path length. In the laboratory, sample fibers were stretched by known distances and simultaneously measured by the EDM to determine a calibration factor, or strain-

sensitivity factor. Zumberge and others (2002) estimate that uncompensated temperature effects account for 1 mm of uncertainty in the fiber length measurements; this is included in the reported strain rate uncertainties. The stability of the system was monitored by repeat measurements of fibers of known lengths in the laboratory and in the field; no large unexpected errors were found.

We installed fiber-optic gauges in ten holes, five at Divide and five at Flank. The fibers range in length from 80 to 985 m. During each field visit, we used the EDM to measure the optical path lengths of all the gauges from four to 11 times over a five to 20 day interval. The instrumentation was incapable of year-round logging. Using all of the optical path length records over time, together with the strain-sensitivity factor, we calculated displacements of the surface markers relative to the bottom anchors. The rates of change of the fibers were one of the sources of data in our calculation of an age-depth relationship of the ice at Divide. Differencing the displacements gives the average strain rates over the depth intervals from each bottom anchor to the next deeper bottom anchor during the time intervals between field visits. We placed an 80-m fiber in every hole so that we could account for any horizontal inhomogeneities in the strain field due to a spatial dependence of firm compaction, but we did not observe such variations among the gauges at either of the two sites. Starting at 80 m, the successive fibers increase in length by 180 m at Divide and 170 m at Flank; the exact depth intervals are listed in Table 2.1. The uncertainties associated with the reported strain rates combine the displacement uncertainties and the RMS residuals to the linear fits of displacement versus time.

Resistance-wire system design

The resistance-wire (referred to as r-wire in what follows) strainmeter design used in this experiment was modified slightly from the one described by Harrison and others (1993). The gauges (Fig. 2.2) use a four-wire Wheatstone bridge, with three of the 0.08 mm diameter constantan alloy resistance wires (the 3/4 bridge) coiled up inside a hollow, cylindrical bridge casing. The “active” resistance wire (also 0.08 mm diameter) and the thicker, loosely hanging “return” wire (0.38 mm diameter) hang below the bridge casing

down to a common solder point on the 100 g bottom anchor. Changes in the length of the approximately one-meter active wire are sensed as changes in the balance of the bridge. This same design has also been used on several valley glaciers, including Black Rapids (Raymond and others, 1995b) and Trapridge (Kavanaugh and Clarke, 2001).

Harrison and others (1993) describe using “dummy” strainmeters to monitor long term stability of the system—both gauges and dataloggers. Dummy gauges are designed such that all four resistance wires of the Wheatstone bridge are coiled up inside the bridge casing, and therefore physically isolated from the deforming ice. Records from some dummy gauges installed in the ablation areas of valley glaciers showed excellent stability while others exhibited a monotonic drift on the order of $100 \mu\epsilon \text{ a}^{-1}$, far too unstable for the current experiment; so we modified the gauge design to minimize drift.

One source of gauge instability is the solder connections, so we used gold-coated feed-throughs and connecting pins throughout the gauges, cleaned and etched the wire ends with either a rosin or acid flux prior to soldering, rinsed off the assembled 3/4 bridges and dummy full bridges in an ultra-sonic cleaner, and painted all exposed solder joints with an insulating varnish to minimize leakage current and to relieve stress concentrations on the fine wire. Before deployment, the bridge casings were flushed with nitrogen gas to minimize corrosion from contact with oxygen and residual moisture, and were then closed off using molded-rubber oceanographic electrical connectors with o-ring seals to prevent water leakage before hole freeze-up.

The original strainmeter design was also modified in an attempt to decouple mechanically the downward motion of the instrument cable and bridge casing from the active strain wire (Fig. 2.2) by adding a decoupling anchor approximately 5 cm below the bridge casing. The weight of the lower gauge parts was supported by three pieces of fine thread connecting the bridge casing to the decoupling anchor.

Laboratory testing

The fully assembled r-wire gauges were tested over a period of five months in temperature regulated cold chambers, held at -7°C . All of the gauges were clamped

vertically under slight tension to Invar steel alloy rods. Diurnal fluctuations and long-period drift in the chamber temperatures, along with temperature differentials from the tops of the gauges to the bottoms, make the laboratory test data inapplicable to field conditions. Temperatures in the ice are probably as close to steady state as found anywhere in the world, while temperatures at the surface (where the dataloggers remained during the experiment) fluctuate both diurnally and seasonally to a much greater extent than in the laboratory. Environmental electronic noise in the building may have also affected the laboratory measurements. The cold-chamber testing did allow us to identify gauges with excessive drift or sudden jumps in strain readings, which we opened up and inspected. Typically, defective solder joints were found and repaired.

Campbell Scientific 21X dataloggers were used to measure the level of bridge imbalance in logger units (LU), defined as (see Fig. 2.2 for symbol definitions):

$$LU = 1000 \left(\frac{V_{out}^+ - V_{out}^-}{V_{in}^+ - V_{in}^-} \right).$$

By calibrating 14 of the gauges at known states of strain we computed a conversion (or gauge factor) from LU to $\mu\epsilon$ (where $\mu\epsilon$ is equivalent to parts per million strain) which is valid under laboratory conditions. Some gauges were calibrated multiple times for a total of 32 independently measured gauge factors. The average measured gauge factor was $0.500 \times 10^{-3} \text{ LU } \mu\epsilon^{-1}$ and was found to be insensitive to ambient temperature from -15 to $+20$ °C. We used this average gauge factor in all strain calculations. There are three aspects which contribute to the uncertainty associated with this gauge factor: the repeatability of the gauge-factor measurement on one gauge, the variability of the gauge factors measured on multiple gauges, and any systematic errors due to the method of measuring the gauge factor. These three uncertainties are $(0.006, 0.006, \text{ and } 0.012) \times 10^{-3} \text{ LU } \mu\epsilon^{-1}$ respectively, and the quadrature sum is $0.015 \times 10^{-3} \text{ LU } \mu\epsilon^{-1}$, or 3% of the average gauge factor. Each gauge-factor measurement took less than an hour in laboratory conditions, so this uncertainty does not include any time-dependent effects, nor any errors (which we will discuss later) associated with actual field installation conditions.

Deployment and freeze-in

The r-wire gauges were emplaced in December 1997 and January 1998 at the two sites, Divide and Flank. We used a motorized winch to lower each gauge by the attached instrument cable into its own hole up to six hours after hot-water drilling by the California Institute of Technology drilling team. Thirteen active gauges and two dummy gauges were installed at 11 depths at each site, laid out in a grid with approximately 2 m separating adjacent holes. By monitoring the strain in the gauges as we lowered them, we were able to adjust the winch speed such that the r-wires did not go slack. We were also able to confirm that the gauges did not touch the sides of the holes, except momentarily, suggesting that the holes were vertical over length scales of a few meters and greater. Despite our precautions, we broke four active wires at the solder junctions during the lowering process. We immediately retrieved each gauge, reattached or replaced the active wire, and redeployed it. In hindsight, a lighter lower anchor would have made installation easier, as the current design places a static load on the active wire of 1/2 to 1/3 of its tensile strength, leaving a narrow margin of safety to account for dynamic shocks on the way down the hole.

Each of the eight dataloggers logged from one to four gauges year-round for the duration of the experiment. The gauges were sampled at intervals between 30- and 90-minutes and at a resolution of about $0.6 \mu\epsilon$ or $2 \mu\epsilon$, depending on the voltage range we chose for each of the input channels. All of the active strainmeters produced a wildly varying initial transient signal during the freeze-in process, which lasted up to a week. Two active gauges at Divide and one at Flank failed during this period, most likely because the active wires yielded under the stress of hanging too long before freezing in. (We had observed similar failures in the lab with free-hanging gauges.) The deeper gauges, located in relatively warm ice, took the longest time to freeze in and thus were most prone to breaking. Less massive lower anchors on the deeper gauges should alleviate this problem while still pre-tensioning the active wires adequately. (The

smallest strain rates are found near the bed, so the deeper gauges require less total dynamic range than the shallower ones.)

One gauge at Divide did not fail during freeze-in, but the output drifted at an impossibly high extensional strain rate for the duration of the experiment. We never discovered its failure mode. Out of the 26 active gauges we installed, four failed without producing useful data (three at Divide and one at Flank).

Gauge-design comparison

The two types of gauges differed in many respects. While the r-wire gauge length is approximately 1 m or nearly a point measurement compared to the ~1000 m thickness of the ice sheet, the fiber-optic strain rates were computed differentially over effective gauge lengths of 170 m or 180 m, resulting in depth-averaged rates over the intervals. This means that the r-wire gauges were orders of magnitude more sensitive to anchor-to-ice coupling and interactions, and to depth-dependent variations in strain rate. For example, there might have been localized anomalous ice flow caused by the r-wire instrument cable and bridge housings. Also, because the hole freezing process proceeded from the top down (starting where the ice sheet is coldest), residual anomalous stresses were concentrated toward the bottom of each re-frozen hole. This caused localized time- and depth-dependent disturbances in the strain field which would affect an entire r-wire gauge, while affecting only the lower portion of a fiber-optic gauge. This would also be the case with naturally occurring variations in strain rate over length scales on the order of one to 10 m.

The two gauge systems also differ in the time domain. By leaving dataloggers in the field, we were able to measure a continuous signal of strain over time with the r-wires, whereas the optical fibers were measured approximately annually, yielding only single- and multi-year averaged strain rates. Furthermore, the very nature of the measurements made by each gauge type was different. The r-wire system sensed the change in strain of each active wire by measuring the change in the balance of the Wheatstone bridge. The fiber-optic system was used to make repeat measurements of the

absolute length of each fiber, from which we computed the strain over several depth intervals. With these differences in mind, we will now present the results from both systems.

RESULTS

In this section we present the data, processing techniques, and derived strain rates. We also describe time-dependent variations in strain rates. A discussion and summary of our findings will be reserved for the following section.

Data overview

Figure 2.3a shows the entire four-year series of strain versus time for two of the active r-wire gauges (167 m and 514 m Flank gauges). The slope of strain versus time is the strain rate, and the distribution of strain rate with depth as calculated from all of the active r-wire gauges is plotted in Figure 2.4a. The strain rates measured with optical fibers are plotted in Figures 2.4b and 2.4c, along with r-wire results, which have been averaged over the same depth intervals as those sampled by the fiber-optic gauges. Figure 2.5 shows average annual strain rates for each year of the experiment (the four annual average strain rates are grouped together for each depth or depth interval). It is evident that the measured rates were not constant throughout our observation period. The departure from a constant rate of strain is due to transients related to installation, errors in measurements, and real time dependence of the ice flow; this time dependence was observed over several time scales, from hours to years. Figure 2.6 shows the residual strain for all of the active gauges, after subtracting the least-squares second-order trend from each record; the dummy gauges are plotted at the bottoms of the graphs without any trend removed. The first year of data is not plotted due to the large drift related to installation. Most of the Divide gauges recorded seasonal-time-scale strain fluctuations, which showed strong correlations among the various gauges and can be seen in Figure 2.6a. On a shorter time scale, we observed six strain events at Divide which lasted from six to twenty-four hours. Figure 2.7 shows three of these strain events as measured by

each active r-wire gauge. (The gauges are labeled by their depths, with an 'a' appended to the duplicate gauges at one depth, and a 'd' for the dummy gauges.) We saw no seasonal-time-scale fluctuations or strain events correlated among multiple gauges at Flank.

System performance

The dummy gauges served as experimental controls, allowing us to evaluate the potential stability of the gauges and dataloggers. The dummy gauges all performed beyond our expectations, with the magnitudes of the long term average strain rates all less than $1 \mu\epsilon \text{ a}^{-1}$. Furthermore, unlike the active gauges, none of the dummy gauges recorded any time-dependent fluctuations other than small amplitude short period random noise on the order of the datalogger resolution.

The surviving active gauges (10 at Divide and 12 at Flank) continued to operate for the four year duration of the experiment, with a few data gaps due to issues with memory storage. The dominant linear trend in the strain records makes it difficult to see variations in the strain rate over time (Fig. 2.3a), including the failure of many of the strain records to approach a nearly constant slope before the third year of the experiment. For each of these records, we fit a linear trend (by the method of least squares) to the last two years of the record (the portion with the most stable slope) and subtracted that trend from the entire data series. These detrended data series show the residual strain fluctuations from each gauge.

Some records settled down to a nearly constant linear trend within one to two years (Fig. 2.3b, for example), while others included a long term decaying transient which lasted through the entire experiment (Fig. 2.3c, for example) – thus the reason behind the choice of fitting a line to only the later data. A quadratic curve fit the data for gauges with long-term transients, but we did not use this fit in our quantitative analysis, due to variations in the characteristic shapes, magnitudes and time scales of the transients. We will use two terms to describe these variations in strain rate. The “initial transient,” observed during the actual freeze-in process, lasted up to one week after the installation and was described previously. The long-term drift, or simply “drift,” lasted

anywhere from one to four or more years and was characterized by a persistent change in strain rate (either increasing or decreasing) with time. In general the rate of drift decreased over the course of the experiment. The sources of this drift could have included gauge or instrument stability (apparently ruled out by the stable performance of all of the dummy gauges), installation disturbances, and/or actual variations in ice strain rates unrelated to gauge installation. The decaying nature of the drift with increasing time since installation, and the fact that the same drift was not seen in the fiber-optic data, suggests that the second possibility, installation complications, was the dominant source. As noted above, the relatively short r-wires are more susceptible to these complications than the long optical fibers.

In order to look at long-term drift for every gauge, both r-wire and fiber-optic, we calculated strain rates using subsets of the data spanning each time interval from one field visit to the next (Fig. 2.5). (These time intervals, each approximately one year, ranged from 328 to 406 days.) The differences in gauge lengths between the two gauge types preclude a direct comparison of the drift effects. The horizontal bar passing through each of the r-wire data points (Figs. 2.5a and 2.5b) represents the standard deviation of the approximately 50 one-week strain rates that were averaged together for each year, and are described in more detail in the following section. In the previous analysis of the first three years of fiber-optic gauge data (Zumberge and others, 2002), two of the length measurements taken at the end of the third year were ruled as outliers; we have not used these outliers in any strain rate calculations. The four strain rates plotted as unfilled boxes in Figures 2.5c and 2.5d were calculated over two year intervals due to the outliers.

In addition to using the dummy gauges as an experimental control, we installed two different pairs of r-wire gauges at identical depths at each site to monitor the relative accuracy of the system. Among these was one of the four gauges mentioned previously that failed, leaving us with three redundant gauge pairs. At Divide, one pair was placed at 171 m depth, in holes located 6 m apart. At Flank, pairs were placed at 167 m depth (2 m apart) and at 687 m depth (7 m apart). The long-term average strain rates on each gauge pair agreed to within 16, 5, and 7 $\mu\epsilon\text{ a}^{-1}$, respectively. The largest of these three

discrepancies, at 171 m at Divide, was due to drift of gauge 171a, as can be seen in Figure 2.5a. The strain rates measured by gauge 171 varied by less than $1 \mu\epsilon \text{ a}^{-1}$ from year three to year four, while gauge 171a drifted by $12 \mu\epsilon \text{ a}^{-1}$. Given another two to three years for this drift to decay, it appears that the two gauges would have reached near-perfect agreement. The two smaller discrepancies, between the redundant Flank gauges, were within 3% of the measured strain rates, which is comparable to the gauge-factor uncertainty. This suggests that drift was a large source of random errors in some of the calculated strain rates.

The stability of gauge 171 over the last two years of the experiment was typical of the most stable active gauges, with 11 of the 22 gauges varying by $5 \mu\epsilon \text{ a}^{-1}$ or less from year three to year four. The largest variations in annual strain rates from year three to year four were an order of magnitude greater, with six of the gauges varying by more than $10 \mu\epsilon \text{ a}^{-1}$ from year three to year four. These represent the gauges with the worst persistent drift. The RMS average of the strain rate variations over the last two years is $14 \mu\epsilon \text{ a}^{-1}$.

Long-term average strain rates

Before extracting strain rates from the raw data, we first corrected for the effects of bed-parallel shear motion on the Flank gauges. At Divide, we assumed that there was insignificant horizontal ice flow, so that the gauges responded only to the vertical strain field (Nereson and others, 1996). On the flanks of Siple Dome, there is a significant horizontal velocity away from the divide, with both the vertical and horizontal components of velocity decreasing with depth. Gauges were installed vertically (aligned with gravity), rather than bed-normal, so that at Flank the top of each gauge was angled “upstream” or against the ice flow (Harrison, 1975). Thus, the initial strain rate measured by each gauge was the sum of the vertical compression and the horizontal shear (sensed as compression) components. The effect of shearing on the gauges first rotated them away from vertical toward a position perpendicular to the ice flow, at which time they measured only the vertical compression component of the strain field. Later there was an increasing contribution of a horizontal shear (sensed as extension) component to the

strain rate as the gauges rotated such that the top of the gauge was pointed “downstream,” or with the ice flow.

We used the predicted horizontal-velocity profile in a finite-element model of ice flow to estimate the effect of shearing on each gauge over time. The results showed that the shear-strain effect should have been negligible on the shallowest gauges throughout our observation period, but below 675 m depth, it should have been significant. For example, at a depth of 861 m (our deepest operational r-wire Flank gauge) and four years after installation, our calculations indicated that the shear strain would have caused an apparently extensional strain rate of $38 \mu\epsilon \text{ a}^{-1}$ which must be subtracted from the instantaneous slope to calculate the vertical strain rate. Table 1 lists both corrected and uncorrected strain rates when the predicted shear strain effect was significant. In the figures, only corrected values are plotted.

The strain rates reported here for the r-wire gauges were calculated using only the last two years of data for each gauge. This avoided the initial transients seen in all of the active gauges and mitigated the impacts of drift on those gauges that took the longest time to settle down. As there were only four years of data collected, cropping any more than two years from the data series would have left us with an inadequate time series to analyze. For the remaining two years of each record we fit a linear trend by least squares to each week of data. (One week is enough time so that the strain accumulated on most gauges was at or above the datalogger resolution.) We took the average of these approximately 100 independently measured slopes to be the long term average strain rate and the standard deviation to represent the variability. Even when looking at only the last two years of data, deviations from the long term average strain rate included the enduring drift seen in some records, as well as variations in slope on yearly, seasonal, and shorter term time scales. The variability associated with each long term average strain rate provides a relative measure of each gauge record’s departure from a constant rate of strain as compared to the other r-wire gauges rather than an absolute uncertainty in the long term average strain rate. If we had averaged the week long strain rates over a

slightly different time, then the long term average rates would not have changed significantly, but the variabilities would have been different.

The r-wire variabilities ranged over more than an order of magnitude between gauges. The gauge with the largest variability was likely affected by time variations in firn compaction (80 m Divide gauge), although the other gauge placed near the firn-ice transition (80 m Flank gauge) had a much smaller variability. The long-term average r-wire strain rates from all depths are compiled in Table 2.1 alongside the updated results from the fiber-optic system. Both corrected results (the values in **boldface** type) and uncorrected results (in parentheses, immediately following the corrected values) from the Flank gauges with significant modeled shear strain effects are listed. Gauges that failed are listed with an “X” in the rate and variability columns. As mentioned above, the “a” and “d” labels refer to duplicates and dummy gauges, respectively.

The r-wire gauge data are presented for each of the individual gauges (approximately point measurements with depth). To facilitate comparison with the data from the optical fibers, the r-wire data are presented as interval-averaged rates over the same depth intervals as covered by the fiber-optic gauges (approximately 170 or 180 m effective gauge lengths). The interval averages were computed by fitting a smooth cubic spline curve going through all of the r-wire gauge data points (producing a continuous function of strain rate versus depth), integrating that spline function over each depth interval, and dividing by the length of the interval. We assume that the strain rate at the bed goes to zero, as there is no ice flowing into the bed. At 80 m depth the vertical strain rate is the result of a combination of firn densification and dynamic flow effects, causing an elevated strain-rate gradient with depth at 80 m compared to a point just 10 or 20 meters deeper. The splines we fit do not account for the large strain-rate gradient at 80 m, and so the shallowest interval-averaged r-wire strain rate at each site (80-to-261.5 m at Divide and 80-to-253.5 m at Flank) is biased toward a more negative value. Figure 2.4 also presents the long-term average strain rates from both gauge types.

Time-dependent strain rates and strain events

Our analysis of the data so far has focused on extracting long-term average strain rates; we also observed deviations from such a simple linear trend with time. All of the strain rates calculated for both types of gauges showed some amount of inter-annual variability in the form of oscillations and/or drift (see Fig. 2.5). Ignoring the data tainted by excessive installation-related drift, it appears that both types of gauges recorded similar levels of inter-annual variability, typically around $10 \mu\epsilon$, although several gauges did show extremely high levels of year-to-year stability on the order of $1 \mu\epsilon$. There may also have been some inter-annual variations in the form of drift not associated with gauge installation, but the dominant drift precluded analyzing this possibility.

All but two of the Divide r-wire active gauge records showed seasonal-time-scale strain fluctuations after we subtracted off the best quadratic fit to compensate for long-term drift (Fig. 2.6). Installation related drift and data gaps during the first year masked this effect entirely, and during the second year the variations do not seem well correlated among the Divide gauges. The seasonal-time-scale fluctuations were most apparent over the last two years, with the best correlation in the timing of the fluctuations among the gauges seen in year four. This effect was seen on all four of the Divide dataloggers, and was not restricted to certain datalogger channels. Neither of the dummy gauges showed any seasonal-time-scale fluctuations, even though they were attached to two dataloggers which did record seasonal-time-scale fluctuations on active gauges. None of the active or dummy gauges at Flank measured similar seasonal-time-scale correlated fluctuations in strain rate.

The strain variations over a daily time scale were some of the most interesting and surprising observations that we made. Six clearly identifiable strain events were recorded, all at Divide, and all during the third or fourth Austral summers of the experiment. The dates of the strain events were 25 December 1999, 7 January 2000, 8 January 2000, 24 January 2000, 31 January 2001, and 1 February 2001, which correspond to days 724, 737, 738, 754, 1127, and 1128. (The strain readings returned to pre-event levels between the day 737 and day 738 events, so we refer to them as two

events. The same is true of the day 1127 and day 1128 events.) The camp at Siple Dome was closed during the 2001 events. There were other weaker events, with amplitudes on the same level as the random noise.

During each of the six clear events, all of the active gauges at Divide, except one, registered a strain perturbation which lasted from six to twenty-four hours; none of the dummy gauges registered any of these events. The events registered on four separate dataloggers operating on two independent battery/solar-panel systems. Figure 2.7 shows the events as sampled on days 724, 1127, and 1128, by each of the gauges. Similar plots for each strain event were used to estimate the amplitude of that event at each depth, the amplitude being defined as the maximum strain deviation from a line connecting the data points immediately before and after the strain event. The strain signal at 717 m depth in Figure 2.7a is more complex than at the other depths. As was typical during each of the first four events (days 724 through 754), the 717 m signal lasted longer than the others, and exhibited a positive jump in strain followed by a negative jump. We measured the initial positive jump in strain to characterize the amplitude at 717 m. When the amplitudes for all six events are plotted together (Fig. 2.8), a pattern with depth reveals itself that is almost the same from 171 m down to 535 m for each event. The 444 m gauge did not register any of the strain events, and all of the amplitude curves cross from positive to negative strains at that depth. Below 535 m, the amplitude patterns are less consistent between events, but not entirely incoherent, especially when looking at only the first four events (the solid lines in Fig. 2.8). The largest variations in amplitudes appear in the firm, at 80 m. The events on days 1127 and 1128 had nearly identical amplitudes, and are plotted as one set of points in Figure 2.8.

DISCUSSION AND SUMMARY

System performance

The dummy gauge records show that the r-wire system is capable of high levels of long-term stability and that, on short time scales, the dataloggers can be insensitive to changing air temperature and other time dependent influences. Because of the influence

on the local strain field due to the installation and the gauges themselves, the potentially excellent datalogger stability does not necessarily imply that the strain rates and strain-rate variations observed by the active gauges are representative of nearby undisturbed ice.

The nature of the observed long-term drift suggests that it was related mainly to gauge-installation effects. The drift persisted for too long to be caused by temperature disturbances from the drilling, and the stability of the dummy gauges implies that it was not an instrumentation-related problem. Depth- and time-dependent disturbances to the crystal fabric of the refrozen ice, or residual stresses from the refreezing process could have been the culprits. Variations over time in the coupling between the anchors and the ice could also have contributed.

Long-term average strain rates

When interpreting the strain rates measured with the r-wire gauges, it is important to note that analyses of ice cores show inhomogeneities in ice stratigraphy over length scales comparable to our gauge length (~ one meter) and to the horizontal separation between our holes (on the order of one to 10 m). Analysis of the Greenland Ice Sheet Project 2 (GISP2) ice core revealed numerous inhomogeneous features, at the scale of grain size and larger, that could be capable of affecting ice rheology and even of disturbing the stratigraphic order (Alley and others, 1997). These features were confined to the lower 30% of the ice thickness. Visual observations of the Siple Dome deep ice core revealed similar ice-structure inhomogeneities, including reverse dips and inclined layers between 438 m and 596 m, a large number of volcanic ash and dust layers from 700 m to 730 m with a peak in fallout layer concentration from 711 m to 713 m, and inclined and distorted layers between 759 m and 780 m (Debra Meese, personal communication, 2002). We do not know how exactly these observations relate to the ice structure at our measurement sites, nor to what extent such variations may have affected our results.

The offset between the r-wire and fiber-optic results is evident in Figures 2.4b and 2.4c, with all but one of the r-wire data points falling to the left of the corresponding fiber-optic data points. This suggests that the offset is not likely due to horizontal

inhomogeneities or variations with depth of the strain field over short (one to 10 m) length scales. The r-wire and fiber-optic strain rates cannot be easily compared over the shallowest interval at each site due to the contributions of firm compaction. A one-parameter best-fit line to the eight deeper r-wire interval-averaged rates versus the fiber-optic rates showed that the r-wire data were 15% more negative than the optical-fiber data on average (12% more negative at Divide and 16% more negative at Flank). In addition to this systematic offset, the r-wire data scattered about this best fit line with an RMS deviation of $17 \mu\epsilon \text{ a}^{-1}$ ($14 \mu\epsilon \text{ a}^{-1}$ at Divide and $19 \mu\epsilon \text{ a}^{-1}$ at Flank); this scatter may be due to the differences in the length scales of the two gauge types, with the r-wires sensing vertical variations which the fiber-optic system can not resolve.

We believe that some of this disagreement was the result of uncertainty in where the upper portions of the r-wire gauges were coupled to the ice. The gauges were calibrated under the assumption that each of the two anchors (Fig. 2.1) moves at the same velocity as the adjacent ice. By this assumption, depicted by the left-hand gauge in Figure 2.9, the difference in velocities between the ice at the depth of the decoupling anchor and the ice at the depth of the lower anchor causes a measurable strain. It is assumed that the ice does not communicate any of the motion of the bridge casing to the decoupling anchor. If, as with the right-hand gauge in Figure 2.9, the ice located between the bridge casing and the decoupling anchor acts as a rigid body, then the entire upper assembly moves as one piece. In this case, the difference in velocities between the ice somewhere above the decoupling anchor and the ice at the depth of the lower anchor causes a measurable strain. Under the second scenario, there is an increase in the actual gauge length which was not accounted for in the gauge-factor measurements. The ruler scale in Figure 2.9 shows that the amount of this increase in the gauge length is between 5 and 25 cm, depending on where the upper gauge body was best coupled to the ice. This would cause a corresponding 5 to 25% systematic offset in the measured strain rates, as we observed between the two gauge types. A significantly larger distance between the decoupling anchor and the bridge casing would remedy this. Calculations using the pressure coefficient of resistance of constantan (Bridgman, 1964), show that the effect of

hydrostatic pressure on the active and return wires may have contributed to drift during the first year, but was not a factor in the systematic offset.

The 15% systematic error, probably due to gauge coupling with the ice, is relevant if one is concerned with the absolute magnitudes of the of the long-term strain rates. The $14 \mu\epsilon \text{ a}^{-1}$ RMS average of all the gauge's variations in strain rate from year three to year four is a measure of how much drift was still going on over the later half of our observations. Because some gauges were stable over years three and four and others weren't, when looking at spatial variations in the measured strain field, only differences of much more than $14 \mu\epsilon \text{ a}^{-1}$ are likely significant. Referring to Figure 2.5 can help in determining which gauges were stable and which were not. Due to the observed spatial inhomogeneities in the ice stratigraphy, the variations in strain rate with depth may represent localized ice deformation rates on length scales of approximately 1 m.

Time-dependent strain rates and strain events

The time-varying components of the strain signals (excluding those aspects deemed to be artifacts of installation or uncertainties in our measurements) are in some ways the most interesting results of these observations. While a linear trend of strain versus time fits the simple models of ice deformation, the setting for our experiment is not a simple time-independent stress field in a homogeneous medium. The ice system around the Siple Coast exhibits characteristics which vary on time scales as short as a few minutes.

Bindschadler and others (in press) observed rapid changes in horizontal and vertical positions of several GPS stations located as far as 50 km from the ice grounding line of Whillans Ice Stream (variant name: Ice Stream B). These motion events occurred near high tide and during falling tide. The authors conclude, from the relative timing of the events at multiple stations, that the motion events propagated as shear waves through the till, and as elastic waves through the ice shelf.

Short time scale motion can be isolated to layers within an ice sheet. Tilt sensors frozen into the ice sheet adjacent to Jakobshavn Isbræ exhibited oscillating angle variations up to 0.3° over 20 minute intervals (Lüthi, Funk, and Iken, submitted *J.*

Geophys. Res., 2003). Ice velocities at this study site are much smaller than those in Jakobshavn Isbræ, much like the situation at Siple Dome. The magnitude of the oscillations dies off quickly with distance above and below the affected layer.

Other aspects of ice flow vary on time scales of many hours to days. When the earlier r-wire strain gauges were deployed in the trunk of Whillans Ice Stream (Harrison and others, 1993) all of the strain records showed deviations from the linear trend over time scales of hours to days with amplitudes of a few to tens of $\mu\epsilon$. At each of two different study sites, two adjacent gauges at the same depth and in holes 0.8 m or 3 m apart measured simultaneous strain events several times throughout their records. Some of the active gauges showed intermittent diurnal behavior during the Austral summer. As with the current experiment, the dummy gauges did not register any of these short-term strain events.

The seismicity measured on Whillans Ice Stream and Kamb Ice Stream seems to be modulated by the tide beneath the Ross Ice Shelf (Anandakrishnan and Alley, 1997). Harrison and others (1993) also observed diurnal variations in seismicity on Whillans Ice Stream. Engelhardt and Kamb (1997) and Kamb (2001) observed a “seemingly random appearance and disappearance” of diurnal fluctuations in basal water pressure recorded beneath Whillans Ice Stream and Kamb Ice Stream.

On longer time scales, seasonal fluctuations have been observed. Harrison and others (1993) noted that seismicity in Whillans Ice Stream was far more active during Austral Winter than during Summer. Zwally and others (2002) reported seasonal fluctuations in the surface velocity of the Greenland ice sheet at the equilibrium line, attributed to variations in water flow to the bed.

Variations in the ice sheet also occur over many years, and Alley and Whillans (1991) summarized many of the changes observed in the West Antarctica ice sheet. Bindschadler and Vornberger (1998) used satellite imagery from the 1960's and 1990's to show that ice-stream margins migrate and ice-stream velocities can change by a factor of two in just a few decades. Harrison and others (1998) used ice temperature observations and Echelmeyer and Harrison (1999) used ice velocities derived with GPS

to measure the margin migration on Whillans Ice Stream. Both sets of observations indicated that the southern ice margin was migrating outward on the order of 10 m a^{-1} . All of these observations show that on many time scales, the West Antarctic ice sheet is a highly dynamic entity.

Strain events have also been observed in valley glaciers. On Black Rapids Glacier, Raymond and others (1995b) noted correlations between strain events measured between 7 m and 15 m below the surface and changes in the glacier drainage system. Kavanaugh and Clarke (2001) observed a strain event on Trapridge Glacier in conjunction with seismic activity and basal motion. The strain event showed an increase in the vertical strain signal of several hundred micro-strain which persisted for eight hours before suddenly dropping off to a strain level below the initial reading. This strain event was one or two orders of magnitude greater than what we observed at Siple Dome.

Analogous slow (relative to earthquakes) strain events have also been observed in the earth's crust along tectonic faults (e.g., Gladwin and others, 1994 and Linde and others, 1996). Borehole strain meters adjacent to faults typically show long-term creep, with some records punctuated by irregularly spaced strain events.

At yearly time scales, the variations we observed in measured strain rates from one year to the next may be real. Both types of gauges recorded similar levels of year to year variations, but these variations were near the levels of uncertainty of both gauges. Over shorter time scales, only the r-wires were able to track variations in strain rate.

There are several aspects of the seasonal-time-scale strain fluctuations and the short-term strain events which are similar. Some of the facts suggest that both of these phenomenon were real, and unrelated to instrumental errors, installation transients, or anthropogenic sources. (Figure 2.6 is relevant to the following discussion.) The dummy gauges have already been discussed as evidence that in a best case scenario the r-wire system is capable of long- and short-term stability. If the strain fluctuations were related to surface temperatures, then the effect was somehow confined to individual datalogger channels, and the affected channels were different on each datalogger. Furthermore, the datalogger sensitivity to temperature was not seen at Flank, where the experimental setup

was nearly identical to that at Divide. Strain fluctuations coincident in time among several gauges were seen on nine out of 22 active gauges, and all nine affected gauges were located at Divide.

A simple calculation of the diffusion of seasonal temperature fluctuations into the ice sheet (Paterson, 1994, pp. 206-207) shows that even the shallowest r-wire gauges do not see significant temperature variations with time. To investigate whether the instrument cables could have carried the seasonal temperature variations to the gauges, we substituted the thermal diffusivity of pure copper for that of ice in the same diffusion formulas (thereby computing the grossly exaggerated case of temperature diffusion into a copper half-space) and found the depth scale was ten times that for ice. This is still inadequate to affect the deeper gauges. Because we saw strain events and seasonal-time-scale variations on both deep and shallow gauges at Divide, even temperature conduction down the instrument cables can not be the cause.

Radio or electrical interference from the Siple Dome camp or drilling operations are ruled out by the fact that the camp was closed by the time of the last two strain events, and the seasonal-time-scale fluctuations persist year-round. There are no obvious changes in the battery voltages coincident with either type of strain fluctuation. Other evidence does not support the premise that both types of observed strain fluctuations were real.

The sudden jumps in strain during our field visits (the vertical gray bars in Fig. 2.6 denote each field visit) seen at both Divide and Flank show that the dataloggers are indeed susceptible to external influences, but the dummy gauge records show that not every datalogger channel was affected. The jumps did not occur when we first dug out the dataloggers or opened up their protective boxes, but rather several days later when we tightened the screws holding the instrument cable wire leads and switched the power supplies back to the external batteries. This shows that the sudden jumps were not related to temperature changes.

The appearance of the two types of strain fluctuations during only the third and fourth years is inconsistent with ongoing processes in the ice sheet. We believe that the

excessive drift during the first year prevented us from seeing other variations in the strain signal. Perhaps this was true during the second year as well.

The Divide gauge at 444 m did not show evidence of either seasonal-time-scale strain fluctuations or short-term strain events. This draws an apparent link between the two types of strain fluctuations being discussed. One possibility is that this gauge was attached to one of only three properly working datalogger channels at Divide (with the dummy gauges attached to the other two). Another explanation is that the ice at 444 m was not affected in the same way as other depths, perhaps because of the proximity to the beginning of a layer reverse dips and inclined layers at 438 m. The transition from positive to negative strain event amplitudes at 444 m (Figure 8) provides a possible physical explanation for the null amplitude at that depth.

The short-term strain events had no apparent correlation with datalogger temperature or any of the climatic variables recorded at Siple Dome and archived by the Antarctic Automatic Weather Stations Project at the University of Wisconsin – Madison (<http://uwamrc.ssec.wisc.edu/aws/>): air temperature, barometric pressure, wind direction and velocity, or relative humidity. Anandakrishnan and Winberry (personal communication, 2002) were measuring the seismic activity at Siple Dome at the same time as our events occurred as part of the Antarctic Network of Unattended Broadband Seismometers (ANUBIS) Project. While their analysis does not focus on seismicity in the ice sheet, they do see approximately three low amplitude seismic events per day at Siple Dome which do not register at any other stations and may be icequakes or low energy tectonic quakes.

The timing of the strain events was coincident on all of the gauges to within 90 minutes. A hypothesis proposed to explain the strain events, or any of the observed time dependencies in strain rates, can not be dependant on liquid water in the ice or at the bed, as the basal ice temperature at Divide is -2.54°C (Hermann Englehardt, personal communication, 2002). Instead, we look for evidence of disturbances in the ice.

The signals seen at 717 m depth during the first four strain events were more complex and lasted longer than the concurrent signals seen at other depths. Figure 8

shows that the total range of event amplitudes seen at 717 m was greater than at any other depth except 80 m (where the softer firn could be expected to respond differently than ice). These characteristics suggest that the first four strain events were related to activity in the ice near the 717 m gauge. The large number of ash layers observed in the core from 711 to 713 m could be related to such activity, although it is impossible to say whether the presence of ash increases, decreases or has an insignificant effect on the strength of the ice (Paterson, 1994, pp. 88-89).

Something changed between the events occurring in 1999/2000 and those occurring in 2001. During the two events in 2001, the event amplitude at 717 m changed signs and the signal was not anomalous relative to other depths. This suggests that the events in 2001 were related to a disturbance at a different depth.

While we do not know of any ice flow mechanisms or possible changes in the stresses in the ice which are consistent with the seasonal-time-scale variations and we do not have a clear picture of what caused the strain events, simple instrument related sources can not explain these observations.

One final point to highlight is that both types of strain fluctuations just discussed typically amounted to five or 10 $\mu\epsilon$ deviations from the long-term average trends in strain. This is at least an order of magnitude smaller than the strain accumulated over one year as observed by all of the active r-wire gauges except those at Divide at 798 m and 899 m.

CALCULATING AN AGE-DEPTH RELATIONSHIP AT DIVIDE

Our results provide the basis for calculating an age-depth relationship for the ice at Divide independent of a theoretical ice flow model. Because horizontal velocities are negligible beneath the flow divide, our gauges measured flow parallel to the flow pattern of the ice. To be consistent with the rest of this paper, depths are given as actual distances below the surface, where $z = 0$. We make two of the same assumptions about the ice sheet as found in Nereson and others (1996): (1) the velocity field at Divide is purely vertical, and (2) the ice sheet and flow geometries are time-independent.

Zumberge and others (2002) show that the ice sheet thickness was close to steady state

over the duration of our measurements. We will compute two age-depth relationships, one each using the r-wire and the optical-fiber data. For the r-wire strain rates, we begin with the same spline fit as we used in the calculation of depth-interval average strain rates. Integrating this spline over the ice sheet thickness,

$$w(z) = \int_{z_{bed}}^z \dot{\epsilon}(z') dz', \quad (1)$$

yields the vertical velocity distribution with depth, $w(z)$. z_{bed} is the measured thickness of 1004 m and the velocity at that depth is zero because there is no basal melting. We integrated up from the bed because we do not have r-wire measurements in the firn layer.

The fiber-optic EDM measurements are in the form of lengths as a function of time. Fitting slopes to these data yields velocities at the depths of the deep anchors relative to the upper fiber termination points, located at the surface at the beginning of the experiment. Fitting a cubic spline to the velocities yields a continuous $w(z)$ function, akin to that which we computed from the r-wire strain rates.

Following the method of Nereson and others (1996) we compute the age of the ice as a function of depth,

$$A(z) = \int_0^z \frac{1}{w(z')} dz', \quad (2)$$

where $A(z)$ is the age-depth relationship with $A(z = 0) = 0$. The results are plotted in Figure 2.10 along with the ages computed in Nereson and others (1996) from a finite element modeled ice velocity field.

The optical-fiber measurements are better suited for these calculations because the measurements are in the form of displacements over time. The r-wire strain measurements require the additional integration in Equation (1). We used the uncertainties associated with the fiber-optic to compute error limits on the corresponding age-depth curve. These uncertainties do not reflect the errors due to using a spline fit to interpolate between the source data of r-wire strain rates or optical-fiber velocities. The depths of the source data points are also plotted to indicate the depth intervals over which interpolation was necessary.

The results in Figure 2.10 show that the curves below 700 m are dominated by uncertainties of the same magnitude as the computed ages. In addition to this uncertainty, the assumptions of steady-state conditions are likely not valid throughout the entire history of the dome and this means that our results are most realistic at shallower depths. All three curves fall within the fiber-optic error limits from 700 m on down. The lowest estimate of the age of the ice at 900 m is 100 ka; the diverging error limits bring into question any calculations for ice deeper than that. The ice at the bed is at least 120,000 years old, meaning that the ice at Siple Dome includes a complete record of the Wisconsin glacial episode.

CONCLUSIONS

At Siple Dome, West Antarctica, we measured vertical strain rates at several depths at two locations. We were able to measure long-term average strain rates using two types of gauges. The strain rates measured by the r-wire gauges were 15% more negative on average than the fiber-optic rates. This difference cannot be fully explained by drift in the r-wire measurements or by our initial estimates of the systematic errors in gauge calibration; we believe it was due to inadequate decoupling of the motion of the upper gauge components from the decoupling anchor. The short gauge length and continuous logging of the r-wire gauges allow us to discern variations in strain rates over short length and time scales.

At both sites, the r-wire gauges at 80 m depth recorded elevated strain rates due to firn compaction, consistent with measurements by other researchers of strain rates throughout the firn and densities of shallow firn and ice cores. Below 80 m, the pattern of strain rate versus depth as measured by both gauge types was different at the two sites. We found less compressive strain rates and a more linear pattern of strain rate versus depth at Divide than at Flank, as was discussed previously by Zumberge and others (2002).

Our observations of time-dependent strain rate variations appear over four time-scales: multi-year drift, year-to-year variability about the long-term average, seasonal-time-scale fluctuations, and strain events lasting less than a day. The multi-year drift,

which was far more prevalent among the r-wire gauges, was almost certainly related to installation. The year-to-year variability was at a level comparable to our uncertainties in the strain rates, so we can not conclude whether or not it was real. In the cases of the seasonal-time-scale fluctuations and the strain events, the lack of corresponding variations in both the dummy gauges and the Flank gauges suggest that these were not due to instrumental effects. However, we are not able to propose any mechanisms to explain how seasonal-time-scale fluctuations could reach our gauges, which are more than 50 ice thicknesses away from any ice streams or the Ross Ice Shelf, nor why these fluctuations did not appear at the Flank. We hypothesize that the strain events occurred as a result of deformation in the ice, with evidence suggesting it was related to the observed peak concentration of ash and dust layers in the deep ice core at 711-713 m.

We computed two age-depth relationships for the ice at Divide, using data from both gauge types. The uncertainties in the deepest 100 m of the ice sheet are as large or larger than the calculated ages. Under the assumptions that the ice sheet and flow geometries are time independent, the ice at 900 m is at least 120,000 years old. The deep ice core drilled at Siple Dome reaches the bed, which is more than 100 m deeper than that. This suggests that the Siple Dome deep ice core includes a complete record of the Wisconsin ice age and that the oldest part of the core is at least as old as the Sangamon interglacial of 115 to 125 ka BP.

It is clear that the Siple Coast ice streams and their surroundings make up a highly complex and dynamic system. Time and again new findings show that the driving forces in the region (geothermal, tidal, gravitational, etc.) have far-reaching effects which are complicated by the response dynamics of the ice sheet and its environment. Our measurements provide yet another look into this system.

ACKNOWLEDGEMENTS

We are grateful to Hermann Englehardt and the Caltech hot-water drilling team who worked round-the-clock to provide us with open holes for our gauges, to Chad Trabant who worked extensively on prototype r-wire gauge testing and design

improvements, and to the Geophysical Institute machine shop crew and Bill Zito who manufactured the r-wire gauges. This project was funded by NSF-OPP grants 9220199, 9615502, 9515454 and 9615417.

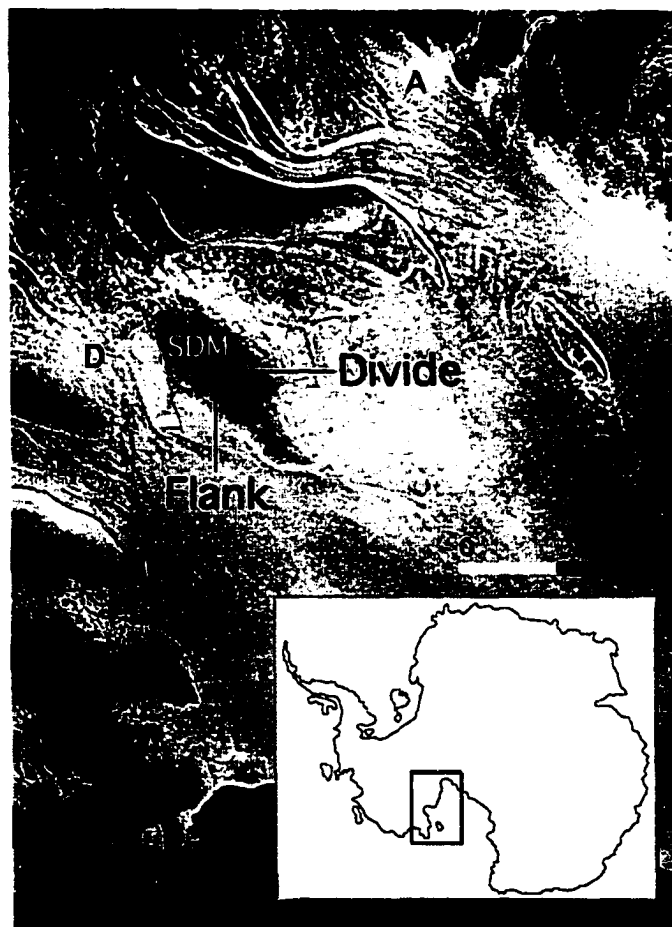


Figure 2.1: Location map. Location map of the study area, and the surrounding Siple Coast. The six Siple Coast ice streams are labeled (by their lettered variant names), as is Siple Dome (SDM). Base image mosaic from the RAMP AMM-1 SAR Image Mosaic of Antarctica (Jezek and others, 2002).

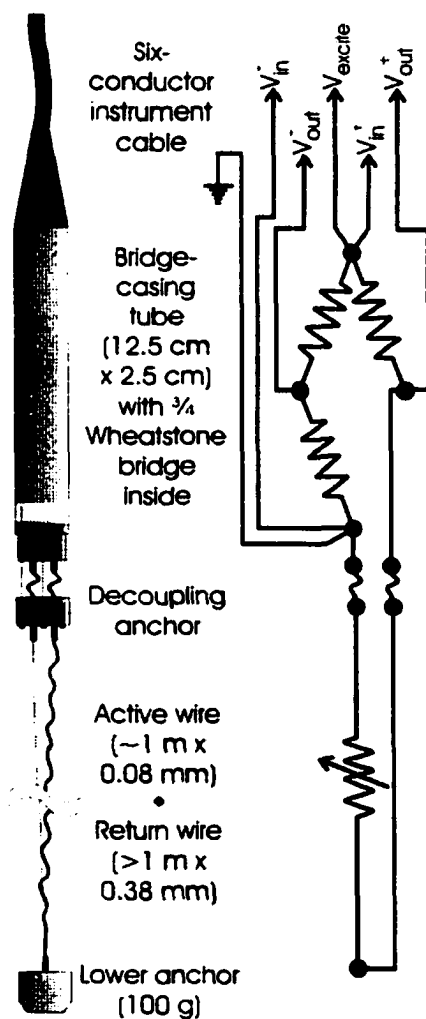


Figure 2.2: Gauge Design. Diagram showing the physical and schematic design of the resistance-wire gauges deployed at Siple Dome. The dummy gauge design (not pictured) incorporates the active wire into the bridge casing, and thus eliminates the decoupling and lower anchors and the return wire.

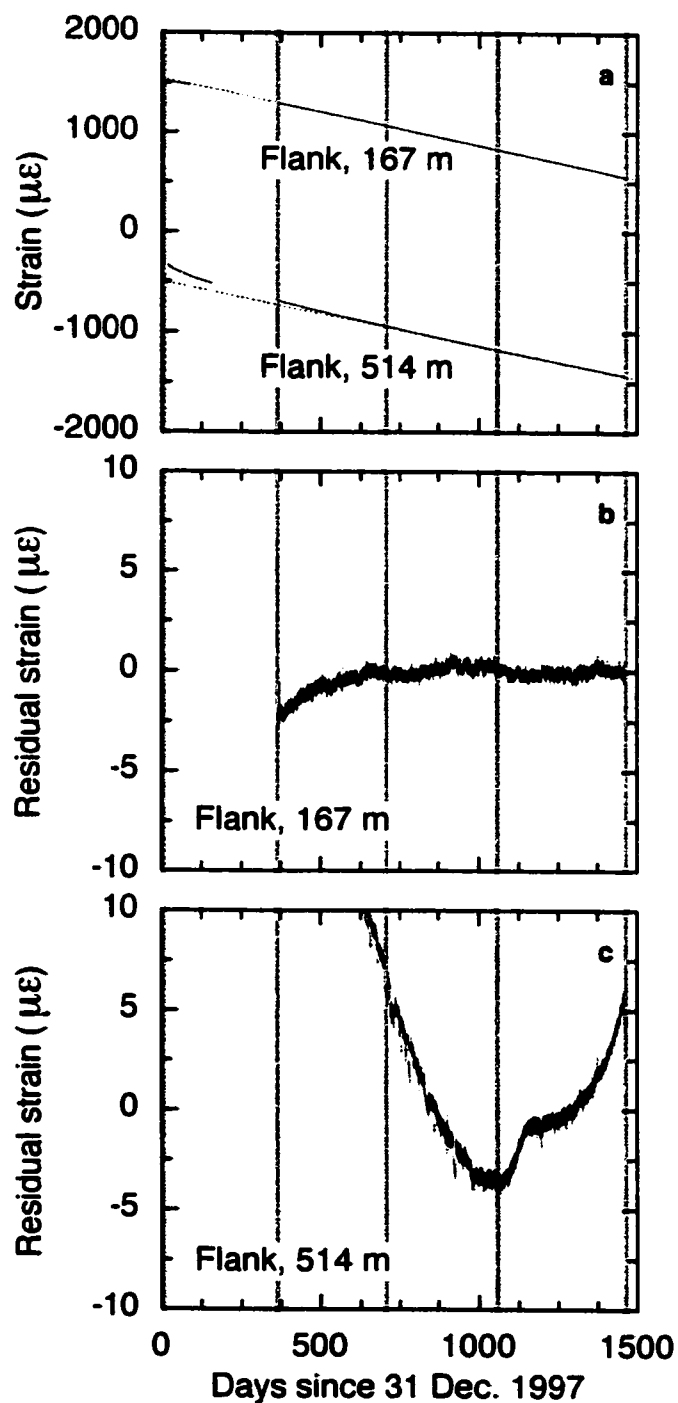


Figure 2.3: Sample gauges. (a) Examples of resistance-wire gauge records of strain. Also shown (b and c) are the same records after a linear trend has been removed.

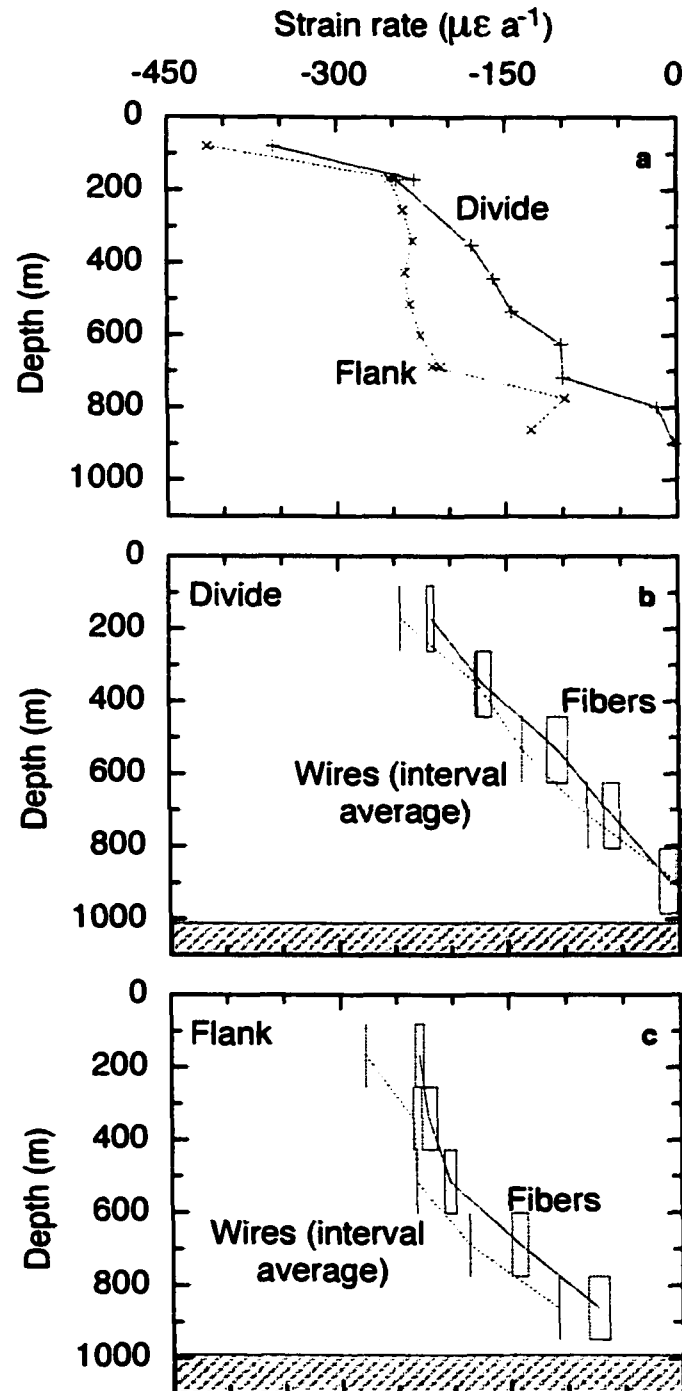


Figure 2.4: Long-term average strain rates. (a) Long-term average strain rate as a function of depth as measured by the resistance-wire gauges. Resistance-wire measured strain rates are also given as interval averages along with the fiber-optic rates at (b) Divide and (c) Flank.

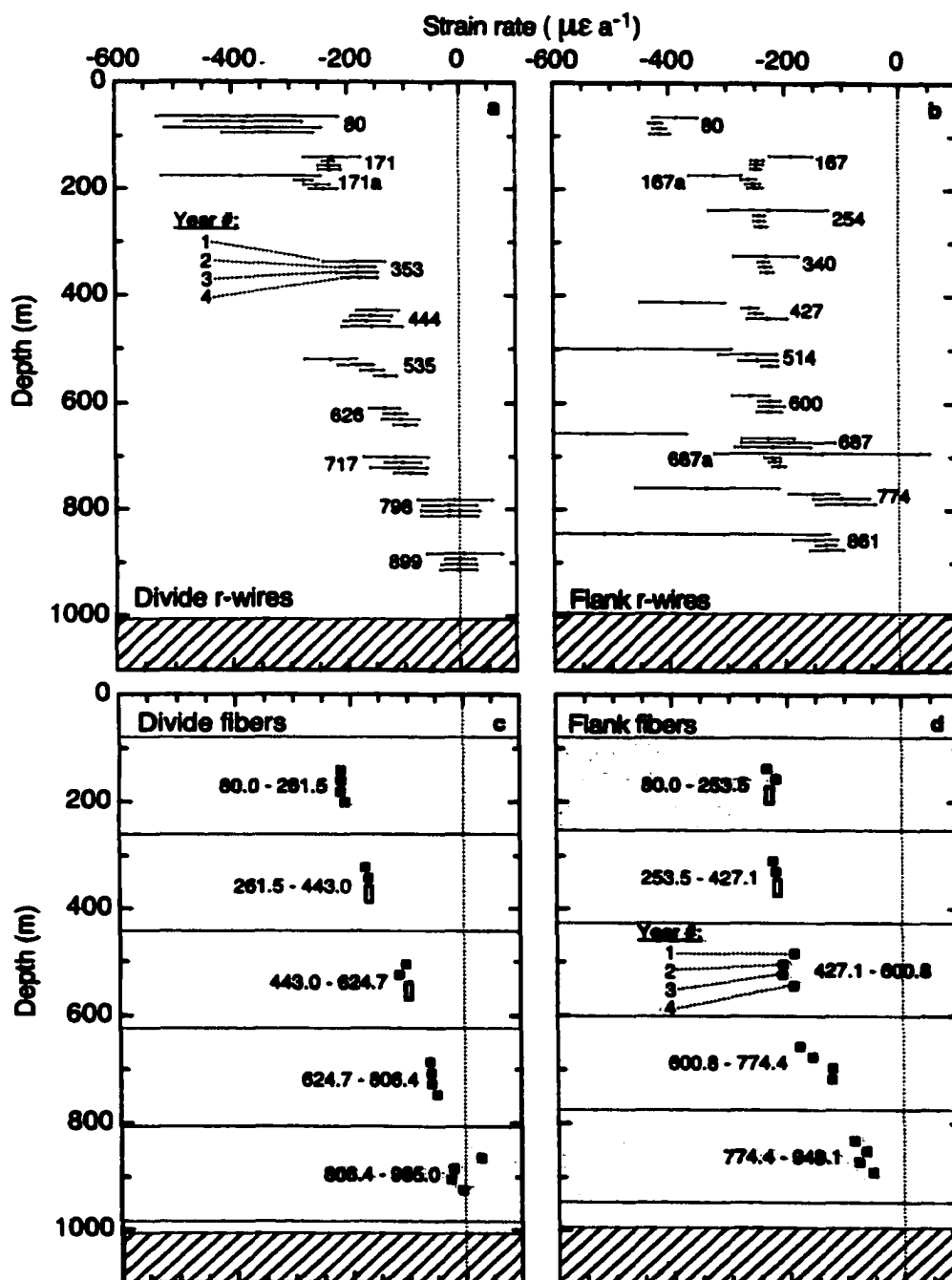


Figure 2.5: Annual strain rates. The resistance-wire rates at (a) Divide and (b) Flank, grouped together by depth, with each four years of data plotted as labeled for the 353 m Divide gauge. The horizontal bars passing through the data points represent the standard deviations of one-week strain rates averaged together for each year. The fiber-optic data are presented for (c) Divide and (d) Flank. The four open boxes represent two-year average strain rates, due to outliers in the data.

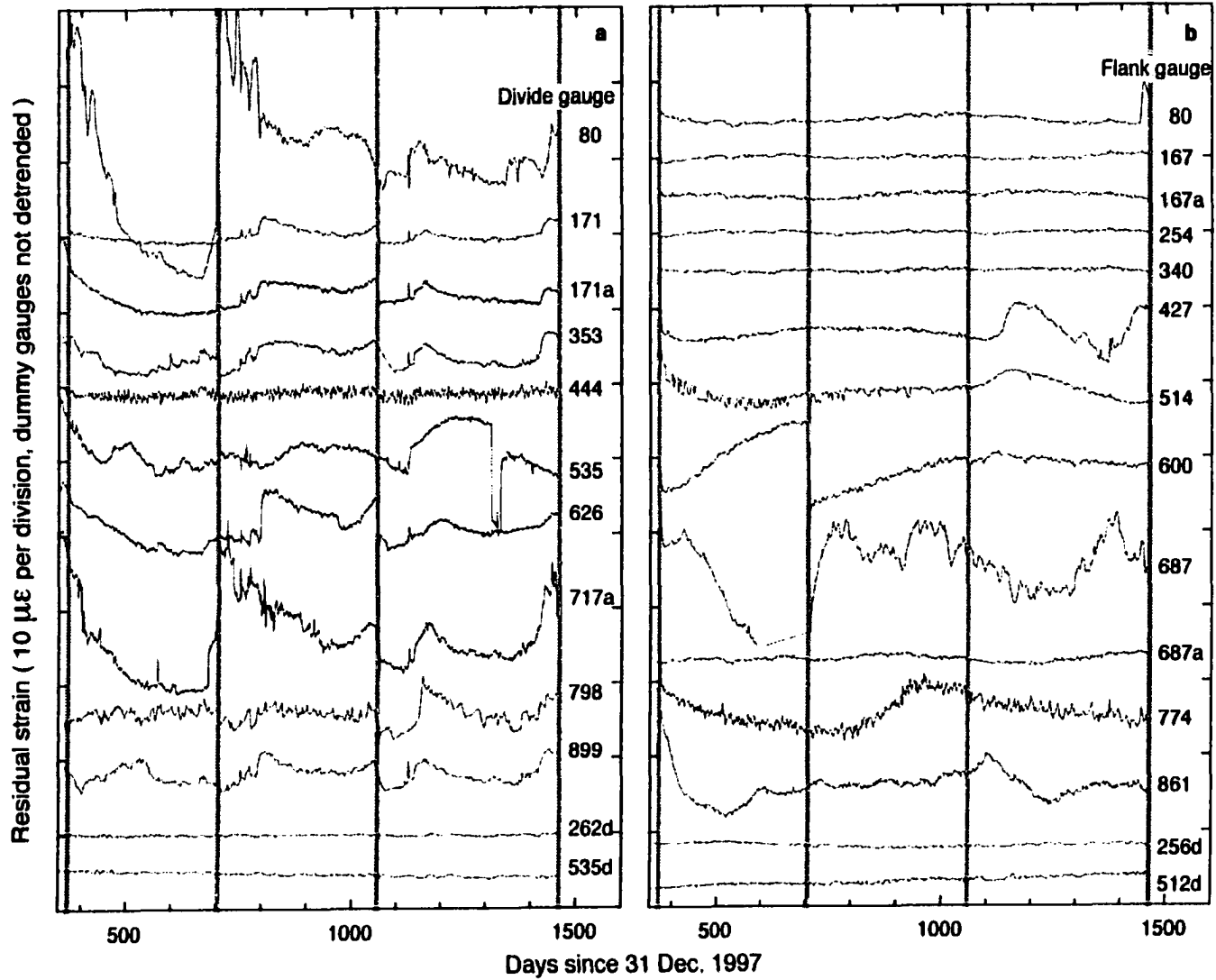


Figure 2.6: Detrended strains. R-wire gauge records during years two, three, and four at (a) Divide and (b) Flank after detrending by subtraction of the least-squares quadratic fits; the dummy gauge records have not been detrended.

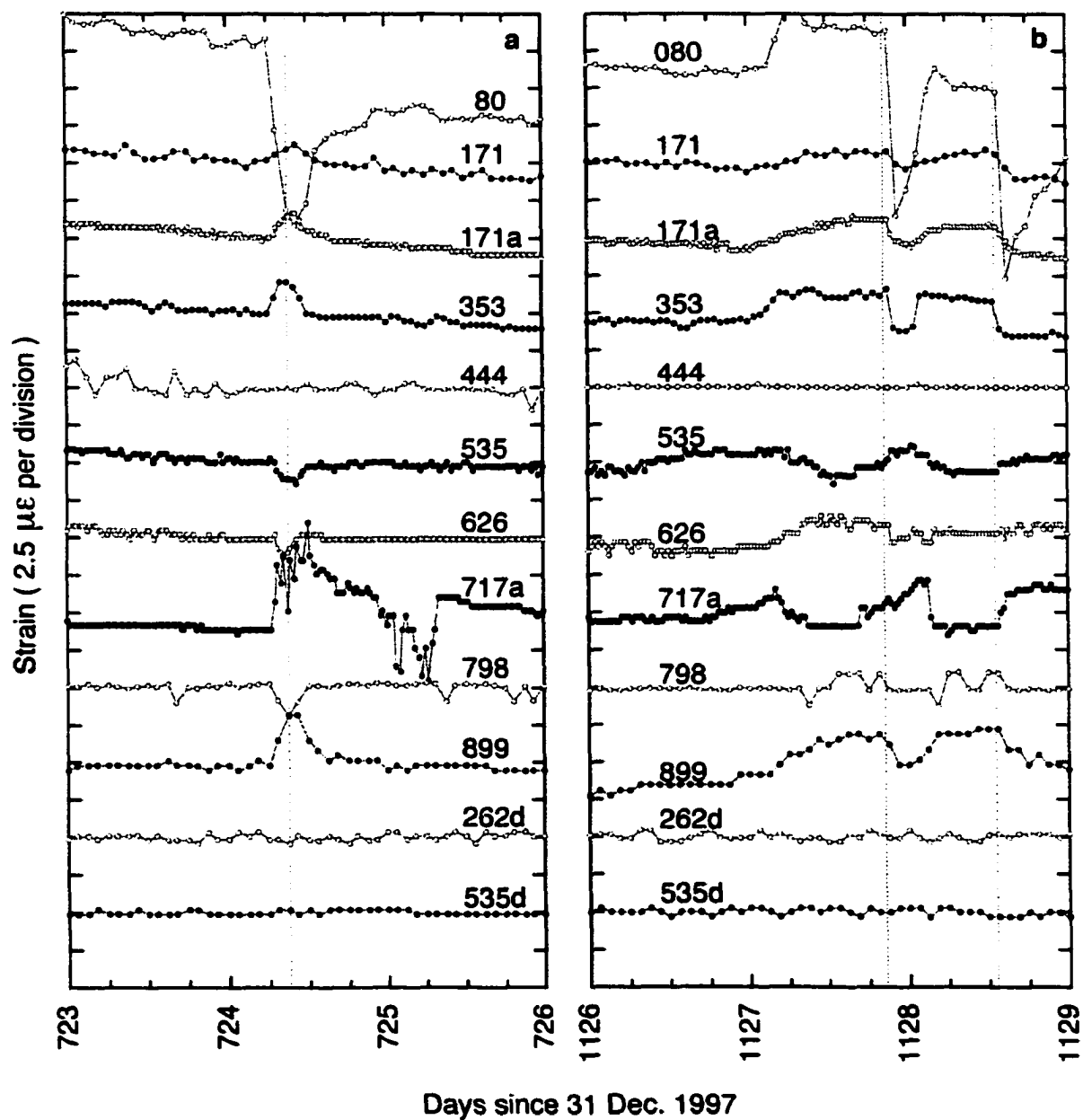


Figure 2.7: Sample strain events. One of these events occurred on (a) day 724 (25 December 1999) and two on (b) days 1127 and 1128 (31 January and 1 February, 2001).

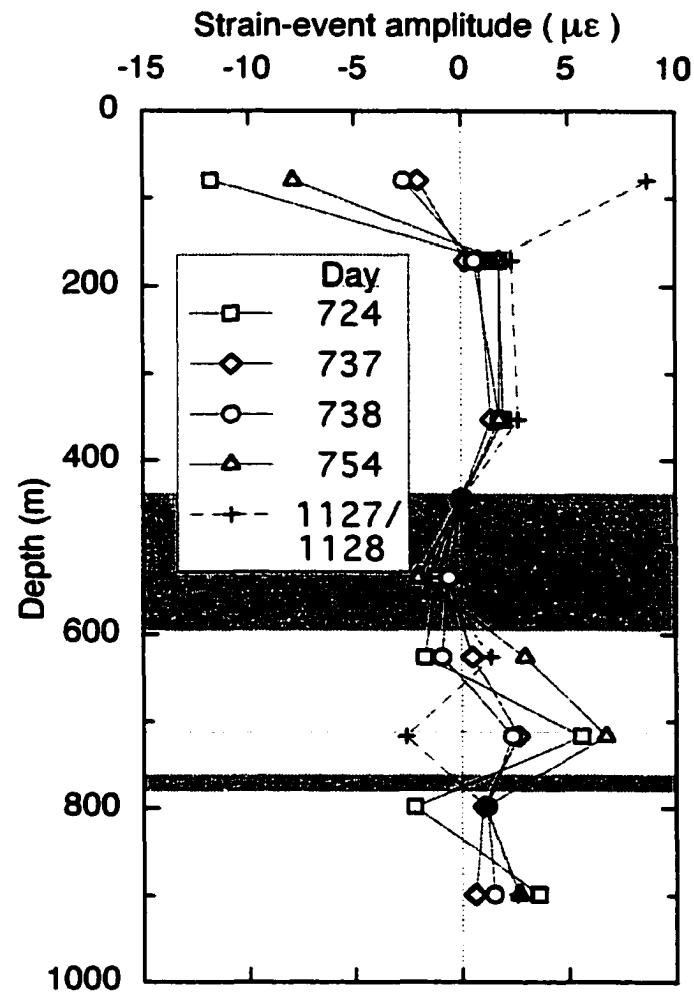


Figure 2.8: Strain-event amplitudes. Strain-event amplitudes as a function of depth. The events in 1999 and 2000 are plotted with solid lines. The two events in 2001 (days 1127 and 1128) are plotted as one set of points because the amplitudes were nearly identical; a dashed line connects these points because they differed from the earlier events, as described in the text.

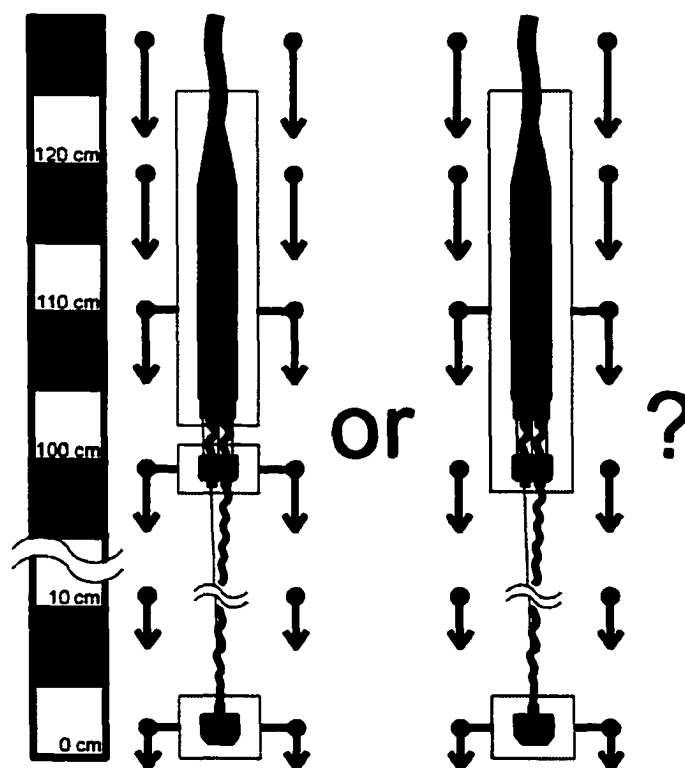


Figure 2.9: Gauge-to-ice coupling. A graphic showing the uncertainty in how the upper r-wire gauge assembly is coupled to the ice. The decoupling anchor on the left-hand gauge is not influenced by the downward motion of the bridge casing. The decoupling anchor on the right-hand gauge moves as a single body with the bridge casing due to rigid ice between them; this 5 to 25 cm increase in the actual gauge length results in a 5 to 25% systematic offset in the measured strain rates.

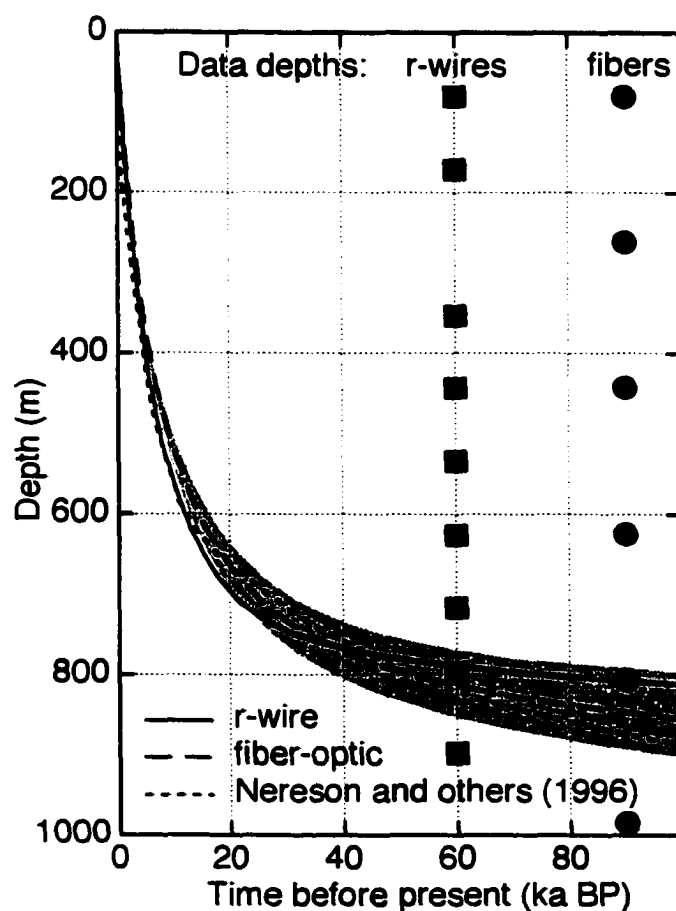


Figure 2.10: Age-depth relationship. *The age-depth relationship of the ice at Divide. The three curves were computed using resistance-wire (r-wire) measured strain rates, fiber-optic measured displacements, and finite element modeled (Nereson and others, 1996) velocities. The gray band surrounding the fiber-optic derived ages shows the error limits due to uncertainties in the measured displacements. The depths of the resistance wire gauges and the fiber-optic lower anchors are also plotted to show where interpolated data was used in our calculations.*

Table 2.1: Long term average strain rates. Long term average strain rates as measured by the r-wire (averaged over years three and four) and fiber-optic gauges (averaged over all four years). The r-wire rates are reported for each gauge, and as average rates over the same depth intervals as the optical fibers. X's indicate nonfunctioning gauges. The corrected rates are boldfaced, with the uncorrected values following in parentheses.

	Wires			Optical fibers			
	Depth (m)	Strain rate ($\mu\epsilon \text{ a}^{-1}$)	Variability ($\mu\epsilon \text{ a}^{-1}$)	Depth interval (m)	Strain rate ($\mu\epsilon \text{ a}^{-1}$)	Strain rate ($\mu\epsilon \text{ a}^{-1}$)	Uncertainty ($\mu\epsilon \text{ a}^{-1}$)
Divide	80	-356	111	80.0 - 261.5	-245	-217	3
	171	-230	20				
	171a	-246	25				
	262	X	X	261.5 - 443.0	-176	-171	7
	353	-179	34				
	444	-160	48				
	535	-144	24	443.0 - 624.7	-137	-106	9
	626	-101	27				
	717	X	X				
	717a	-99	41	624.7 - 806.4	-80	-59	7
	798	-18	52				
	899	-3	32				
	944	X	X	806.4 - 985.0	-3	-9	9
80	-414	16					
167	-247	10					
167a	-252	13	80.0 - 253.5	-278	-230	4	
254	-241	10					
340	-232	11					
Flank	427	-239	28	253.5 - 427.1	-236	-221	7
	514	-235	27				
	600	-225	21				
	687	-207 (-209)	75	600.8 - 774.4	-186	-142	7
	687a	-214 (-216)	12				
	774	-98 (-96)	51				
	861	-128 (-101)	25	774.4 - 948.1	-108	-73 (-64)	9
	905	X	X				

REFERENCES

- Alley, R.B. and I.M. Whillans. 1991. Changes in the West Antarctic ice sheet. *Science*, **254**(5034), 959-963.
- Alley, R.B., A.J. Gow, D.A. Meese, J.J. Fitzpatrick, E.D. Waddington, and J.F. Bolzan. 1997. Grain-scale processes, folding, and stratigraphic disturbance in the GISP2 ice core. *J. Geophys. Res.*, **102**(C12), 26819-26830.
- Anandakrishnan, S. and R.B. Alley. 1997. Tidal forcing of basal seismicity of ice stream C, West Antarctica, observed far inland, *J. Geophys. Res.* **102**(B7), 15183-15196.
- Bindschadler, R.A. ed. 1995. *West Antarctic Ice Sheet Initiative: Science and Implementation Plan*. WAIS Working Group. National Science Foundation.
- Bindschadler, R.A., and P.L. Vornberger. 1998. Changes in West Antarctic ice sheet since 1963 from Declassified Satellite Photography, *Science*, **279**, 689-692.
- Bindschadler, R., P. Vornberger, M. King, and L. Padman. In press. Tidally-driven stick-slip motion in the mouth of Whillans Ice Stream, Antarctica. *Annals of Glaciology*, **36**.
- Bridgman, P.W. 1964. *Collected Experimental Papers of P.W. Bridgman*. Harvard Univ. Press. Vol. II, 365-370.
- Echelmeyer, K.A., and W.D. Harrison. 1999. Ongoing margin migration of Ice Stream B, Antarctica, *J. Glaciol.* **45**(150), 361-369.
- Engelhardt, H., and B. Kamb. 1997. Basal hydraulic system of a West Antarctic ice stream: constraints from borehole observations, *J. Glaciol.* **43** (144), 207-230.

Gladwin, M.T., R.L. Gwyther, R.H.G. Hart, K.S. Breckenridge. 1994. Measurements of the strain field associated with episodic creep events on the San Andreas fault at San Juan Bautista, California. *J. Geophys. Res.*, **99**(B3), 4559-4565.

Gow, A.J., and H. Engelhardt. 2000. Preliminary analysis of ice cores from Siple Dome, West Antarctica, in *Physics of Ice Core Records*, T. Hondoh, ed. Hokkaido University Press, Sapporo, Japan. 63-82.

Harrison, W.D. 1975. A measurement of surface-perpendicular strain-rate in a glacier. *J. Glaciol.*, **14**(70), 31-37.

Harrison, W.D., K.A. Echelmeyer, and H. Englehardt. 1993. Short-period observations of speed, strain and seismicity on Ice Stream B, Antarctica. *J. Glaciol.*, **39**(133), 463-470.

Harrison, W.D., K.A. Echelmeyer, and C.F. Larsen. 1998. Measurement of temperature in a margin of Ice Stream B, Antarctica: implications for margin migration and lateral drag. *J. Glaciol.*, **44**(148), 615-624.

Hughes, T. 1973. Is the West Antarctic Ice Sheet disintegrating?, *J. Geophys. Res.* **78**(33), 7884-7910.

Jezeq, K., and RAMP Product Team. 2002. RAMP AMM-1 SAR Image Mosaic of Antarctica. Fairbanks, AK: Alaska SAR Facility, in association with the National Snow and Ice Data Center, Boulder, CO. Digital media.

Kamb, B. 2001. The lubricating basal zone of the West Antarctic Ice Streams, in *The West Antarctic Ice Sheet, Behavior and Environment*, R.B. Alley and R.A. Bindshadler, ed., American Geophysical Union, Washington, D.C., **77**, Antarctic research series. 157-199.

Kavanaugh, J.L., and G.K.C. Clarke. 2001. Abrupt glacier motion and reorganization of basal shear stress following the establishment of a connected drainage system. *J. Glaciol.*, **47**(158), 472-480.

Linde, A. T., M. T. Gladwin, M. J. S. Johnston, R. L. Gwyther, and R. G. Bilham. 1996. A slow earthquake sequence on the San Andreas fault, *Nature*, **383**, 65-68, 1996.

Nereson, N.A., E.D. Waddington, C.F. Raymond, and H.P. Jacobson. 1996. Predicted age-depth scales for Siple Dome and inland WAIS ice cores in west Antarctica. *Geophys. Res. Lett.*, **23**(22), 3163-3166.

Nereson, N.A., C.F. Raymond, E.D. Waddington, and R.W. Jacobel. 1998. Recent migration of Siple Dome ice divide, West Antarctica. *J. Glaciol.*, **44**(148), 643-652.

Paterson, W.S.B. 1994. *The physics of glaciers. Third edition.* Oxford, etc., Elsevier.

Raymond, C.F., N.A. Nereson, A.M. Gades, and H. Conway. 1995a. Geometry and stratigraphy of Siple Dome, Antarctica. *Antarctic Journal of the United States, Review*, National Science Foundation, **30**(5). 91-93.

Raymond, C.F., R.J. Benedict, W.D. Harrison, K.A. Echelmeyer, and M. Sturm. 1995b. Hydrological discharges and motion of Fels and Black Rapids Glaciers, Alaska, U.S.A.: implications for the structure of their drainage systems. *J. Glaciol.*, **41**(138), 290-304.

Rose, K.E. 1979. Characteristics of ice flow in Marie Byrd Land, Antarctica. *J. Glaciol.*, **24**(90), 63-75.

Zumberge, J.H., B.M.E. Smith, and A. Fuzesy. 1969. *Ross Ice Shelf Studies*, 1969.

Antarctic Journal of the United States, National Science Foundation, 4(5). 215-216.

Zumberge, M.A., D.H. Elsberg, W.D. Harrison, E. Husmann, J.L. Morack, E.C. Pettit, and E.D. Waddington. 2002. Measurement of vertical strain and velocity at Siple Dome, Antarctica, with Optical Sensors. *J. Glaciol.*, 48(161). 217-225.

Zwally, H.J., W. Abdalati, T. Herring, K. Larson, J. Saba, and K. Steffen. 2002. Surface Melt-Induced Acceleration of Greenland Ice-Sheet Flow. *Science*, 297(5579). 218-222.

Chapter 3. Mapping the regional distribution of equilibrium lines: a case study in the western Chugach Mountains, Alaska*

Daniel H. Elsberg¹, William D. Harrison¹, Keith Echelmeyer¹, Tyler J. Fudge²

¹*Geophysical Institute, University of Alaska–Fairbanks, Fairbanks, Alaska 99775-7320, U.S.A.*

²*Geology Department, Bowdoin College, Brunswick, Maine 04011, U.S.A.*

Abstract. We have completed a case study in the western Chugach Mountains, Alaska, of measuring the regional pattern of equilibrium lines and temporal changes in the pattern using aerial photographs and digital video, and Landsat scenes covering many years from 1950 to 2001. Our goals were to evaluate the accuracy of such measurements, and to assess the spatial and temporal variability of the resulting data. We used laser altimetry from 1994 through 2001 and maps from 1950 to estimate surface elevations over the entire time period of observations, and a modeled snow line rise curve to account for ablation between the image dates and the end of the summer. Our uncertainties in those two corrections accounted for our stated random error of 30 m. The average glacier thinning from 1950 to 2000/2001, at the equilibrium lines, was 40 m. The average correction for snow line rise after the dates of image acquisitions was 28 m. Individual glacier equilibrium line altitudes varied by 100 m relative to a smoothed surface over a 20 km spatial scale, and inter-annual variations in equilibrium line altitudes at one glacier averaged 74 m. The pattern of equilibrium line altitudes changed shape from year to year, with average variations of 50 m about the mean change. A map of the regional pattern of equilibrium line altitudes shows variations of 1000 meters from the south to the north side of the range, but no major trend from east to west.

* This chapter is in preparation for submission to *Journal of Glaciology*.

INTRODUCTION

There is much interest in glacier fluctuations, as changes in glacier volume affect sea-level rise and fresh-water resources (e.g. Harrison and others, 1983). Glaciers are also sensitive indicators of climatic variations. The glaciers of Alaska and adjacent portions of Canada (collectively referred to, in this paper, as Alaska glaciers) make up 13% of the mountain glacier area on earth. Several studies have estimated the rate of volume change of Alaska glaciers, using various calculation methods and sources of data (Meier, 1984; Dyurgerov and Meier, 1997; Dyurgerov, 2002; Arendt and others, 2002). However, no study thus far has measured mass balance or volume change of every Alaska glacier. For example, Arendt and others (2002) used a sample representing about 20% of the glacierized area in their calculations. As a result, they and others rely on extrapolation of limited data to the remaining unmeasured glaciers in order to estimate rate of change of glacier ice volume.

Just how to best extrapolate volume change measurements has not yet been established. Arendt and others (2002) defined seven geographic regions based on mountain ranges, and computed an average curve of thickness change versus elevation within each of those regions. They used those seven average thickness-change curves to estimate the volume change of the unmeasured glaciers. The implicit assumption in the regional extrapolation method is that the measured glaciers form a representative sample of the remaining nearby glaciers. Sapiano and others (1998) looked at how representative the volume changes measured on individual glaciers are of the surrounding regions. They showed both positive and negative examples of representative glaciers, but mostly found that the glaciers they measured were not representative of entire regions.

A regional extrapolation scheme does not take into account variations in temperature, precipitation or surface aspect within the geographic regions. Aðalgeirsdóttir and others (1998) showed that from 1950's to the mid-1990's, the glaciers on the south side of the Harding Icefield thinned more than those on the north side, but found no substantial differences between the west and east side glaciers. This is an example of spatial patterns of glacier changes which would not be represented by a

random sampling of glaciers. In this case the variations in thinning rate are due in part to the proximity of the southern glaciers to the ocean.

In the long term, we seek an extrapolation method which does not rely solely on a somewhat arbitrary grouping of glaciers, as by mountain ranges. Such a scheme would demarcate regions of similar climatic conditions, or perhaps even identify the patterns of climatic variation within and across regional boundaries. The basis for such a scheme must be easy to measure over large geographic areas and must be related to the interaction between a glacier and the climatic forces which shape it. This paper examines one candidate which could serve as a basis for the climatic classification scheme just mentioned: equilibrium line altitude.

An equilibrium line separates a glacier into a zone of net mass gain and a zone of net mass loss. At the equilibrium line, the sum of accumulation processes are balanced exactly by the sum of ablation processes (Paterson, 1994). By measuring the elevation of the equilibrium line (commonly referred to as the equilibrium line altitude or ELA) one obtains a single number which summarizes the preceding year's climatic effect on a glacier. Unlike a glacier-wide mass balance, the ELA is not strongly related to the hypsometry of the subject glacier. On the other hand, an ELA does not tell us anything about the relative importance of accumulation and ablation processes, which the results of a mass balance field program often can.

In general, the equilibrium line is not necessarily an observable surface feature. On a truly temperate glacier, the zone of superimposed ice (Benson, 1961) is insignificant, and the equilibrium line essentially coincides with the late summer snow line (Paterson, 1994). Trabant and Mayo (1985) estimate the contribution of internal accumulation to mass balance on two coastal Alaska glaciers using firn temperature measurements. They estimate that internal accumulation, including superimposed ice and capillary retention of liquid water in the firn, accounts for 5% of the total annual accumulation on each of the two coastal glaciers. They also note that the amount of internal accumulation is related to increasing latitude. They do not give any estimates of the areal extent of or the elevation interval spanned by the superimposed ice zone. We

will use the late-summer snow line as a proxy for the equilibrium line, but recognize that this introduces some error in the absolute ELAs. Within our study region we are interested in the relative patterns of ELAs, and over a small latitudinal range variations in the extent of superimposed ice should be small. If future work spans larger latitudinal ranges then this may become more of a concern.

The main question we propose is, how accurately can a regional distribution of Alaska glacier ELAs be mapped? A related topic of interest is how such a regional ELA pattern varies time and space, and how these variations affect the applicability of the regional mapping results. If there is no discernible spatial pattern to the ELAs, or if the pattern we do see is incoherent from one year to the next, then perhaps ELAs can not help in improving the regional extrapolation scheme mentioned above. To answer this query, we used historical aerial photographs and scenes acquired by the Thematic Mapper instrument onboard the Landsat 5 satellite. We also collected two years of snow line position and elevation data using an integrated airborne elevation profiling and digital-video imaging system flown in a single-engine airplane. This video/profiling system enabled us to collect both planimetric and hypsometric information about the observed snow lines and is described in Appendix 3.1. Our study area covers the western Chugach Mountains in Southcentral Alaska (Fig. 3.1). The aerial photographs and video images of late-summer snow lines allowed us to determine equilibrium-line altitudes on 11 glaciers during 12 years between 1950 and 2001. The Landsat scenes, in conjunction with the aerial observations, allowed us to create a map of the distribution of equilibrium-line altitudes throughout our study area.

MEASURING EQUILIBRIUM LINE ALTITUDES

Mass-balance methods

A direct way of locating an equilibrium line altitude is to measure the specific balance curve over a portion of a glacier which crosses from the accumulation zone into the ablation zone. This is typically done using mass balance stakes and measuring the

near surface snow and firn density (Østrem and Brugman, 1991). Specific balance curves often change in slope in the vicinity of the equilibrium line (ref. Fig. 9 in Coffin and others, 1990), so ideally several measurement sites would be distributed throughout the range of expected equilibrium-line altitudes to minimize errors due to interpolation. To truly map the location of the equilibrium line, the stakes would also have to be installed across the width of the glacier to measure lateral variations in specific mass balance. Increasing the number of stakes and pits certainly increases the cost of a mass balance program. In most cases, then, the accuracy of equilibrium line records will be affected by the need to interpolate between poles, and by the assumption that specific mass balance is a function of elevation only. Resource limitations also confine field measurements to just a few glaciers in any region. For example, there are just four or five long-term mass-balance programs in the state of Alaska. Resorting to mass-balance methods of identifying the equilibrium line does not necessarily solve the problem of taking internal accumulation into account. Trabant and Mayo (1985) point out that the effect is commonly ignored, and additional measurements are necessary.

Reconnaissance methods

We do not always have to resort to mass balance stakes and density pits; we can simply map the snow lines. The snow line referred to here is the location of the lower extent of snow remaining on a glacier surface from the previous accumulation season. The snow line is typically visible as a distinct transition in brightness due to the difference in albedo between ice or firn and the snow. The contrasting brightness is usually visible in aerial photographs or satellite images. In the case of a broad transition from snow cover to bare ice, the snow line follows where the snow cover and bare ice surfaces are in equal proportions. Reconnaissance methods afford the possibility of covering large areas in a short amount of time. They can be thwarted by inclement weather, cloud cover, or a layer of fresh snow. In the simplest, although not necessarily most efficient, form of the reconnaissance method observers can record snow line positions by going to the glaciers or viewing them from nearby observation points on the

ground. If a snow line is observed before or after the time when it is at its maximum elevation, a seasonal correction must be made to account for the date of the observation. When looking at ELAs, a map correction must be made to account for the change in the elevation between the mapped surface and the glacier surface at the time of the reconnaissance mission. One of the goals of this paper is to assess the uncertainties in reconnaissance measurements of ELAs, especially on a regional scale.

Aerial photographs typically cover an area on the order of hundreds of square meters (covering a portion of one glacier) up to hundreds of square kilometers (covering many glaciers). Some advantages of aerial photography are that flights can be timed to take advantage of cloud free conditions or in some cases can fly beneath the clouds. The digital-video imager we used has the same characteristics just mentioned.

Satellite remote sensing platforms of interest in regional glacier studies typically cover thousands to tens-of-thousands of square kilometers. These instruments acquire imagery in the optical (visible to infra-red) and microwave spectra. The large areal coverage from satellites is a great asset, and the lower resolution compared to aerial photography is not generally a concern in the sort of equilibrium line study we describe here.

Landsat imagery falls in the optical sensor category. There has been a series of Landsat spacecraft going back to the early 1970's and in their more recent incarnations (Landsat 4 through 7) back to the early 1980's. Because Landsat uses an optical imaging system (divided into discrete spectral bands), the data are easily compared with aerial photographs. Landsat imagery can be expensive, priced at several hundred U.S. dollars per scene, but once an image has been purchased it can be shared freely. Another optical sensor based satellite is the Advanced Spaceborne Thermal Emission and reflection Radiometer (ASTER) which was launched in 1999. At \$55US for an ASTER scene which covers 10% of the area of a Landsat scene, the two types of images are of comparable cost. (ASTER images are free to certain user groups, including NASA funded researchers.) ASTER and Landsat images are also comparable in spectral coverage and resolution.

There have been several synthetic aperture radar (SAR) satellites and these have proven extremely useful in many aspects of glacier studies, especially when applied to large valley glaciers, icefields and ice sheets. Glacier facies can be identified by their distinct backscatter signals, allowing identification of dry snow, wet snow, and bare ice (Ramage, 2000). Unfortunately, SAR imagery is not so straightforward when used to map equilibrium lines. Because radar energy can penetrate a glacier surface, the current year's snow line can be obscured by an older firn limit which is located at a lower elevation (Hall and others, 2000; Craig Lingle, personal communication, 2000). Smaller glaciers nestled among tall mountains and ridges are often obscured in SAR imagery due to the side looking nature of the instruments.

Another option available is to combine several types of images to take advantage of the benefits of each. In this study we used historical aerial photographs in order to look back as far as 1950, newly acquired imagery from our video/altimeter system to provide more recent information with concurrent altimetry data, and Landsat imagery to cover our entire study area.

PREVIOUS STUDIES

Meier and Post (1962) determined the geographic distribution of equilibrium line altitudes from aerial photography acquired between mid-July and late-September, 1961, over glaciers ranging from California to Alaska. Because the photograph dates did not all coincide with the end of the summer season, they made a seasonal correction using "knowledge of the approximate time of the end of the ablation season" and "a subjective appraisal as to the rate at which the snow line had retreated based on weather records and the apparent thickness of the snowpack." They acquired photographs of the St. Elias, Chugach and Kenai area glaciers from 10 August to 15 August. There is no mention of which maps were used, although they do lament the "lack of accurate large scale topographic maps." In the St. Elias Mountains their observations showed that the equilibrium line altitudes rose with an average trend of 13 m km^{-1} from an elevation of 763 m near the coast to 2,225 m at a point 110 km inland.

In Østrem's (1973) study of transient snow lines in western Canada, the snow line elevations were compared to four steady state equilibrium line altitudes. (A steady state ELA is the ELA which, for a specified glacier, corresponds to a glacier wide mass balance of zero and can be calculated from several years of corresponding mass balance and ELA measurements.) The locations of the snow lines were measured from a major aerial photography campaign covering 141 glaciers in the Rocky Mountains west of Calgary and 37 glaciers in the Coast Mountains north of Vancouver from 22 to 24 August 1966. The snow-line elevations were then determined from existing Canadian National Topographic System maps, and in the one example given the map was based upon 1956 aerial photographs. In both of the study areas the snow-line elevations rose from southwest to northeast; the trend was 3.8 m km^{-1} in the Rocky Mountains and 8.9 m km^{-1} in the Coast Mountains.

Aniya and others (1996) used Landsat scenes acquired on 14 January 1986 to measure equilibrium line altitudes as part of an inventory of the outlet glaciers of the Southern Patagonia Icefield, Chile and Argentina. They compared three of the snow lines from the mid-summer Landsat scenes with previously published equilibrium-line locations that were derived from aerial photography and subjective estimations of the magnitude of seasonal corrections. It was determined that despite the early date of the Landsat images, the snow lines provided good estimates of the equilibrium lines so no corrections were made for a subsequent rise in equilibrium line altitude due to ablation during the second half of the summer. It is not clear which maps were used for elevation information and there are references to the poor quality of the hypsometric information in one series of maps used. We fit a second order polynomial surface to the equilibrium line altitude data published in their study to determine the dominant spatial patterns. In the northern portion of the icefield, the dominant trend in equilibrium line altitudes rises 3.5 m km^{-1} from the northwest to the southeast. In the southern portion this trend is less steep, rising 3.0 m km^{-1} from the southwest to the northeast.

On the Argentinian side of the northern Patagonian Andes, Rabassa and others (1980) visited over 200 glaciers between February and April, 1978, and measured snow

line altitudes using a hand altimeter or inferred them using the distance on a map and the measured vertical angle from an observation point of known elevation to the snow line. They note that they visited some glaciers in both February and April and did not see a significant change in the snow line position. No corrections to the snow line elevations were made to account for the observation dates. There is no description of the topographic maps used beyond the scale and contour interval. They divided the sampled glaciers into seven horizontal bands, each covering 20 minutes of latitude, and computed the trend in equilibrium line elevations with distance from east to west. These trends vary from 4 m km^{-1} to 35 m km^{-1} in the different bands.

Beginning in 1977 a regional snow line survey has been carried out nearly annually in New Zealand's Southern Alps using oblique aerial photography (Chinn, 2001). The photographs are usually acquired in March or early April, although the surveys have been as early as 15 February and as late as 18 April (Chinn, 1995). Chinn notes the difficulty in timing flights for the end of the summer season due to bad weather and logistical complications. Two different series of topographic maps (the newer NZMS 260 series and the older NZMS 1 series) have been used over the years to determine snow-line elevations. Neither a map correction nor a seasonal correction is mentioned in the papers describing this project. Nonetheless, the elevations are reported as ELAs. The regional extent and nearly continuous time series of this ongoing study provide an excellent opportunity to analyze trends and inter-annual variations in glacier-climate interactions. For example, Lamont and others (1999) show that from 1977 to 1997 the trend of snow-line elevation with distance across the north-south aligned Southern Alps varied from 1.6 to 10.9 m km^{-1} . The standard deviation of the annual averages of the ELAs (not including the three years with less than three glacier observations) is 46 m.

Hall and others (2000) used SAR data to study the position of the firn line on a monthly basis from January 1994 through March 1998 on the Hofsjökull ice cap, Iceland. They found that in most of their winter images, the firn line was visible, rather than the

previous summer's equilibrium line. In the summer images, they were able to track temporal and spatial patterns of the onset of snow melt and the appearance of bare ice.

THE SOURCE IMAGERY

For our study, we collected images of snow lines from the three sources mentioned above: historical aerial photographs, newly acquired aerial digital-video images, and Landsat 5 Thematic Mapper scenes. Regardless of the source, we set several criteria for each image; each had to depict the snow line so that it could be located geographically (via ground control or knowledge of the camera location and orientation), be unobscured by clouds, be taken close to the end of the summer but not too late such that new snow had fallen, and finally, the exact date of acquisition had to be known in order to evaluate the magnitude of the seasonal correction.

We explored several archives for appropriate historic photographs, mainly the vertical photography acquired in 1950 by the U.S. Geological Survey (USGS) to prepare topographic maps, the USGS Ice and Climate Project (ICP) photographs taken by Austin Post, Robert Krimmel, and Larry Mayo from the 1960 through 1996, and the Alaska High Altitude Aerial Photography (AHAP) collection which covers most of Alaska and was flown from 1978 to 1986. (The USGS topographic mapping photographs are currently archived at the USGS EROS Data Center (EDC) as part of the Index/Map collection. The ICP and AHAP photographs are currently held by the Geophysical Institute GeoData Center, University of Alaska – Fairbanks.) We searched only for photographs acquired between 5 August and 9 September, to limit the magnitude of the seasonal corrections, and (except in the case of Allen Glacier) studied glaciers for which we had at least some laser altimetry data so we could quantify the map corrections. After searching through approximately 1000 photographs, we found 30 photographs covering snow lines on 11 glaciers located within our study area. Table 3.1 lists the images, along with the sources and dates for each. Figure 3.2 shows a portion of one of the photographs covering a snow line.

The video/altimeter system made it possible to coordinate the collection of new imagery with glacier profiling work which was already planned. The airborne elevation profiling system includes a global positioning system receiver used to locate the airplane throughout each flight, a fiber-optic gyroscope to determine the attitude (pitch and roll), and a laser rangefinder to measure the distance from the airplane to the glacier surface (Echelmeyer and others, 1996). The camera is a compact digital video camera operating at 15 frames per second – this allows us to select from hundreds of images taken as we pass over a portion of the glacier. All of the equipment communicates with a central data-acquisition computer to synchronize timing of the measurements. Post processing of the position, attitude and rangefinder data, along with the selected digital images allows us to create a rectified (vertically oriented) georeferenced mosaic from a segment of the video. A more detailed description of the video/altimeter system is given in Appendix 3.1, and the details of the image rectification and geolocation algorithm can be found in Appendix 3.2. Using a number of the images acquired in late August and early September, 2000, and at about the same time in 2001, we were able to determine the position of the snowline on 10 glaciers using a total of 16 mosaicked images. Figure 3.3 shows one of the mosaics covering a terminus and snow line.

The third source of snow-line imagery we used was the Landsat 5 Thematic Mapper. We obtained two overlapping cloud-free scenes which were already in the public domain: path 66/row 17 acquired on 25 August 1987 and covering the eastern portion of our study area, and path 67/row 17 acquired on 28 July 1986 and covering the western portion. Because we did not purchase new scenes, we were not able to obtain coverage of a small portion of our study area which included Sherman and Sheridan glaciers. The snow line elevations observed in these two images were used to explore relative spatial patterns or trends in the distribution of equilibrium line elevations and the spatial variability of individual equilibrium lines relative to those general patterns. They were not expected to give us absolute equilibrium line positions and elevations for the two years covered. Therefore, the early acquisition date of the 1986 scene, and the different years covered by the two scenes, did not necessarily preclude their use in our

study. We will discuss the relative variations in equilibrium line patterns from year to year and throughout a summer. Figure 3.4 shows a subset of the 25 August 1987 Landsat scene after image processing and identification of the snow lines, as will be described below.

METHODS

Measuring ELAs from photographs and video images

The snow lines in the photographs were manually transferred to the corresponding USGS 15 minute series topographic maps using rock and ice features for spatial references, and the planimetric positions were digitized and imported into a geographical information system (GIS) database. The video mosaic images, already in digital format, were imported directly into the same GIS database, where we were able to extract the locations of the snow lines using cursor tracking along the visible demarcation between snow and ice or firn.

Once the photograph and video derived snow line positions were entered into the GIS database, we extracted the corresponding elevations from the USGS digital elevation models (DEMs). (The profiling system altimetry data typically ran along one or two tracks over the glacier. We used the DEM to account for relative surface elevations, correcting in a later step for the average offset between the DEM and profile data along the equilibrium line.) We then took the average of the elevations at 60 m postings along each snow line. Seasonal corrections to the snow line elevations were necessary because of the range of acquisition dates relative to the end of summer. There are no published observations of daily snowline rise over a summer season in the vicinity of our study region, so we used the output from a glacier mass balance model which produces, among other results, a time series of snow line elevation for each year of weather station data input (Tangborn, 1999). A graph depicting the average of the modeled 1950 to 1998 snow line elevations each day over the summer season for the Seward/Malaspina glacier system, shows that the maximum snow line elevation is reached on September 3, before

winter snow accumulation quickly brings the snow line back down the glacier (Fig. 3.5). The Seward/Malaspina glacier system is three- to four- hundred kilometers east of our subject glaciers. However, because the snow line rise curve was only used as a correction to the actual observations, the lack of snow line rise data specific to each glacier and year, and the lack of field based observations was not a large source of uncertainty. This is the snow line rise curve. The difference in snow line elevations between the date of image acquisition and the end of the summer ablation season is the seasonal correction. We added this correction to the measured snow line elevation.

The snow line elevations still needed a correction to account for surface elevation change between the DEM (which was created from the USGS topographic maps made from 1950 aerial photographs) and the snow line image acquisition dates. The snow lines surveyed with the video/altimetry system all (except Allen glacier) had surface elevation data acquired on the same day as the video images, so the difference in elevation between the altimetry data and the DEM was simply added to the average snow line elevation. The aerial photographs were acquired at times between the DEM surveys and our altimetry flights. We assumed that the surface elevation changes during the intervening years occurred at a constant rate, so we scaled the DEM-to-altimetry elevation changes using a linear interpolation as follows:

$$\Delta z_{\text{photograph-DEM}} = \left(\frac{\Delta t_{\text{photograph-DEM}}}{\Delta t_{\text{altimetry-DEM}}} \right) \Delta z_{\text{altimetry-DEM}} \quad (1)$$

The DEM elevations represent the 1950 surface. The map and seasonal corrections transform snow line elevations into ELAs. Table 3.2 shows the ELA data compiled from the two airborne sources.

Figure 3.6 shows the range of typical seasonal and map corrections as applied to Sherman Glacier. The circles in this plot are the elevations of the snow lines with no corrections applied. The squares are above the circles because of the seasonal corrections, and the X's have generally been brought back down by the amount of glacier thinning at the equilibrium line since the map was made.

Measuring the regional distribution of snow line elevations from Landsat scenes

Using the ideas of Hall and others (1987) and Paul (2000), we took the ratio of band three to band five and also the ratio of band four to band five to investigate which would best highlight the transition from ice or firn to snow. In both cases, the ratio of band three to band five gave a better delineation of the snow lines. We then used an automatic contour tracing algorithm to demarcate the pixel gray level (the “digital number”) which best fit the snow line transition, as can be seen in Figure 3.4. As with the video images, we imported the Landsat scenes into the GIS database, used cursor tracking to trace the snow lines (choosing not to automate this process because of the large number of snow lines which appear outside of the glacier boundaries and the lack of high resolution glacier boundary masks). The red line segments in Figure 3.4 are the snow lines traced from the underlying Landsat image (25 August 1987) and the blue line segments coincide with the snowlines we traced on the overlapping portion of the 28 July 1986 Landsat image. The green line segments represent the equilibrium line positions derived from the 1978 AHAP photographs. (We applied a seasonal correction in the map plane to the 1978 snow line positions to derive the corresponding equilibrium line positions. We did this by moving each point of a given snow line along the path of steepest ascent on the DEM surface. The point was moved until it had been shifted by the modeled seasonal elevation correction.)

The two Landsat scenes we used were acquired on different dates and in different years. We are interested in combining the two scenes to cover the entire study area to give us a picture of the relative distribution of snow lines throughout the region. Below we will compare the Landsat derived snow line elevations to aerial photograph derived ELAs and relate them to each other. In order to combine the observed snow line positions from the two scenes, we had to ascertain whether the spatial distribution of snow lines was consistent from one scene to the other. The overlapping portions of the Landsat scenes include roughly 1/4 of the glacierized area in our study region. The snow lines derived from the two Landsat images within the overlapping portions coincide to within 800 m horizontally on all but two of the glaciers. The majority of the snow lines

agree to within 200 m horizontally. The larger disagreements were found on large, flat glaciers, reducing the associated differences in elevations. The 1987 image snow lines are consistently higher or nearly identical, but almost never lower, than the 1986 image snow lines. Within the overlapping region, the average snow line elevation in the 1987 image is 28 m higher than in the 1986 image. We added this 28 m to all of the elevation points from the 1986 image before merging the two sets of snow line elevations into one database containing 8794 point measurements on approximately 75 glaciers

ERRORS IN THE ELA MEASUREMENTS

There are several sources of error in the ELA measurements. First, there are errors in our ability to identify the snow line in the source imagery. This could be due to poor contrast or a broad transition region on the glacier from bare ice to snow, or, in the photographs, due to inadequate control points to locate the snow line on a map. Contrast did not limit our measurements, and we discarded photographs without good control. Fortunately, errors in the horizontal plane do not propagate into larger errors in elevation on most glaciers as the surface slope is typically on the order of five degrees, and so this is not expected to be a significant uncertainty.

The next source of errors arises from extrapolation due to an image which depicts only a portion of the snow line. Some images cover the entire snow line and so this is not always a concern. On some glaciers the snow line closely follows a single elevation contour, but in extreme cases we observed snow lines which varied in elevation by several hundred meters across multiple tributaries. In all of the cases of poor coverage of the snow line, we were able to extrapolate using spatial patterns observed during other years. We do not believe that this was a significant source of uncertainty either.

The date of image acquisition, relative to the end of the summer season also introduces some uncertainty. We countered this with the seasonal corrections and by limiting our snow line images to those acquired after 5 August, so the maximum adjustment was 100 m. Our latest images were taken on 9 September, at which time the modeled curve had fallen by 10 m from the late summer maximum. We were more

conservative with the later cutoff dates because a single snow fall can lower the snow line far more quickly than a hot summer day can raise it. The average snow line correction was 28 m and we took this value to represent the uncertainty in the corrections.

Because we relied on the USGS DEMs compiled from 1950 aerial photography for our elevation data, we made the map corrections. If we had not corrected for surface elevation changes at all, then our most recent ELAs would have been off by 40 m too high on average. We used the elevation profile data to quantify this effect, making the assumption in Equation (1) that the elevation changes had occurred at a constant average rate from 1950 until the times of the profiling. Arendt and others (2002) showed that the rate of surface elevation change over a period of five to seven years can be double the average rate found over a 40 year time period. Using a typical average thinning rate and assuming that the 10 years immediately prior to an aerial photograph coincided with one of these periods of faster-than-average thinning, the linear interpolation scheme we used would be off by less than 10 m.

The quadrature sum of the uncertainties in our seasonal and map corrections is 30 m, and this is the uncertainty in the aerial photo and video derived ELAs.

ELA VARIATIONS WITH TIME

We are interested in determining the year-to-year variability of the spatial patterns of ELAs. Figure 3.7a shows the equilibrium line altitudes from the photographs and video images for the four years with the best coverages, along with the remaining years of ELA data as individual points. (We plotted the ELAs as a function of Northing in the UTM system because the 11 glaciers we measured with photographs and video are located mostly along a north/south transect. The Northing coordinate also conveniently corresponds well with the glaciers' distances from the coast and so is a proxy for increasing continentality.) The variations between individual years include systematic shifts common to all of the glaciers and changes in the relative elevations between glaciers. In order to quantify the relative variations we computed the difference between the ELA measured at each glacier in 1950, 2000, and 2001, compared to the 1978 ELA

(Fig. 3.7b). The standard deviations of those differences are 47, 33, and 60 m, respectively. This suggested that the combined Landsat snow line data could be used to represent the relative ELA patterns found in different years, or if just one or a few ELAs were known for a given year, then the entire pattern could be shifted up or down to fit the known elevations. Such an application would correspond to an uncertainty of approximately 50 m due to inter-annual variability of the spatial pattern.

Another facet of time variations in our data is the inter-annual variability of the ELA on an individual glacier. This is related to the question of whether a systematic study of ELAs can lend some insight to climatic trends. We amassed the ELA measurements for Sherman Glacier, with a total of nine years of data (the most for any glacier in our dataset). We used meteorological data (total monthly precipitation and average monthly temperature) from Cordova to extend the Sherman Glacier ELA data in the form of a predicted time series of ELAs from 1950 to 2001. We investigated the correlations between the measured Sherman glacier ELAs and various combinations of months of the meteorological data. The best correlation was found using a two parameter fit to the total precipitation from January to May and the average temperature in July and August. For the nine years of ELA measurements, our least squares fit had an r^2 value of 0.56. The predicted ELAs are plotted in Figure 3.8 along with the measured ELAs. The predicted time series has a standard deviation of 74 m, and the nine observed ELAs have a standard deviation of 63 m. The trend of ELA over time was indistinguishable from zero. Applying the relationship between the change in ELA with a change in temperature computed by Kuhn (1989) shows that the $+0.02 \text{ K a}^{-1}$ trend in average summer (July, August) air temperature observed in Cordova from 1948 to 2002 would correspond to a 1.2 m a^{-1} change in equilibrium-line altitude. This is dwarfed by the inter-annual variability and the observed trend in meteorological records of winter precipitation would actually significantly reduce the expected rate of ELA change.

SPATIAL VARIABILITY OF ELA'S

We used the Landsat scenes to measure snow line positions and to derive snow line elevations. We can not make map corrections on most of the glaciers which appear in the Landsat scenes because of our limited airborne profiling system altimetry coverage. Instead of making seasonal and map corrections to the Landsat data, as we did with the aerial photograph and video data, we will compare the Landsat snow line elevations with the 1978 ELAs. Then we can shift the Landsat snow line elevations up or down to find the best fit with the 1978 ELAs. The elevations plotted in Figure 3.7b show that the Landsat snow lines average 26 m lower than the 1978 ELAs, with a standard deviation of 60 m. This standard deviation is similar to those we found between years of aerial photograph data. We added a 26 m offset to raise the entire set of Landsat derived snow line elevations to the level of the 1978 ELAs.

Because the main goal of this study was to look at the regional distribution of ELAs, we used several methods of fitting surfaces to the elevation points in the combined Landsat dataset. By smoothing the data, we also can characterize the spatial variability of individual ELAs relative to the surrounding area. A high order polynomial fit, or a spline surface would match the data well, but the general spatial pattern which may be explained by climatic and meteorological processes would be obscured by numerous local peaks and valleys. A low order polynomial fit, or a fit which smooths over the data from several adjacent glaciers is easier to interpret in terms of the dominant trends in elevations. In the end we settled on an inverse distance weighting interpolation scheme with a weighting factor of one over the distance and a circular neighborhood sized to average over 900 data points. This resulted in a typical neighborhood radius of 20 km. In other words, we smoothed the data over a length scale of approximately 20 km. Our result, drawn with 100 m contour intervals, is shown in Figure 3.9. Keeping the 60 m inter-annual variability in the pattern of relative ELAs in mind, the interpolated elevation map can be taken to represent the 1978 ELA distribution. All of the measured snow line positions are also plotted in this figure as thick black line segments. The RMS prediction error of the interpolation is 100 m; this is a measure of how far off a typical individual

snow line elevation is from the smoothed surface. This prediction scatter tells us that the ELA of an individual glacier can be expected to vary by 100 m relative to the surrounding glaciers. This is due to local variables such as aspect, and wind and precipitation shadowing. The RMS prediction error of a linear trend line fit to the 1978 data in Figure 3.7a is also 100 m.

The steepest trends in ELAs in Figure 9 are found on the glaciers north and west of Valdez and are aligned approximately perpendicular to the general coast line. The trends show an increase in ELA with distance from the coast of between 11 m km^{-1} and 20 m km^{-1} . The ELA pattern of the glaciers to the northeast of Cordova show a distinct pattern with less steep trend which runs from southeast to northwest.

SUMMARY AND CONCLUSIONS

The uncertainties in our aerial photograph and video measured ELAs were mitigated by our use of seasonal and map corrections. The map corrections were possible because we used an airborne profiling system to measure surface elevations on most of our individual subject glaciers. The seasonal corrections relied on modeled snow line elevation data – reliable field measurements or time sequences of remote sensing measurements in various parts of Alaska would be of great use in validating the model, or supplanting it altogether. Our estimate of the uncertainty in our photograph and video derived ELAs is 30 m, due to uncertainty in the seasonal and map corrections.

Equilibrium line altitudes can be mapped on a regional scale using Landsat imagery, and this has been done in the past. We were able to use one Landsat scene acquired mid-summer because we compared the distribution of snow lines with an overlapping late-summer Landsat scene; the elevation offset was fairly constant between the two sets of snow lines. The difference in the spatial pattern of ELAs from one year to another is comprised of an average offset for all of the glaciers and a $\sim 50 \text{ m}$ random variability among individual glaciers. This implies that the relative distribution of ELAs we mapped using Landsat is relevant to other years by adding a constant elevation offset, but that will not account for the random interannual variations in the pattern at the 50 m

level. The smoothed regional pattern of ELAs showed a trend with distance from the coast (11 m km^{-1} to 20 m km^{-1}) which was similar to the trend reported by Meier and Post (1962) for the St. Elias Mountains (13 m km^{-1}). The ELA on an individual glacier can be expected to vary by $\pm 100 \text{ m}$ from the smoothed regional pattern.

When looking at the time dependent nature of ELAs, the inter-annual variations (74 m at Sherman Glacier) are so large that it is difficult to see any trends over time scales of decades. Our ELA measurements covered between two and nine years out of the last 50 years, demonstrating how large gaps in the data set limit the utility of the results. If a program of regional or worldwide ELA mapping is started, as will become more feasible as the choices of remote sensing satellites increase, it is imperative that there is a commitment to long term continuity. The program undertaken by Chinn (2001) in New Zealand is an excellent example of a long term record covering an entire region, but a rigorous analysis of the effects of seasonal snow line rise would improve the quality of the existing, and yet to be collected data. Fifty uninterrupted years of ELA data would probably show a significant trend, given the current climatic changes with time.

We have mapped the pattern of glacier ELAs over a small region, and analyzed the time and space variations in that pattern. Our results do suggest that refinements can be made in the extrapolation schemes used thus far. The difference in ELAs of the glaciers on the south and north sides of the western Chugach Mountains is around 1000 m . The glaciers to the northeast of Cordova have a different pattern of ELAs than the glaciers farther west. It seems unjustified to group all of these glaciers together into one zone, as has been done in the past. Equilibrium line distributions may help replace broad geographic regions with climatically similar regions in future estimates of glacier volume change in Alaska and elsewhere.

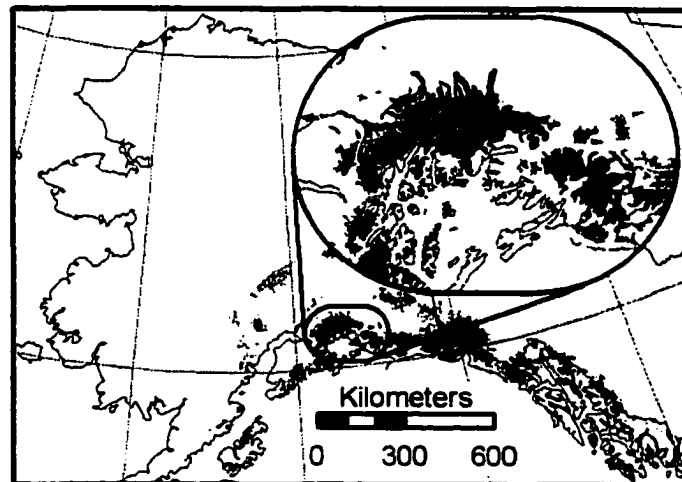


Figure 3.1: Location map. Location map showing our study area, shown in black, in relation to the glaciers of Alaska and adjoining portions of Canada, shown in gray. Our study area coincides with region six as defined in Arendt and others (2002).

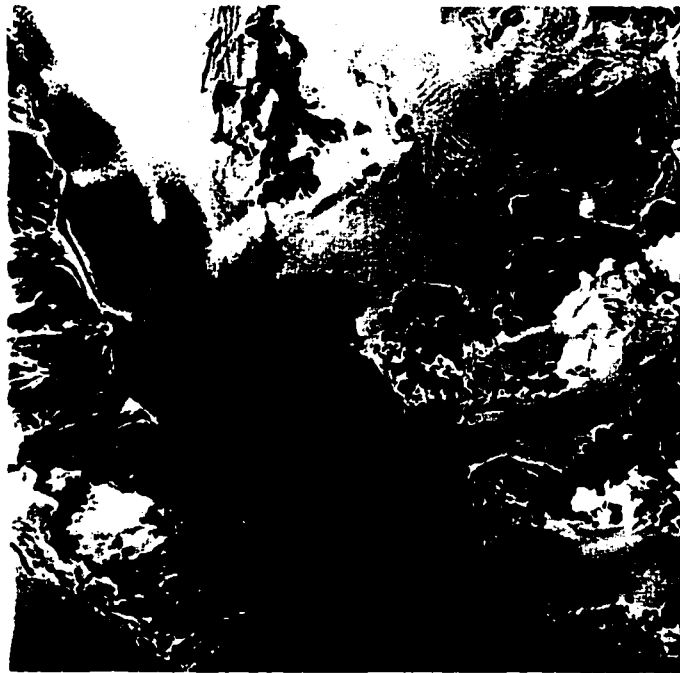


Figure 3.2: Example aerial photograph. A portion of an aerial photograph of a snow line (Scott Glacier, 7 August 1950). The features were oriented, scaled and located by matching the glacier boundary to the topographic map. The glacier is approximately 3 km wide at the bottom of the photograph.



Figure 3.3: Example video mosaic. An example of a mosaic made up of 77 frames of digital video (Worthington Glacier, 24 August 2000). The glacier is approximately 1 km wide at the snow line, and north is to the right.

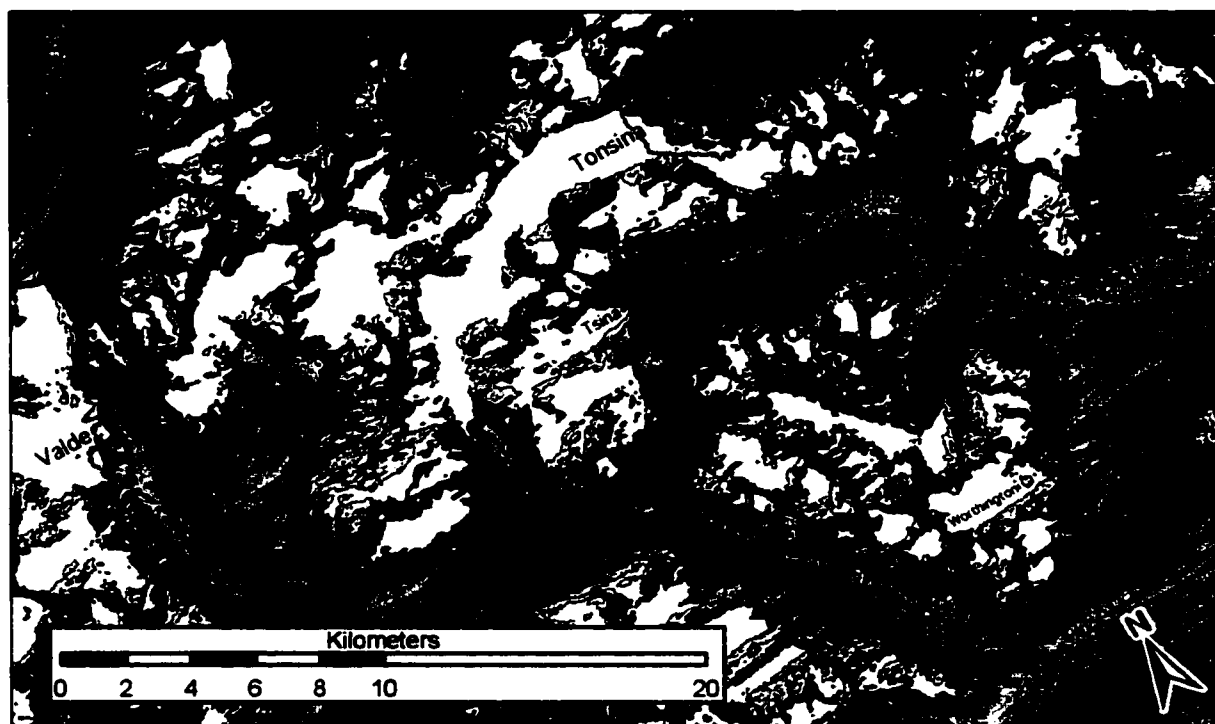


Figure 3.4: Landsat scene. A portion of the Landsat scene acquired on 25 August 1987, with the snow lines from that date shown in blue. The snow lines seen in the overlapping 28 July 1986 Landsat image are shown in red. The equilibrium line positions derived from 1978 aerial photographs appear in green.

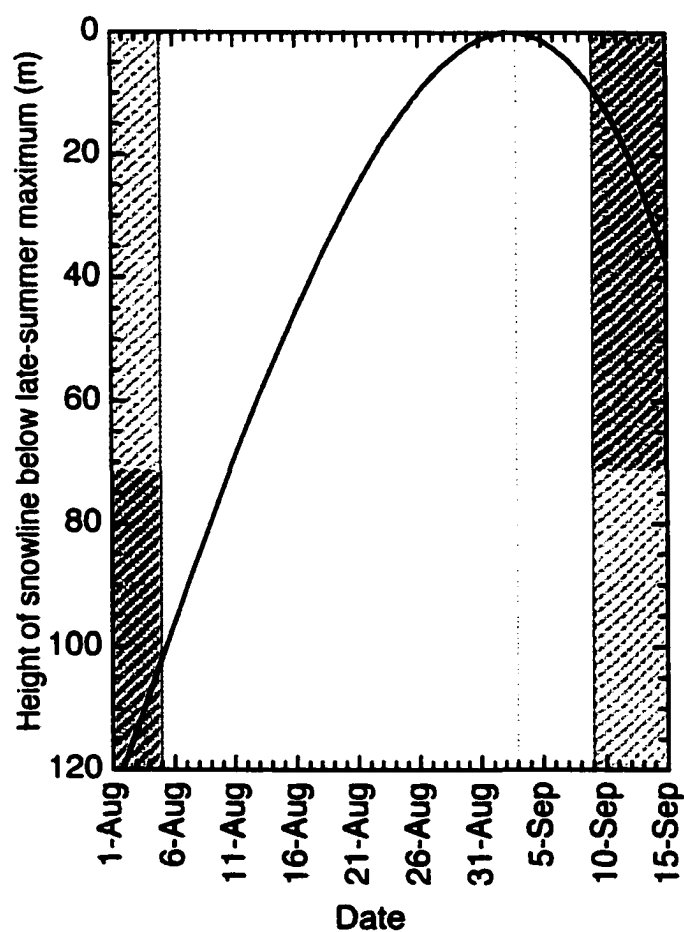


Figure 3.5: Snow line rise. The 1950 to 1998 average modeled snow line rise curve. Source data from the Tangborn (1999) PTAA model for the Seward/Malaspina glacier system. The hash marks on the left and right of the plot show the dates before and after which we did not use photographs due to excessive uncertainty in the seasonal corrections.

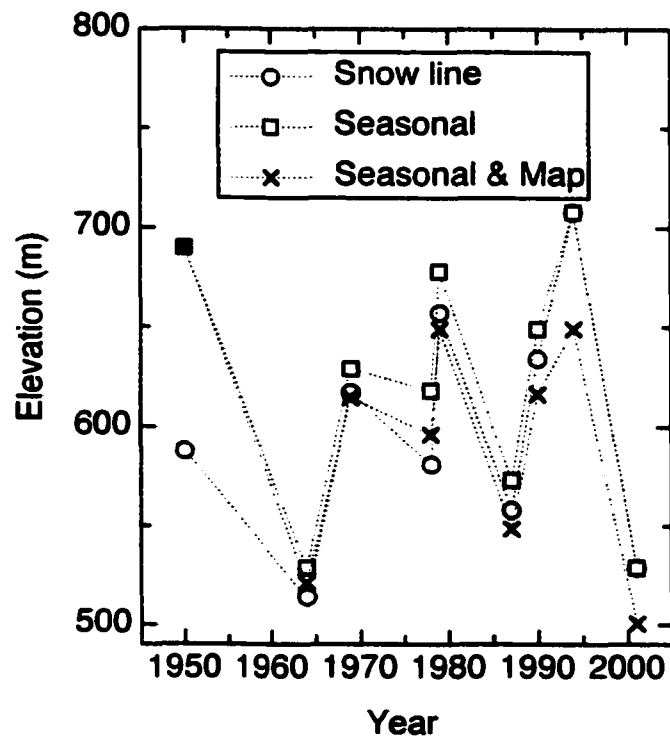


Figure 3.6: Seasonal and map corrections. Plot of the Sherman Glacier snow line elevations with no corrections, with seasonal corrections, and with both seasonal and map corrections. The elevations with both corrections are the ELAs

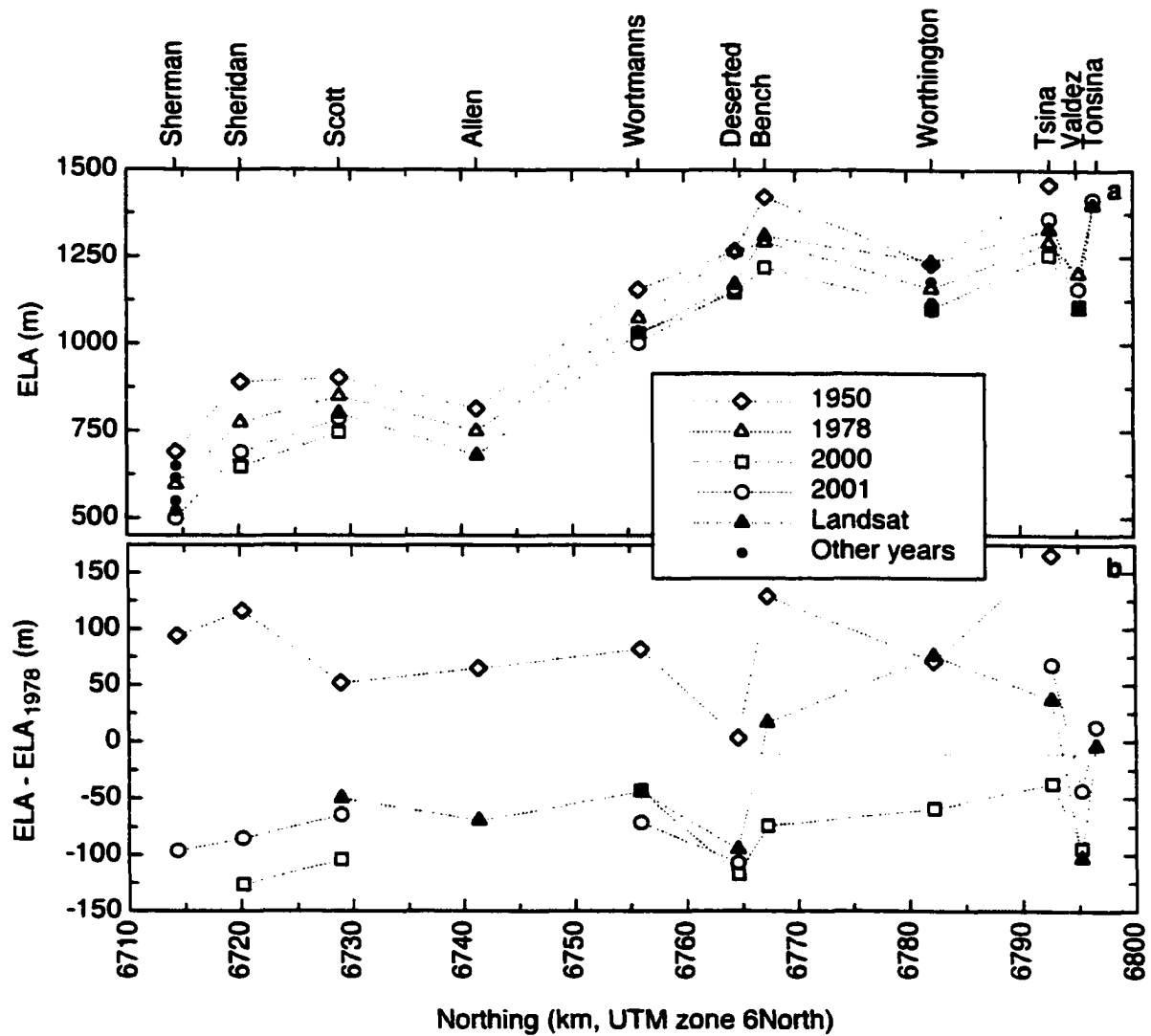


Figure 3.7: ELAs and their variability. (a) Equilibrium line altitudes derived from aerial photographs (1950, 1978, and other years listed in Table 3.2) and aerial digital video (2000 and 2001). Also plotted are snow lines derived from Landsat scenes. (b) Plot showing the relative variations in equilibrium line altitude in 1950, 2000, and 2001, and the relative variations in the Landsat snow line elevations; these are all relative to the 1978 ELAs.

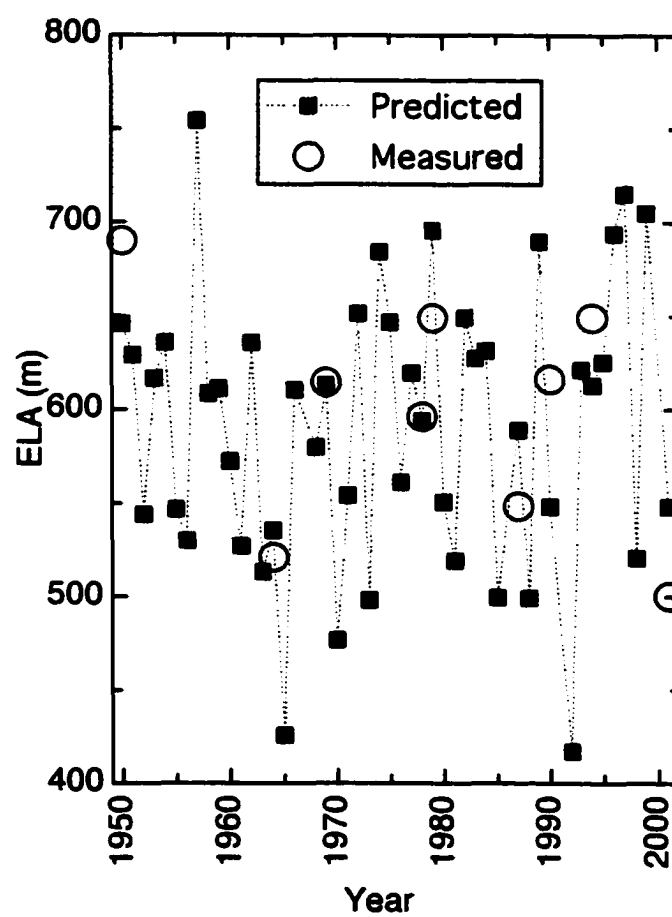


Figure 3.8: ELA time series. Sherman glacier equilibrium line altitudes measured on the aerial photographs (open circles) and predicted using a two-parameter fit to meteorological data at Cordova, Alaska (solid squares).

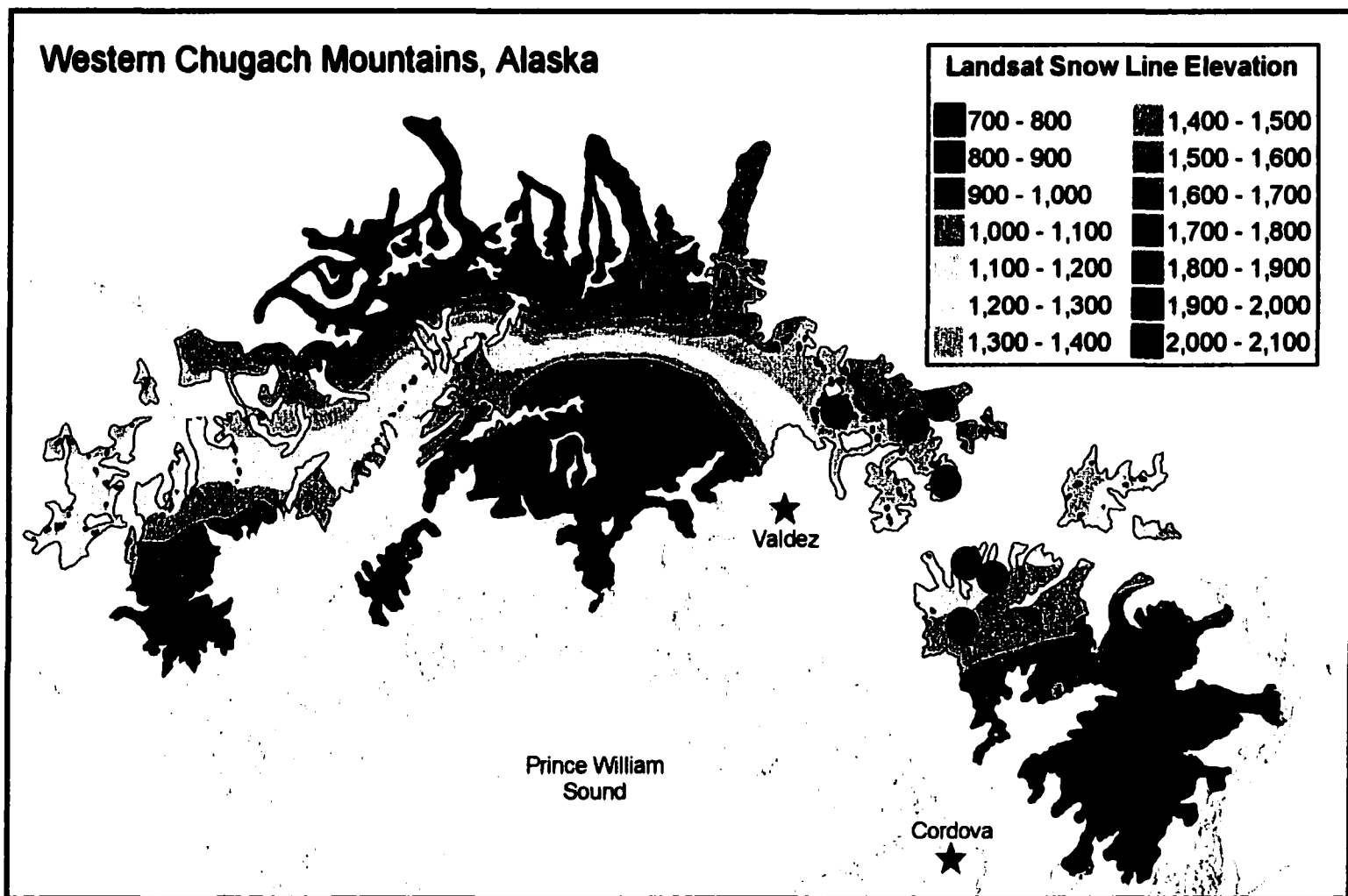


Figure 3.9: ELA spatial distribution. Interpolated map of equilibrium line altitude distribution throughout the western Chugach Mountains, Alaska. These elevations are approximately representative of the 1978 balance year. The thick black line segments scattered around the map are the locations of the actual snow lines measured on Landsat images.

Table 3.1: Source imagery. A list of the images used, including the sources and dates.

<i>Glacier</i>	<i>Source</i>	<i>Date</i>	<i>Glacier</i>	<i>Source</i>	<i>Date</i>
Sherman	USGS	5 Aug 50	Deserted	USGS	12 Aug 50
Sherman	ICP	24 Sep 64	Deserted	AHAP	25 Aug 78
Sherman	ICP	25 Aug 69	Deserted	Video	25 Aug 00
Sherman	AHAP	18 Aug 78	Deserted	Video	25 Aug 01
Sherman	ICP	22 Aug 79	Bench	USGS	12 Aug 50
Sherman	ICP	24 Aug 87	Bench	AHAP	25 Aug 78
Sherman	ICP	7 Sep 90	Bench	Video	24 Aug 00
Sherman	ICP	7 Sep 94	Worthington	USGS	12 Aug 50
Sherman	Video	26 Aug 01	Worthington	ICP	25 Aug 64
Sheridan	USGS	5 Aug 50	Worthington	ICP	24 Aug 65
Sheridan	AHAP	18 Aug 78	Worthington	ICP	3 Sep 77
Sheridan	Video	25 Aug 00	Worthington	AHAP	25 Aug 78
Sheridan	Video	26 Aug 01	Worthington	ICP	13 Aug 94
Scott	USGS	7 Aug 50	Worthington	Video	24 Aug 00
Scott	AHAP	18 Aug 78	Tsina	USGS	12 Aug 50
Scott	Video	25 Aug 00	Tsina	AHAP	25 Aug 78
Scott	Video	25 Aug 01	Tsina	Video	25 Aug 00
Allen	USGS	7 Aug 50	Tsina	Video	25 Aug 01
Allen	AHAP	18 Aug 78	Valdez	AHAP	25 Aug 78
Wortmanns	USGS	12 Aug 50	Valdez	Video	25 Aug 00
Wortmanns	AHAP	18 Aug 78	Valdez	Video	25 Aug 01
Wortmanns	Video	25 Aug 00	Tonsina	AHAP	25 Aug 78
Wortmanns	Video	25 Aug 01	Tonsina	Video	25 Aug 01

Notes: USGS = US Geological Survey mapping photographs, ICP = Ice and Climate Project, AHAP = Alaska High Altitude Aerial Photography, Video = video/altimetry system.

Table 3.2: ELA results. Equilibrium line altitudes derived from aerial photographs and video acquired in the years listed. These elevations include seasonal and map corrections as described in the text. The 25 August 1987 Landsat observed altitudes are listed under "Landsat" and the interpolated map altitudes are listed under "Interp."

<i>Glacier</i>	<i>Equilibrium line altitude in meters</i>													
	<i>1950</i>	<i>1964</i>	<i>1965</i>	<i>1969</i>	<i>1977</i>	<i>1978</i>	<i>1979</i>	<i>1987</i>	<i>1990</i>	<i>1994</i>	<i>2000</i>	<i>2001</i>	<i>Landsat</i>	<i>Interp.</i>
Sherman	690	521		615		596	649	549	616	649		500		785
Sheridan	890					774					648	689		790
Scott	902					850					746	785	800	795
Allen	814					749							680	760
Wortmanns	1156					1074					1031	1003	1030	1060
Deserted	1268					1265					1148	1158	1170	1110
Bench	1422					1293					1219		1310	1205
Worthington	1230	1092	1120		1118	1159				1179	1101		1235	1220
Tsina	1459					1293					1256	1361	1330	1350
Valdez						1203					1109	1160	1100	1330
Tonsina						1404						1417	1400	1390

REFERENCES

- Aðalgeirsdóttir, G., K.A. Echelmeyer, and W.D. Harrison. 1998. Elevation and volume changes on the Harding Icefield, Alaska. *J. Glaciol.* **44**(148), 570-582.
- Aniya, M., H. Sato, R. Naruse, P. Skvarca, and G. Casassa. 1996. The use of satellite and airborne imagery to inventory outlet glaciers of the Southern Patagonia Icefield, South America. *Photogrammetric Engineering & Remote Sensing*.
- Arendt, A.A., K.A. Echelmeyer, W.D. Harrison, C.S. Lingle, and V.B. Valentine. 2002. Rapid wastage of Alaska Glaciers and their contribution to rising sea level. *Sci.*, **297**, 382-396.
- Benson, C.S. 1961. Stratigraphic studies in the snow and firn of the Greenland Ice Sheet. *Folia Geographica Danica.*, **9**, 191-203.
- Bouquet, J.-Y. 1999. Visual methods for three-dimensional modeling. Ph.D. thesis. Pasadena, California Institute of Technology. Submitted May 25, 1999.
- Chinn, T.J.H. 1995. Glacier fluctuations in the Southern Alps of New Zealand determined from snowline elevations. *Arctic and Alpine Research.* **27**(2). 187-198.
- Chinn, T.J. 2001. Glacier ELA monitoring programme. *ICE, news bulletin of the International Glaciological Society.* (126/127), 6.
- Coffin, J.H., D.C. Trabant, L.W. Mayo, C.S. Benson, W.D. Harrison, and H. Roethlisberger. 1990. Mountain glaciers – an overview with emphasis on Alaska. *In: Cold Reg. Hydrol. and Hydraul., Tech Council on Cold Reg. Eng. Monogr.* Ryan, W.L. and R.D. Crissmon, *eds.* Am. Soc. Civil Eng.

- Dyurgerov, M. 2002. Glacier mass balance and regime: Data of measurements and analysis. *Institute of Arctic and Alpine Research Occasional Paper No. 55*.
- Dyurgerov, M.B. and M.F. Meier. 1997. Year-to-year fluctuations of global mass balance of small glaciers and their contribution to sea-level changes. *Arctic and Alpine Res.*, **29**(4), 392-402.
- Echelmeyer, K.A., and 8 others. 1996. Airborne surface profiling of glaciers: a case-study in Alaska. *J. Glaciol.* **42**(142), 538-547.
- Hall, D.K., J.P. Ormsby, R.A. Bindschadler and H. Siddalingaiah. 1987. Characterization of snow and ice reflectance zones on glaciers using Landsat thematic mapper data. *Ann. Glaciol.*, **9**, 104-108.
- Hall, D.K., R.S. Williams, Jr., J.S. Barton, O. Sigurðsson, L.C. Smith, and J.B. Garvin. 2000. Evaluation of remote-sensing techniques to measure decadal-scale changes of Hofsjökull ice cap, Iceland. *J. Glaciol.* **46**(154). 375-388.
- Harrison, W.D., B.T. Drage, S. Bredthjauer, D. Johnson, C. Schoch and A.B. Follet. 1983. Reconnaissance of the glaciers of the Susitna River basin in connection with proposed hydroelectric development. *Ann. glacial.*, **4**, 99-104.
- Kuhn, M. 1989. The response of the equilibrium line altitude to climate fluctuations: theory and observations. *In Oerlemans, J., ed. Glacier fluctuations and climatic change.* Dordrecht, Kluwer Academic Publishers, 407-417.

Lamont, G.N., T.J. Chinn, and B.B. Fitzharris. 1999. Slopes of glacier ELAs in the Southern Alps of New Zealand in relation to atmospheric circulation patterns. *Global and Planetary Change*. **22**. 209-219.

Meier, M.F., and A.S. Post. 1962. Recent variations in mass net budgets of glaciers in western North America. In Ward, W., ed. *Symposium of Obergurgl, Variations of the regime of existing glaciers*. Gentbrugge, International Association of Scientific Hydrology (IASH). Publication number 58.

Meier, M.F. 1984. Contribution of small glaciers to global sea level. *Sci.*, **226**, 1418-1421.

Østrem, G. 1973. The transient snowline and glacier mass balance in southern British Columbia and Alberta, Canada. *Geogr. Ann.* **55A**(2). 93-106.

Østrem, G. and M. Brugman. 1991. *Glacier Mass-Balance Measurements, a manual for field and office work*. Saskatoon, National Hydrology Research Institute Science Report No. 4, 129-31.

Paterson, W.S.B. 1994. *The physics of glaciers*. Oxford, England, Elsevier Science Ltd.

Paul, F. 2000. Evaluation of different methods for glacier mapping using Landsat TM. Proceedings of EARLSeL-SIG-Workshop Land Ice and Snow, Dresden, *EARSeL eProceedings*, 1, 239-245.

Rabassa, J., S. Rubulis, and A. Brandani. 1980. East-west and north-south snow line gradients in the northern Patagonian Andes, Argentina. In *World Glacier Inventory (Proceedings of the Riederalp Workshop, September 1978)*. International Association of Hydrological Sciences (IAHS-AISH) Publ. 126. 1-10.

Ramage, J.M., B.L. Isacks, and M.M. Miller. 2000. Radar glacier zones in southeast Alaska, U.S.A.: field and satellite observations. *J. Glaciol.* **46**(153), 287-296.

Sapiano, J.J., W.D. Harrison, and K.A. Echelmeyer. 1998. Elevation, volume and terminus changes of nine glaciers in North America. *J. Glaciol.* **44**(146), 119-135.

Tangborn, W.V. 1999. A mass balance model that uses low-altitude meteorological observations and the area-altitude distribution of a glacier. *Geogr. Ann.* **81A**(4), 753-766.

Trabant, D.C. and L.R. Mayo. 1985. Estimation and effects of internal accumulation on five glaciers in Alaska. *Ann. Glaciol.* **6**, 113-117.

APPENDIX 3.1: DESCRIPTION OF THE VIDEO AND ALTIMETRY SYSTEM

INSTRUMENTATION

The existing laser altimetry system

Echelmeyer and others (1996) describe the airborne profiling system which has now been in operation for nearly a decade. During that time, elevation profiles have been measured on approximately 100 glaciers. The elevation changes relative to topographic maps and relative to repeated profiles have been processed into volume changes for many of those 100 glaciers, and work is progressing on the rest (Sapiano and others, 1998; Aðalgeirsdóttir and others; 1998, Arendt and others, 2002). Here we will give a brief summary of this system, which is mounted in a small single-engine aircraft. A dual-frequency kinematic GPS receiver logs data during the flight. Post processing of the GPS data against a nearby base station of known coordinates (typically a USGS benchmark) yields the aircraft position at one second intervals; intermediate positions are interpolated using a spline fit. A laser ranging device operating in the near infra-red (905 nm) measures the distance from the airplane to the glacier surface 25 times per second. A 3-axis fiber-optic gyroscope determines the pitch and roll of the instrument platform, also at 25 Hz. At present, the heading is estimated from the tangent of the splined GPS track. An electronic compass or second GPS antenna near the tail of the airplane could be used to give more accurate heading information. All of these instruments communicate with a central data acquisition computer. These data are then processed together to give a profile of glacier surface elevations at points spaced about every 1.5 meters along the surface. Overall the vertical accuracy of the laser profiling system is typically 0.3 m, depending on flight conditions and surface slope.

The camera

For determining terminus positions, snow lines, and the positions of other features, we have incorporated a digital video camera into our profiling system. We

chose a video format, instead of still, because this provides a nearly continuous record of the surface below the aircraft. Digital still cameras typically have better resolution than video, but this is not a major concern for the types of features we are measuring and at the altitudes which we fly. Another handy feature of video is the convenience of archiving. The “mini-DV” video tapes used in our camera hold one hour of video (enough to cover between 5 and 10 glacier termini and EL’s), are smaller than a standard audio cassette.

Analog video requires digitizing of the images, whereas digital video imagery is, of course, already in a convenient digital format. Also, analog video cameras record interlaced video, meaning that the odd and even scan lines are acquired in alternating order (i.e., each image is actually acquired at two different moments). The motion of the airplane between these alternating images results in a loss in image quality. Digital video cameras have a progressive scan mode that captures each frame at one point in time.

Our camera is a high quality digital camcorder (Sony DCR-TRV900). The optics are of fairly high quality, the highest shutter speed (1/10,000 s) exceeds our needs by an order of magnitude, and the camera simultaneously writes a digital time-code to tape and to a (LANC type) serial port. This last feature eliminates the need for a separate time-code generator. The time-code on the serial port is read by the data-acquisition computer so that the video images can be co-registered with position and attitude. This camera records 15 frames per second, which corresponds to 2 to 3 m of travel between images at typical flight speeds. Camera resolution is 640 by 480 square pixels (or 720 by 480 non-square pixels). The minimum focal length is 4.3 mm, with a 3.2 × 2.4 mm CCD imaging chip (equivalent to a 41.3 mm lens on a 35 mm format camera). At 600 m above the surface, a flying height adequate to view the full width of a 500 meter-wide glacier, each pixel represents a square 0.8 × 0.8 m on the glacier.

DATA COLLECTION AND PROCESSING

Field work

The system is capable of simultaneously acquiring altimetry data and video. However, the laser altimeter works best in the range of 100 to 300 m above the surface, while the video camera focal length makes flying heights of 500 to 1000 m best for capturing a reasonable portion of the glacier in the field of view. Thus, we usually fly separate passes over the glacier to acquire each type of data. If there are several glaciers clustered in one area, then we generally fly all of the high passes at once and then descend for the low passes.

The instrument operator in the plane monitors the data stream and a video screen. The operator can tell the pilot to adjust the flight path in order to fit the important glacial features into the field of view. During the altimetry portion of the flight, multiple passes are often flown over the equilibrium line to increase the areal coverage of elevation data.

Image Processing

The operational goal of our system is to measure the three-dimensional world coordinates, (Northing, Easting, elevation), of any point in the video imagery. To accomplish this the image must be rotated and scaled to account for the camera attitude and height above the surface. Surface elevations are taken from the profiling data, generally acquired within hours of the video footage. The effects of the lens and imaging CCD distortion must also be removed; to this end we have determined the relevant characteristics of the camera, including radial lens distortion (sometimes referred to as barrel distortion), principal point offset (the pixel location where the optical axis of the camera intersects the image plane, not necessarily the center pixel of the image), and the measured focal length. This calibration was performed using the “Camera Calibration Toolbox” (http://www.vision.caltech.edu/bouguetj/calib_doc/index.html) developed by J.-Y. Bouguet (1999). This software allows a non metric camera to be calibrated, thereby increasing the accuracy of the images.

Given the camera calibration results, the camera position and orientation, and the elevation at the surface, each “source” image can be rectified and georeferenced. The

general procedure we used is an adaptation of the method used by Bouguet (1999). Lens distortion is removed from the source image, and the undistorted is rotated to vertical and scaled to the known glacier surface elevations. The position of the image is translated by the location of the camera at the time of image acquisition. Narrow horizontal strips are taken from the middle of each image and merged into a mosaic covering the features which passed beneath the airplane while the video camera was recording. The mathematical details of this procedure are found in Appendix 3.2.

Errors in the final horizontal positions are due mainly to errors in gyroscope readings of pitch and roll, airplane crab angle (the difference between the actual azimuth and the tangent to the splined track), and horizontal displacement introduced by a limited number of elevation profiles representing the glacier surface elevations. Of these three factors gyroscope errors dominate, contributing approximately 5 m of uncertainty in horizontal positions per 100 m of flying height above the surface. All of these horizontal errors can be minimized by flying lower (thereby increasing the number of images required to cover the same area).

APPENDIX 3.2: IMAGE RECTIFICATION AND GEOLOCATION

This appendix describes the details of the rectification and geolocation procedure applied to each video image to obtain world coordinates of visible features. We start with the image plane pixel coordinates of the original image,

$$\bar{X}_{image} = \begin{bmatrix} x_{image} \\ y_{image} \end{bmatrix}$$

with the upper left corner being (0,0) and the lower right corner being (640,480). From these we subtract the principal point offset, \bar{P} (the pixel location where the optical axis of the camera intersects the image plane, measured along with the focal length, f , and the second order radial lens distortion coefficient, k , during calibration of the camera), effectively placing the principal point at the origin.

We then divide the translated coordinates by the focal length,

$$\bar{X}_{norm,dist} = (\bar{X}_{image} - \bar{P})/f \quad (1)$$

These coordinates are thus normalized to a unit distance from the center of the lens. They still include the radial lens distortion. In general, the focal length may be different along each axis, in which case a slightly modified version of Equation (1) would apply.

The next step is to remove the radial lens distortion, which is defined by

$$\bar{X}_{norm,dist} = (1 + kr^2)\bar{X}_{norm} \quad (2)$$

where $\bar{X}_{norm} = (x_{norm}, y_{norm})$, and $r^2 = x_{norm}^2 + y_{norm}^2$. Inversion of Equation (2) to obtain

\bar{X}_{norm} is accomplished using numerical, rather than algebraic, methods.

Prior to rotating the normalized undistorted pixels, the z-coordinate of each pixel is defined to be 1. The rotation is then accomplished by a series of rotation matrices accounting first for the relative pointing angles between the camera and the gyroscope, represented by the matrix **A**, and second for the attitude of the plane relative to the (Easting, Northing, up) coordinate system, represented by the matrix **B**. The first rotation matrix is computed as follows:

$$\mathbf{A} = \begin{vmatrix} \cos \theta & \sin \theta & 0 \\ -\sin \theta & \cos \theta & 0 \\ 0 & 0 & 1 \end{vmatrix} \begin{vmatrix} 1 & 0 & 0 \\ 0 & \cos \phi & \sin \phi \\ 0 & -\sin \phi & \cos \phi \end{vmatrix} \begin{vmatrix} \cos \rho & 0 & \sin \rho \\ 0 & 1 & 0 \\ -\sin \rho & 0 & \cos \rho \end{vmatrix}$$

where the angles θ , ϕ , and ρ represent the constant azimuth, pitch, and roll angles (see Echelmeyer and others, 1996, for the sense of these angles), respectively, of the camera's optical axis relative to the instrument platform, measured in the laboratory. The second rotation matrix, \mathbf{B} , is of the same form, using the airplane's measured pitch and roll, and estimated azimuth. These rotations are of the form

$$\begin{vmatrix} x_{rot} \\ y_{rot} \\ z_{rot} \end{vmatrix} = \mathbf{BA} \begin{vmatrix} x_{norm} \\ y_{norm} \\ (z_{norm} = 1) \end{vmatrix}$$

The rotated coordinates are then renormalized, and multiplied by the focal length, to yield the corner locations relative to the principal point in a vertically oriented camera:

$$\begin{vmatrix} x_{vert} \\ y_{vert} \end{vmatrix} = \begin{vmatrix} x_{rot}/z_{rot} \\ y_{rot}/z_{rot} \end{vmatrix} * f$$

These steps define a mapping from the vertical image to the source image.

Each point in the vertical image is then referenced to a location on the surface in the (Easting, Northing, up) coordinate system by scaling and translating the vertical image coordinates:

$$\begin{vmatrix} x_{surf} \\ y_{surf} \end{vmatrix} = \left(\begin{vmatrix} x_{vert} \\ y_{vert} \end{vmatrix} * \frac{z_{camera} - z_{surf}}{f} \right) + \begin{vmatrix} x_o \\ y_o \end{vmatrix} \quad (\text{B1})$$

z_{camera} is the GPS derived camera elevation, x_o and y_o represent the UTM coordinates of the point where the optical axis of the camera intersects the glacier surface, and z_{surf} is a constant elevation taken from the closest altimeter measured point to (x_o, y_o) . This last step results in a first approximation of the world coordinates of each pixel. For every pixel, the software then searches for the closest point on the surface with an altimeter derived elevation. The final surface coordinates are computed using a second iteration of equation (B1), this time using a variable $z_{surf}(x_{vert}, y_{vert})$.

General Conclusions

Through these three papers, I have explored several aspects of glaciology, all of which relate the forces which act upon glaciers and ice sheets to how the ice responds. The forces may be obvious, as with accumulation of snowfall, or unknown to us (so far), as with the causes of the strain events we observed at Siple Dome, Antarctica.

We have presented a method by which glaciologists can compute a change in glacier mass from specific balance measurements, without the benefit of an up-to-date map. Changes in both glacier area and in surface elevation since the time when an older map was made must be taken into account. Both of these terms are vital aspects of glacier response to climatic forcing. In addition, reference-surface balances, which measure the balance on an unchanging surface, and not conventional balances, are required for studies of glacier dynamics and climate change. For this reason, reference-surface balances should be routinely reported along with conventional balances.

At Siple Dome, West Antarctica, we measured vertical strain rates at several depths at two locations. We were able to measure long-term average strain rates using two types of gauges. Our observations of time-dependent strain rate variations appear over four time-scales: multi-year drift, year-to-year variability about the long-term average, seasonal-time-scale fluctuations, and strain events lasting less than a day. We computed two age-depth relationships for the ice at Divide, using data from both gauge types. Under the assumptions that the ice sheet and flow geometries are time independent, the ice at 900 m is at least 120,000 years old. This suggests that the Siple Dome deep ice core includes a complete record of the Wisconsin ice age and that the oldest part of the core is at least as old as the Sangamon interglacial of 115 to 125 ka BP.

We have mapped the pattern of glacier ELAs over a small region, and analyzed the time and space variations in that pattern. Our results do suggest that refinements can be made in the extrapolation schemes used thus far to relate individual glacier mass balance measurements to the surrounding regions. The difference in ELAs of the glaciers on the south and north sides of the western Chugach Mountains is around 1000 m. The glaciers to the northeast of Cordova have a different pattern of ELAs than the glaciers

farther west. It seems unjustified to group all of these glaciers together into one zone, as has been done in the past. Equilibrium line distributions may help replace broad geographic regions with climatically similar regions in future estimates of glacier volume change in Alaska and elsewhere.

The ideas in this thesis are applicable to tracking climate change and to the potential for the West Antarctic ice sheet to catastrophically break up. As South Cascade melts away, the western Chugach ELAs fluctuate their way through time, and Siple Dome jumps by tiny leaps and miniscule bounds, we are lucky to have the chance to watch, measure and analyze.